NASA Technical Paper 1285

Development and Validation of a Piloted Simulation of a Helicopter and External Sling Load

J. D. Shaughnessy, Thomas N. Deaux, and Kenneth R. Yenni

JANUARY 1979

NASA Technical Paper 1285

Development and Validation of a Piloted Simulation of a Helicopter and External Sling Load

J. D. Shaughnessy
Langley Research Center, Hampton, Virginia
Thomas N. Deaux
Sperry Support Services, Hampton, Virginia
Kenneth R. Yenni
Langley Research Center, Hampton, Virginia

National Aeronautics
and Space Administration

**Scientific and Technical
Information Office**

1979

CONTENTS

SUMMARY 1

INTRODUCTION 1

SYMBOLS 3

DESCRIPTION OF MATHEMATICAL MODEL 12
Coordinate Systems 12
Atmospheric Model 13
Control System 16
Automatic Flight Control System Model 17
Rotor System 18
Engine Dynamics and Governor Model 25
Fuselage Aerodynamics 26
External-Load Aerodynamics 28
Load-Ground Contact Model 28
Load Suspension System 30
Equations of Motion 33

APPLICATION TO U.S. ARMY CH-54 HELICOPTER AND CARGO CONTAINER 35

SIMULATION DESCRIPTION 39
Computer Hardware 39
Cockpit 40
Simulation Software 42
Visual Landing Display System 44
Load/Landing Zone Visual Display 44
Trim Calculations 46

VERIFICATION AND VALIDATION 47
Simulation Verification 47
Mathematical Model Validation 47
Pilot's Comments 50

CONCLUDING REMARKS 50

REFERENCES 52

TABLES 54

FIGURES 67

SUMMARY

A generalized, real-time, piloted, visual simulation of a single-rotor helicopter, suspension system, and external load is described and validated for the full flight envelope of the U.S. Army CH-54 helicopter and cargo container as an example. The mathematical model described uses modified nonlinear classical rotor theory for both the main rotor and tail rotor, nonlinear fuselage aerodynamics, an elastic suspension system, nonlinear load aerodynamics, and a load-ground contact model. The implementation of the mathematical model on a large digital computing system is described, and validation of the simulation is discussed. The mathematical model is validated by comparing measured flight data with simulated data, by comparing linearized system matrices, eigenvalues, and eigenvectors with manufacturers' data, and by the subjective comparison of handling characteristics by experienced pilots. A visual landing display system for use in simulation which generates the pilot's forward-looking real-world display is discussed, and a special head-up, down-looking load/landing zone display is described.

INTRODUCTION

Simulation and analytical research has been conducted at the Langley Research Center (LaRC) to compare various control system concepts for improving the handling qualities of single-rotor helicopters carrying relatively large external sling loads. These concepts include control jets at the load, a movable cable attachment point on the helicopter, and cable angle feedback into the helicopter stability augmentation system. It was believed that the most cost-effective and safe way to compare and study these systems was through the use of a piloted visual simulation in which wide variations in parameters and concept optimization could be explored easily and quickly.

Literature searches and discussions with industry did not locate any simulations for a helicopter sling load or any mathematical models having full-flight-envelope capability for a helicopter and load. Therefore such a model and simulation had to be developed.

The purpose of this report is to describe the mathematical model of a helicopter and external sling load which was developed, to describe the implementation of the model to obtain a piloted visual simulation, and to describe the validation of the model and simulation through comparison of simulated data with actual flight data by means of analytical techniques and experienced pilots' evaluations.

The overall mathematical model is made up of numerous submodels that describe various components of the total dynamic system. The scope of these submodels is described in general terms as follows:

Atmospheric model - The atmospheric model has variable air density, winds with variable magnitude and direction, and variable-intensity turbulence.

Control system model - The helicopter control system model converts pilot's cyclic-control-stick, collective-stick, and pedal inputs into main- and tail-rotor cyclic and collective-pitch inputs.

Rotor models - Nonlinear models for the main and tail rotors define thrust, drag, and side forces as well as hub and force moments representative of articulated rotors over a wide range of airspeeds from 100 knots through hover to rearward and sideward flight to at least 20 knots. The rotor models account for variable inflow velocity, variable rotor speed, blade twist, tip loss, blade coning, blade flapping, actuator dynamics, flapping-hinge offset, and tail-rotor flapping-hinge cant angle.

Automatic flight control system (AFCS) model - The helicopter AFCS model is based on the system used in the U.S. Army CH-54 helicopter. This AFCS provides helicopter rate and attitude stabilization in roll, pitch, and yaw.

Fuselage aerodynamics model - The fuselage aerodynamics model defines nonlinear lift, drag, and side forces as well as pitching, rolling, and yawing moments in terms of a wide range of fuselage angles of attack and sideslip, rotor downwash, body angular rates, and dynamic pressure.

External-load aerodynamics model - An external-load aerodynamics model defines nonlinear lift, drag, and side force as well as pitching, rolling, and yawing moments as a function of angles of attack and sideslip, dynamic pressure, rotor downwash, and body angular rates.

Load suspension model - A load suspension model defines cable tension in one or more cables and the resulting forces and moments acting on the helicopter and external load.

Load-ground contact model - A load-ground contact model determines the approximate forces and moments acting on the load as it comes in contact with the ground for pickup and landing.

A general set of nonlinear, rigid-body equations of motion for both the helicopter and external load determines the motion of each vehicle with respect to a flat, nonrotating Earth. An algorithm determines the trimmed helicopter control positions, helicopter attitude, and load position and attitude so that the entire dynamic system is in unaccelerated flight for a specified initial flight condition. Another algorithm obtains the equivalent linear system from the nonlinear model once the helicopter is trimmed; the linear system is used for verification and validation only.

The mathematical model is programed on a general-purpose, real-time digital computer, with data for the U.S. Army CH-54 helicopter used as inputs; and appropriate outputs are fed to a cockpit having a set of flight instruments. The computer outputs also drive a real-world, out-the-window visual display as

well as a computer-generated load/landing zone display for pilot use. The research pilot is able to control the simulated helicopter by making cyclic- and collective-stick and pedal inputs in the cockpit which generate electrical signals that are transmitted to the computer. Finally, provisions are made for recording simulated flight data and for interacting with the simulation from a control console.

Use of trade names or names of manufacturers in this report does not constitute an official endorsement of such products or manufacturers, either expressed or implied, by the National Aeronautics and Space Administration.

Contributions to this work and assistance to the authors were provided by the following persons: Dean E. Cooper, of Sikorsky Aircraft Division of United Technologies Corporation; NASA test pilot Perry L. Deal; Lt. Col. W. L. Welter, of Langley Directorate, USAAMRDL; pilots from Evergreen Helicopter, Incorporated, McMinnville, Ore., Colonial Helicopters, Incorporated, Norfolk, Va., and the 355th Aviation Company at Fort Eustis, Virginia; W. F. Lovell, J. B. Leavitt, and L. E. Becker, of Sperry Support Services; M. D. Pardue, graduate student at Old Dominion University; and Lawrence E. Barker, Jr., Lemuel E. Meetze, and Richard E. Bardusch, of LaRC.

SYMBOLS

Measurements, calculations, and programing were made in U.S. Customary Units. They are presented here in the International System of Units (SI).

A_{IC}, B_{IC} rotor lateral and longitudinal cyclic control commands, defined by equations (12), rad

A_{ICafcs}, B_{ICafcs} rotor lateral and longitudinal cyclic AFCS commands, defined by equations (14) and (13), rad or deg

A'_{IC}, B'_{IC} rotor lateral and longitudinal cyclic control displacements, defined by equations (23), rad

a rotor blade lift-curve slope, per rad

a' small angle that defines the rotor drag force, defined by equation (35), rad

$a_{x,h}, a_{y,h}, a_{z,h}$ helicopter body-axes accelerations, m/sec^2

a_0 rotor coning angle given by equation (29), rad

a_1, b_1 rotor longitudinal and lateral flapping angles with respect to control axes, defined by equations (32), rad

a_{1s}, b_{1s} rotor longitudinal and lateral flapping angles with respect to shaft axes, defined by equations (43), rad or deg

B rotor-blade tip-loss constant

b number of blades per rotor

C_h, C_ℓ Euler angle transformation matrix for helicopter and load, defined by equation (1)

C_Q rotor torque coefficient, defined by equation (36)

C_T rotor thrust coefficient, defined by equation (27)

C_Y rotor side-force coefficient, defined by equation (38)

c rotor blade chord, m

$d_{1c,e}, d_{2c,e}, d_{3c,e}$ cable direction cosines defined by equations (73)

e_{kf}, e_{kt} fuselage and tail angle-of-attack corrections due to rotor downwash, rad

e_{mr} rotor downwash factor, defined by equation (52), rad

e rotor flapping-hinge offset, m

$\Sigma F_{x,h}, \Sigma F_{y,h}, \Sigma F_{z,h}, \Sigma F_{x,\ell}, \Sigma F_{y,\ell}, \Sigma F_{z,\ell}$ force summations along helicopter and load body axes including all external forces due to rotor, body aerodynamics, ground contact, and suspension system, N

$G_{B\theta}, G_{Bq}, G_{Bx}, G_{A\phi}, G_{Ap}, G_{Ax}, G_{\theta t\psi}, G_{\theta tr}, G_{\theta ch}$ AFCS feedback gains (see table I for units)

$G_{gov}, K_{dgov}, K_{gov}, K_m$ engine/governor parameters (see table I for units)

G_u, G_v, G_w gust variables defined by equations (11), m/sec^2

g acceleration of gravity, m/sec^2

h_h, h_ℓ helicopter and load altitude, m

I_{bm}, I_{bt} main- and tail-rotor blade flapping moment of inertia, kg-m^2

I_{mr} main-rotor polar moment of inertia, kg-m^2

I_{pt} engine-power-turbine moment of inertia, kg-m^2

$I_{xx,h}, I_{yy,h}, I_{zz,h}, I_{xx,\ell}, I_{yy,\ell}, I_{zz,\ell}$ helicopter and load mass moments of inertia about body axes, kg-m^2

$I_{xz,h}, I_{xz,\ell}$ helicopter and load products of inertia, kg-m^2

i_t flow incidence at helicopter horizontal tail, defined by equation (54), rad or deg

i_{to} fixed incidence of helicopter horizontal tail, rad

$K_{c0}, K_{c1}, K_{c2}, K_{c3}, K_{c4}, K_{c5}, K_{c6}, K_{c7}$ control-system stick gain, control mixing, and unit conversion constants (see table I for units)

K_{fe} fuselage pitching-moment parameter due to rotor thrust used in equations (58), N-m

K_p load-ground contact position force parameter used in equation (61), N/m

K_{sc} load suspension system cable spring rate, N/m

K_v load-ground contact velocity force parameter used in equation (61), N/(m/sec)

$L_{c,\ell}, M_{c,\ell}, N_{c,\ell}$ total load-ground contact moments, defined by equations (66), N-m

$L_{ci,\ell}, M_{ci,\ell}, N_{ci,\ell}$ load moments due to ground contact at point i, N-m

$L_{d,h}, M_{d,h}, N_{d,h}$ helicopter body-axes moments due to body angular rates, defined by equations (89), N-m

$L_{d,\ell}, M_{d,\ell}, N_{d,\ell}$ load moments due to load angular velocities, defined by equations (95), N-m

$L_{f,h}, M_{f,h}, N_{f,h}$ total moments acting on helicopter due to fuselage aerodynamics, defined by equations (58), N-m

$\tilde{L}_h, \tilde{D}_h, \tilde{Y}_h$ helicopter fuselage lift, drag, and side forces, N

$L_{hub,h}, M_{hub,h}, N_{hub,h}$ helicopter moments in body axes due to rotor moments transmitted at the hub, defined by equation (45), N-m

$L_{hub,s}, M_{hub,s}, N_{hub,s}$ helicopter moments in shaft axes due to rotor moments transmitted at the hub, defined by equations (42) and (44), N-m

L_ℓ, M_ℓ, N_ℓ total aerodynamic moments acting on the load, defined by equations (96), N-m

$\tilde{L}_\ell, \tilde{D}_\ell, \tilde{Y}_\ell$ lift, drag, and side forces acting on the load, defined by equations (92), N

$L_{r,h}, M_{r,h}, N_{r,h}$ total body-axes moments acting on helicopter due to rotor forces and hub moments, defined by equation (46), N-m

$L_{t,h}, M_{t,h}, N_{t,h}$ body-axes moments acting on helicopter due to suspension cable, defined by equations (75), N-m

$L_{t,\ell}, M_{t,\ell}, N_{t,\ell}$ body-axes moments acting on the load due to suspension cable, defined by equations (77), N-m

L_u, L_v, L_w scales of turbulence, defined by equations (5) to (7), m

L_{wt}, M_{wt}, N_{wt} body-axes aerodynamic moments acting on fuselage, appearing in equations (58), N-m

$\Sigma L_h, \Sigma M_h, \Sigma N_h$ external moments, including main- and tail-rotor moments, fuselage aerodynamic moments, and cable suspension moments, N-m

ℓ_c suspension-system instantaneous cable length, defined by equation (69), m

ℓ_{c0} suspension-system unstretched cable length, m

$\tilde{M}_w$ mass moment of rotor blade appearing in equations (42), kg-m

m_h, m_ℓ helicopter and load mass, kg

$n_1, n_2, \ldots, n_6$ white-noise signals used in equations (10)

$p_h, q_h, r_h, p_\ell, q_\ell, r_\ell$ helicopter and load angular velocity components in body axes, rad/sec

p_s, q_s, r_s helicopter angular velocity components in shaft axes, rad/sec

p_w, q_w, r_w helicopter angular velocity components in control axes, rad/sec

Q_{am} aerodynamic torque acting on main rotor, positive in direction opposite to rotation, N-m

Q_{at} aerodynamic torque acting on tail rotor, positive in direction opposite to rotation, N-m

Q_{eng} shaft engine torque acting on rotor and fuselage (positive value tends to accelerate rotor and cause fuselage to yaw right), N-m

Q_{gen} gas-generator torque used in equations (48), N-m

Q_s resulting main- or tail-rotor shaft torque acting on fuselage, N-m

$\bar{q}_h, \bar{q}_\ell$ dynamic pressure at fuselage and load, given by equations (50) and (91), N/m^2

R main- or tail-rotor radius, m

S shaft tilt transformation matrix given by equation (18)

s Laplace operator, sec^{-1}

T,H,J main- or tail-rotor thrust, drag, and side force defined by equations (28), (34), and (39), N

T_c suspension-system cable tension, defined by equation (70), N

$u_{as,h}, v_{as,h}, w_{as,h}$ helicopter body-axes components of velocity, defined by equations (20), m/sec

$u_{as,\ell}, v_{as,\ell}, w_{as,\ell}$ load body-axes components of total airspeed, defined by equations (90), m/sec

$u_{cg,h}, v_{cg,h}, w_{cg,h}$ body-axes components of inertial velocity of helicopter c.g., given by equations (80), m/sec

$u_{cg,\ell}, v_{cg,\ell}, w_{cg,\ell}$ body-axes components of inertial velocity of load c.g., given by equations (80) with h replaced by ℓ, m/sec

$u_{ci,e}, v_{ci,e}, w_{ci,e}$ Earth-axes components of inertial velocity of the ith load-ground contact point, defined by equation (60), m/sec

$u_{hcg,e}, v_{hcg,e}, w_{hcg,e}$ Earth-axes components of inertial velocity of helicopter c.g., given by equation (84), m/sec

$u_{\ell cg,e}, v_{\ell cg,e}, w_{\ell cg,e}$ Earth-axes components of inertial velocity of load c.g., given by equation (84) with h replaced by ℓ, m/sec

$u_{gust,h}, v_{gust,h}, w_{gust,h}$,
$u_{gust,\ell}, v_{gust,\ell}, w_{gust,\ell}$ helicopter and load body-axes components of gust velocity, given by equations (90), m/sec

$u_{r,h}, v_{r,h}, w_{r,h}$ body-axes components of total airspeed at rotor hub, given by equations (19), m/sec

u_s, v_s, w_s shaft-axes components of total airspeed at rotor hub, given by equation (17), m/sec

u_w, v_w, w_w control-axes components of total airspeed at rotor hub, given by equations (22), m/sec

$u_{wind,e}, v_{wind,e}, w_{wind,e}$ Earth-axes components of windspeed, given by equation (4), m/sec

$u_{wind,h}, v_{wind,h}, w_{wind,h}$
$u_{wind,\ell}, v_{wind,\ell}, w_{wind,\ell}$ — body-axes components of windspeed for helicopter and load, given by equation (4), m/sec

$V_{as,h}, V_{as,\ell}$ — helicopter and load total airspeed defined by equations (51) and (91), m/sec

V_{wind} — magnitude of wind vector, m/sec

V_o — load sliding velocity beyond which sliding friction becomes independent of sliding velocity, m/sec

$\hat{w}_{as,\ell}$ — load body z-axis component of total airspeed with constant added to improve numerical stability, m/sec

$X_{ci,e}, Y_{ci,e}, Z_{ci,e}$ — Earth-axes components of load-ground contact forces at the ith contact point, defined by equations (61), (62), and (63), N

$X_{ci,\ell}, Y_{ci,\ell}, Z_{ci,\ell}$ — load body-axes components of load-ground contact forces at the ith contact point, given by equation (64), N

$X_{c,\ell}, Y_{c,\ell}, Z_{c,\ell}$ — load body-axes components of total load-ground contact forces, given by equations (66), N

$X_{f,h}, Y_{f,h}, Z_{f,h}$ — helicopter body-axes components of fuselage lift, drag, and side force, given by equation (57), N

X_ℓ, Y_ℓ, Z_ℓ — lift, drag, and side forces expressed in load body axes (eq. (93)), N

$X_{r,h}, Y_{r,h}, Z_{r,h}$ — helicopter body-axes components of rotor forces, given by equation (41), N

$X_{r,s}, Y_{r,s}, Z_{r,s}$ — shaft-axes components of rotor forces, defined by equations (40), N

$X_{t,h}, Y_{t,h}, Z_{t,h}$ — helicopter body-axes components of cable tension, given by equation (74), N

$X_{t,\ell}, Y_{t,\ell}, Z_{t,\ell}$ — load body-axes components of cable tension, given by equation (76), N

$x_{a,h}, y_{a,h}, z_{a,h}$ — helicopter body-axes distances from helicopter c.g. to cable attachment point, m

$x_{a,\ell}, y_{a,\ell}, z_{a,\ell}$ — load body-axes distances from load c.g. to cable attachment point, m

$x_{ci,e}, y_{ci,e}, z_{ci,e}$ — Earth-axes coordinates of ith ground contact point, m

$x_{ci,\ell}, y_{ci,\ell}, z_{ci,\ell}$	load body-axes distances from load c.g. to ith ground contact point, m
$x_{col}, x_{lat}, x_{lon}, x_{ped}$	control displacements of collective stick, lateral and longitudinal cyclic stick, and pedals (positive displacements cause climb, right roll, pitch-up, and yaw left, respectively), m
$x_{ha,e}, y_{ha,e}, z_{ha,e}$	Earth-axes inertial position of helicopter cable attachment point, given by equation (67), m
$x_{hcg,e}, y_{hcg,e}, z_{hcg,e}$	Earth-axes inertial position of helicopter c.g., given by equations (85), m
$x_{\ell a,e}, y_{\ell a,e}, z_{\ell a,e}$	Earth-axes inertial position of load cable attachment point, given by equation (68), m
$x_{\ell cg,e}, y_{\ell cg,e}, z_{\ell cg,e}$	Earth-axes inertial position of load c.g., given by equations (85) with subscript h replaced by ℓ, m
$x_{\ell cg,h}, y_{\ell cg,h}, z_{\ell cg,h}$	helicopter body-axes coordinates of load c.g., given by equation (97), m
$x_{\ell p,h}, y_{\ell p,h}, z_{\ell p,h}$	helicopter body-axes coordinates of any point p on the load, given by equation (98), m
$x_{\ell p,\ell}, y_{\ell p,\ell}, z_{\ell p,\ell}$	load body-axes coordinates of any point p on the load, m
$x_{mr,h}, y_{mr,h}, z_{mr,h}$ $x_{tr,h}, y_{tr,h}, z_{tr,h}$	helicopter body-axes coordinates of main- and tail-rotor hub, m
$x_{ps,h}, y_{ps,h}, z_{ps,h}$	helicopter body-axes coordinates of eye-level position of pilot in left seat, m
x_{screen}, y_{screen}	nondimensional screen coordinates of any point p, used in load/landing zone display defined by equations (101), m
$x_{v,e}, y_{v,e}, z_{v,e}$	Earth-axes coordinates of helicopter viewpoint, given by equation (99), m
$x_{v,h}, y_{v,h}, z_{v,h}$	helicopter body-axes coordinates of down-looking viewpoint, m
$x_{wt,h}, y_{wt,h}, z_{wt,h}$	helicopter body-axes coordinates of wind-tunnel mounting point, m
$x_{zp,e}, y_{zp,e}, z_{zp,e}$	Earth-axes inertial position of any point p fixed on the Earth, m

$x_{zp,h}, y_{zp,h}, z_{zp,h}$ helicopter body-axes coordinates of any point p on the Earth, m

$\alpha_{c,e}, \beta_{c,e}$ cable angles with respect to the vertical, defined by equations (71) and (72), rad

α_f, β_f fuselage angle of attack and sideslip, defined by equations (49) and (55), rad or deg

$\alpha_{f\ell}$ local fuselage angle of attack, defined by equation (53), rad or deg

α_ℓ, β_ℓ load angles of attack and sideslip, defined by equations (91), rad

β rotor orientation angle, rad

γ rotor Lock number, $\dfrac{\rho a c R^4}{\text{Rotor blade flapping moment of inertia}}$

$\Delta\tilde{L}_{1h}, \Delta\tilde{L}_{2h}$ incremental fuselage lift, N

$\Delta M_{1wt}, \Delta M_{2wt}$ incremental fuselage pitching moment, N-m

Δt simulation integration step size, sec

δ_{3t} tail-rotor flapping-hinge cant angle, rad

θ_{ct} commanded value of tail-rotor collective pitch given by equations (12), rad

θ_{0m} main-rotor collective pitch, given by equations (12), rad or deg

θ_{0t} effective value of tail-rotor collective pitch, given by equation (47), rad or deg

$\theta_{mafcs}, \theta_{tafcs}$ main- and tail-rotor AFCS collective pitch command, defined by equations (15) and (16), rad

θ_s longitudinal shaft tilt angle, positive for thrust vector tilted from $-z_h$ toward $-x_h$, rad

θ_1 rotor blade twist angle from root to tip, rad

$\theta_{.75}$ rotor collective pitch at three-fourths radius, defined by equation (33), rad

$\hat{\theta}_h, \hat{\phi}_h, \hat{\psi}_h$ helicopter pitch, roll, and yaw AFCS attitude errors, rad

λ_m, λ_t main- and tail-rotor inflow ratio, defined by equation (25)

μ_f coefficient of sliding friction used in load-ground contact model

μ_m, μ_t main- and tail-rotor tip-speed ratio, defined by equation (24)

ν rotor induced inflow ratio, defined by equation (26)

ρ atmospheric density given by equation (2), kg/m^3

ρ_a swashplate actuator damping ratio

σ rotor solidity, $\frac{bc}{\pi R}$

$\sigma_u, \sigma_v, \sigma_w$ body-axes components of rms gust intensity, m/sec

τ_{eng} engine time constant, sec

$\tau_{\delta 3t}$ tail-rotor δ_{3t} time constant, sec

τ_λ rotor inflow time constant, sec

Φ_o white noise power spectral density, sec

$\phi_h, \theta_h, \psi_h, \phi_\ell, \theta_\ell, \psi_\ell$ roll (ϕ), pitch (θ), and yaw (ψ) Euler angles of helicopter and load, rad

ϕ_s lateral shaft tilt angle, positive for thrust vector tilted from $-z_h$ toward $+y_h$, rad

ψ_{wind} wind angle measured clockwise from true north that defines the direction from which the wind is coming, rad

ψ_{wt} wind-tunnel yaw angle, rad

Ω rotor angular velocity, rad/sec

Ω_o commanded rotor angular velocity, rad/sec

Ω_{pt} power-turbine angular velocity, rad/sec

ω_a swashplate-actuator natural frequency, rad/sec

Abbreviations:

ADC analog to digital converter

AFCS automatic flight control system

c.g. center of gravity

DAC digital to analog converter

BLCG buttock line at c.g.

FSCG fuselage station at c.g.

WLCG water line at c.g.

RTS real-time system

rms root mean squared

VLDS visual landing display system

Dots over a symbol denote derivatives with respect to time.

Initial values of variables are denoted by (0) following the variable symbol.

Matrix transpose is denoted by a superscript T.

DESCRIPTION OF MATHEMATICAL MODEL

The mathematical model for the simulation of a single-rotor helicopter and external load can be given in terms of submodels for the various components of the total dynamic system.

A block diagram for the overall mathematical model is given in figure 1. This diagram together with the Contents should be useful in understanding the interrelationship between the submodels. In the following sections the mathematical model is described in approximately the order it would be executed in the computer so that the reader can write his own simulation program more easily.

Coordinate Systems

The following right-hand orthogonal axis systems are used in this report:

(1) Earth axes (subscript e): origin fixed on the Earth's surface, x_e-axis pointing north, y_e-axis pointing east

(2) Helicopter body axes (subscript h): origin at the helicopter c.g., x_h-axis pointing forward in the plane of symmetry of the fuselage and parallel to the helicopter water line, z_h-axis pointing downward away from the main rotor and in the plane of symmetry (see figs. 2 and 3)

(3) Shaft axes (subscript s): origin at the center of the rotor hub, y_s-axis rotated through the lateral shaft tilt angle ϕ_s about the x_h-axis, x_s-axis rotated through the longitudinal shaft tilt angle θ_s about the y_s-axis, z_s-axis coincident with the rotor shaft, applies to both the main rotor and the tail rotor (see fig. 3)

(4) Control axes (subscript w): origin at the center of the rotor hub, z_w-axis directed toward the fuselage along the axis of no feathering (the physical axis of a pure flapping rotor - a rotor with blades fixed in pitch but free to flap), x_w-axis chosen to give no y_w-component of velocity relative to the free-stream air (the free-stream air to include the air motion from turbulence and steady winds), applies to both rotors (see fig. 3)

(5) Wind-tunnel axes (subscript wt): origin at the helicopter or external-load wind-tunnel mounting point, x_{wt}-axis pointing into the relative wind, z_{wt}-axis pointing downward and perpendicular to the wind

(6) External-load body axes (subscript ℓ): origin at the load c.g., x_ℓ-axis pointing forward in the plane of symmetry of the load, z_ℓ-axis pointing downward in the plane of symmetry of the load

The Earth-to-body axis transformation for the helicopter based on the standard yaw, pitch, and roll Euler angle rotation sequence shown in figure 3 is given in matrix form as

$$C_h = \begin{bmatrix} \cos\theta_h \cos\psi_h & \cos\theta_h \sin\psi_h & -\sin\theta_h \\ \sin\theta_h \sin\phi_h \cos\psi_h & \sin\theta_h \sin\phi_h \sin\psi_h & \cos\theta_h \sin\phi_h \\ \quad - \cos\phi_h \sin\psi_h & \quad + \cos\phi_h \cos\psi_h & \\ \sin\theta_h \cos\phi_h \cos\psi_h & \sin\theta_h \cos\phi_h \sin\psi_h & \cos\theta_h \cos\phi_h \\ \quad + \sin\phi_h \sin\psi_h & \quad - \sin\phi_h \cos\psi_h & \end{bmatrix} \tag{1}$$

The transformation matrix for the load has the same form with the subscript h replaced by subscript ℓ.

Atmospheric Model

The atmospheric model used allows for air-density variations with altitude, variable wind direction and magnitude, and variable-intensity atmospheric turbulence. The air density is calculated according to the polynomial in h

$$\rho = 1.2266 - (1.176 \times 10^{-4})h + (4.337 \times 10^{-9})h^2 - (7.463 \times 10^{-14})h^3 + (5.538 \times 10^{-19})h^4 - (9.357 \times 10^{-25})h^5 \tag{2}$$

where h is the helicopter or external-load altitude above sea level, in meters, as determined from integrating the equations of motions discussed below.

Steady winds are specified in terms of magnitude and direction. The wind is expressed in Earth axes by the relations

$$\left.\begin{aligned} u_{wind,e} &= V_{wind} \cos \psi_{wind} \\ v_{wind,e} &= V_{wind} \sin \psi_{wind} \\ w_{wind,e} &= 0 \end{aligned}\right\} \tag{3}$$

where ψ_{wind} is the angle measured clockwise from true north that defines the direction from which the wind is blowing. Steady vertical winds are not simulated. The components of the steady winds are expressed in helicopter body axes by using the transformation

$$\begin{Bmatrix} u_{wind,h} \\ v_{wind,h} \\ w_{wind,h} \end{Bmatrix} = C_h \begin{Bmatrix} u_{wind,e} \\ v_{wind,e} \\ w_{wind,e} \end{Bmatrix} \tag{4}$$

The components of the steady winds are expressed in load body axes by using equation (4) with the subscript h replaced by subscript ℓ. The atmospheric turbulence mathematical model is based on the Dryden spectrum of turbulence as discussed in reference 1. This theory allows the simulation of atmospheric turbulence by passing uncorrelated white noise through linear filters to obtain gust components in body axes.

The scales of turbulence for the helicopter and the load are calculated according to the relations shown for the helicopter

$$L_{u,h} = \begin{cases} 65.7 h_h^{1/3} & (h_h \leqq 762.0;\ \sigma_u < 6.4) \\ 533.4 & (\sigma_u \geqq 6.4) \\ 762.0 & (h_h > 762.0;\ \sigma_u < 6.4) \end{cases} \tag{5}$$

$$L_{v,h} = L_{u,h} \tag{6}$$

$$L_{w,h} = \begin{cases} h_h & (h_h \leqq 762.0;\ \sigma_u < 6.4) \\ 533.4 & (\sigma_u \geqq 6.4) \\ 762.0 & (h_h > 762.0;\ \sigma_u < 6.4) \end{cases} \tag{7}$$

where σ_u is the longitudinal rms gust intensity (assumed to be the same for the helicopter and load). The scales of turbulence for the load are calculated by using equations (5), (6), and (7) with the subscript h replaced by subscript ℓ. The vertical and lateral gust intensities for the helicopter are given by

$$\sigma_{w,h} = \begin{cases} \sigma_u & (\sigma_u \geqq 6.4) \\ 0.0376\sigma_u h_h^{1/3} & (\sigma_u < 6.4) \end{cases} \tag{8}$$

and

$$\sigma_v = \sigma_u$$

The gust intensities for the load are calculated from equations (8) with the subscript h replaced by subscript ℓ. The white noise power spectral density is given by

$$\Phi_o = \Delta t/2\pi \tag{9}$$

where Δt is the digital simulation computation step size in seconds.

The components of gust velocity for the helicopter and load in body axes are calculated by passing six uncorrelated white noise signals $n_1, n_2, \ldots, n_6$ through linear filters and are given as follows for the helicopter:

$$\left.\begin{aligned} u_{gust,h} &= \frac{G_{u,h}}{s + \frac{V_{as,h}}{L_{u,h}}} n_1 \\ v_{gust,h} &= \frac{G_{v,h}\left(s + \frac{V_{as,h}}{\sqrt{3}\, L_{v,h}}\right)}{\left(s + \frac{V_{as,h}}{L_{v,h}}\right)} n_2 \\ w_{gust,h} &= \frac{G_{w,h}\left(s + \frac{V_{as,h}}{\sqrt{3}\, L_{w,h}}\right)}{\left(s + \frac{V_{as,h}}{L_{w,h}}\right)} n_3 \end{aligned}\right\} \tag{10}$$

where

$$\left.\begin{aligned} G_{u,h} &= \sigma_u\sqrt{V_{as,h}/(\pi\Phi_o L_{u,h})} \\ G_{v,h} &= \sigma_v\sqrt{3V_{as,h}/(2\pi\Phi_o L_{v,h})} \\ G_{w,h} &= \sigma_w\sqrt{3V_{as,h}/(2\pi\Phi_o L_{w,h})} \end{aligned}\right\} \tag{11}$$

The gust components for the load are computed in a similar manner. The filters may be implemented digitally by using Z transform techniques.

It was judged after discussion with G. H. Fichtl, of the NASA Marshall Space Flight Center, that for sling-load cable lengths of approximately 30 meters, the gusts for the helicopter and the external load will be essentially uncorrelated. Thus two sets of uncorrelated white noise signals are used for the helicopter and the external load.

Control System

The flight control system mathematical model converts the pilot's cyclic-stick, pedal, and collective-stick displacements and AFCS outputs to equivalent main-rotor and tail-rotor control inputs. The main-rotor collective pitch θ_{0m}, longitudinal and lateral cyclic pitch B_{IC} and A_{IC}, and tail-rotor collective pitch θ_{ct} are given in terms of collective, cyclic, and pedal displacements and AFCS outputs by the following expressions obtained from Sikorsky Aircraft Division of United Technologies Corporation:

$$\left.\begin{aligned} \theta_{0m} &= K_{c0} + K_{c1}x_{col} + \theta_{mafcs} \\ B_{IC} &= K_{c2}x_{lon} + B_{ICafcs} \\ A_{IC} &= K_{c3}x_{col} + K_{c4}x_{lat} + A_{ICafcs} \\ \theta_{ct} &= K_{c5} + K_{c6}x_{ped} + K_{c7}x_{col} + \theta_{tafcs} \end{aligned}\right\} \tag{12}$$

where x_{col}, x_{lon}, x_{lat}, and x_{ped} are the pilot's control displacements with respect to a fixed reference position. The constants K_{c0} through K_{c7} are used for stick gain, control mixing, and unit conversions. Since control feel is important to pilots, a programmable hydraulic control loader is used for the cyclic control stick and the pedals. Pertinent details of this system are discussed in the section "Simulation Description."

Automatic Flight Control System Model

The mathematical model of the automatic flight control system (AFCS) is similar to that of the attitude command system employed in the U.S. Army CH-54A helicopter, and was obtained from unpublished Sikorsky Aircraft data. The pitch channel equation is given as

$$B_{ICafcs} = G_{B\theta}\hat{\theta}_h + G_{Bq}q_h + G_{Bx}\hat{x}_{lon} \tag{13}$$

where

$$\hat{\theta}_h = \theta_h - \theta_h(0)$$

and

$$\hat{x}_{lon} = x_{lon} - x_{lon}(0)$$

The quantities $\theta_h(0)$ and $x_{lon}(0)$ are the precalculated initial trim values of θ_h and x_{lon} discussed in the section "Trim Calculations."

The roll equation is given similarly as

$$A_{ICafcs} = G_{A\phi}\hat{\phi}_h - G_{Ap}p_h + G_{Ax}\hat{x}_{lat} \tag{14}$$

where

$$\hat{\phi}_h = \phi_h - \phi_h(0)$$

and

$$\hat{x}_{lat} = x_{lat} - x_{lat}(0)$$

The yaw channel is modeled by the following equation:

$$\theta_{tafcs} = G_{\theta t\psi}\hat{\psi}_h + G_{\theta tr}r_h \tag{15}$$

where

$$\hat{\psi}_h = \psi_h - \psi_o$$

The heading command ψ_o is initially set to the helicopter trim yaw angle. During the simulation whenever the pilot actuates either microswitch located on the simulator pedals, then ψ_o is set to the current value of ψ_h. When the pilot releases the microswitches, ψ_o is set to the value of ψ_h just prior to switch release. If the heading hold feature is not desired, then a push button discrete in the cockpit will set the gain $G_{\theta t\psi}$ to zero.

The altitude channel is modeled by using the following equation:

$$\theta_{mafcs} = G_{\theta ch}\hat{h}_h \tag{16}$$

where

$$\hat{h}_h = h_h - h_o$$

The altitude command h_o is initially set to the helicopter altitude. During the operate mode, the pilot can reset h_o to the current altitude or disable the altitude hold feature by using a push-button discrete in the cockpit.

Rotor System

In the interest of real-time pilot-in-the-loop computer simulation, every effort is made to keep the rotor mathematical model simple but adequate to allow forward flight to at least 100 knots, rearward and sideward flight to 20 knots, autorotations, and large-angle maneuvers. The forces and moments due to the main and tail rotors are calculated by using a modified Bailey representation discussed in references 2 to 5.

The following discussion of rotor modeling is general and is applicable to both the main and tail rotors. Important limitations are given when necessary. Rotor variables will need "main (m)" or "tail (t)" identification when included in a computer program.

The velocity of the free stream at the hub is expressed in shaft axes in terms of inertial velocity of the helicopter center of gravity, body angular rates, steady winds, atmospheric gusts, and position of the main- and tail-rotor hubs by the following expression:

$$\begin{Bmatrix} u_s \\ v_s \\ w_s \end{Bmatrix} = S^T \begin{Bmatrix} u_{r,h} \\ v_{r,h} \\ w_{r,h} \end{Bmatrix} \tag{17}$$

where

$$S = \begin{bmatrix} \cos\theta_s & \sin\theta_s \sin\phi_s & \sin\theta_s \cos\phi_s \\ 0 & \cos\phi_s & -\sin\phi_s \\ -\sin\theta_s & \cos\theta_s \sin\phi_s & \cos\theta_s \cos\phi_s \end{bmatrix} \tag{18}$$

and

$$\left.\begin{aligned} u_{r,h} &= u_{as,h} + q_h z_{r,h} - r_h y_{r,h} \\ v_{r,h} &= v_{as,h} + r_h x_{r,h} - p_h z_{r,h} \\ w_{r,h} &= w_{as,h} + p_h y_{r,h} - q_h x_{r,h} \end{aligned}\right\} \tag{19}$$

and

$$\left.\begin{aligned} u_{as,h} &= u_{cg,h} + u_{gust,h} + u_{wind,h} \\ v_{as,h} &= v_{cg,h} + v_{gust,h} + v_{wind,h} \\ w_{as,h} &= w_{cg,h} + w_{gust,h} + w_{wind,h} \end{aligned}\right\} \tag{20}$$

The rotor orientation angle β is defined by the relation

$$\beta = \tan^{-1} \frac{v_s}{u_s} \tag{21}$$

and the velocity of the free stream at the hub is expressed in control axes by the approximation given in reference 2 (see fig. 3(c)):

$$\left.\begin{aligned} u_w &= u_s \cos\beta + v_s \sin\beta \\ v_w &= 0 \\ w_w &= w_s - B'_{IC} u_s - A'_{IC} v_s \end{aligned}\right\} \tag{22}$$

where B'_{IC} and A'_{IC} are the shaft relative cyclic control inputs for the main rotor. For the tail rotor, A'_{IC} and B'_{IC} are of course zero.

Actuator dynamics are modeled by passing the control inputs through second-order filters as

$$\left.\begin{aligned} A'_{IC} &= \frac{\omega_a^2}{s^2 + 2\rho_a\omega_a s + \omega_a^2} A_{IC} \\ B'_{IC} &= \frac{\omega_a^2}{s^2 + 2\rho_a\omega_a s + \omega_a^2} B_{IC} \end{aligned}\right\} \tag{23}$$

The filters may be implemented by using Z transform techniques. The cyclic control inputs A_{IC} and B_{IC} are generated by pilot cyclic stick motions and automatic control system output given by equations (12) to (14).

The rotor forces and moments are functions of the rotor tip-speed ratio and induced inflow ratio, as discussed in references 2, 4, 6, and 7. The tip-speed ratio μ is given by

$$\mu = \frac{u_w}{\Omega R} \tag{24}$$

where Ω is the rotor angular velocity. The inflow ratio λ is calculated by the implicit equation

$$\lambda = \frac{w_w}{\Omega R} - \nu \tag{25}$$

where the induced inflow ratio ν is determined from the differential equation

$$\dot{\nu} = \frac{1}{\tau_\lambda}\left(\frac{C_T}{2\sqrt{\mu^2 + \lambda^2}} - \nu\right) \tag{26}$$

This method of computing the inflow ratio λ assumes that the inflow is constant across the rotor disk. The thrust coefficient C_T is calculated below, and a value of the time constant τ_λ of approximately 0.1 sec is chosen to approximate the time lag associated with change in rotor inflow. This technique of using a first-order differential equation to calculate the induced velocity ratio ν is superior to algebraic calculation, because algebraic methods were found to be numerically unstable in digital simulations.

The rotor thrust T and coning angle a_0 are calculated to the third power of the tip-speed ratio according to the following relations taken from reference 4, where higher order terms have been neglected:

$$\frac{C_T}{\sigma} = \frac{a}{2}\left[\left(\frac{1}{2}B^2 + \frac{1}{4}\mu^2\right)\lambda + \left(\frac{1}{3}B^3 + \frac{1}{2}B\mu^2 - \frac{4}{9\pi}\mu^3\right)\theta_0 + \left(\frac{1}{4}B^4 + \frac{1}{4}B^2\mu^2\right)\theta_1\right] \tag{27}$$

where θ_0 is the effective blade pitch angle at the blade root and θ_1 is the twist of the blade. Then

$$T = bcR\rho(R\Omega)^2\frac{C_T}{\sigma} \tag{28}$$

and

$$a_0 = \gamma\left[\left(\frac{1}{6}B^3 + 0.04\mu^3\right)\lambda + \left(\frac{1}{8}B^4 + \frac{1}{8}B^2\mu^2\right)\theta_0 + \left(\frac{1}{10}B^5 + \frac{1}{12}B^3\mu^2\right)\theta_1\right] \tag{29}$$

The term in equation (22) in reference 4 involving the blade mass moment contributes less than 0.5°, is essentially constant, and is neglected here.

The fuselage angular velocity expressed in control axes is required in the calculation of certain rotor forces and moments. This quantity is obtained by rotating the fuselage angular velocity expressed in shaft axes through the rotor orientation angle β, neglecting the small cyclic pitch angles A_{IC} and B_{IC}. (See fig. 3(c) for clarification.)

$$\left.\begin{aligned} p_w &= p_s \cos\beta + q_s \sin\beta \\ q_w &= -p_s \sin\beta + q_s \cos\beta \\ r_w &= r_s \end{aligned}\right\} \tag{30}$$

where

$$\begin{Bmatrix} p_s \\ q_s \\ r_s \end{Bmatrix} = S^T \begin{Bmatrix} p_h \\ q_h \\ r_h \end{Bmatrix} \tag{31}$$

The flapping angles a_1 and b_1 are calculated relative to control axes by using the following formulas derived from references 3, 6, and 8 and unpublished data obtained from Sikorsky Aircraft Division of United Technologies Corporation:

$$\left.\begin{aligned} a_1 &= \frac{1}{1 - \frac{\mu^2}{2B^2}}\left[\left(2\lambda + \frac{8}{3}\theta_{.75}\right)\mu + \frac{p_w}{\Omega} - \frac{16q_w}{B^4\gamma\Omega}\right] \\ \text{and} \\ b_1 &= \frac{1}{1 + \frac{\mu^2}{2B^2}}\left(\frac{4}{3}\mu a_0 - \frac{q_w}{\Omega} - \frac{16p_w}{B^4\gamma\Omega}\right) \end{aligned}\right\} \tag{32}$$

For a rotor blade with linear twist and constant chord it can be shown that replacing θ_0, the blade pitch at the root (appearing in the references), with $\theta_{.75}$, the pitch at three-fourths radius, and dropping θ_1 will have a negligible effect on the overall solution. An expression for $\theta_{.75}$ is given as

$$\theta_{.75} = \theta_0 + 0.75\theta_1 \tag{33}$$

The downwind horizontal component of the rotor force in control axes is expressed as

$$H = Ta' \tag{34}$$

where the small angle a' is a function of the useful and induced rotor drag-lift power and inflow; however, it behaves similarly to the longitudinal flapping angle a_1. An expression for a' which includes the influence due to body rate, as discussed in reference 8 and in unpublished Sikorsky Aircraft data, is as follows:

$$a' = \frac{1}{1 - \frac{\mu^2}{2B^2}}\left[\left(2\lambda + \frac{8}{3}\theta_{.75}\right)\mu - \frac{24q_w}{B^4\gamma\Omega}\left(1 - \frac{0.29\theta_{.75}}{C_T/\sigma}\right)\right] \tag{35}$$

The expression for the rotor torque which accounts for both acceleration and deceleration torques is derived from equations (9) and (11) of reference 4 and unpublished data obtained from Sikorsky Aircraft. The torque coefficient may be expressed as a polynomial in μ times the major variables as

$$\frac{C_Q}{\sigma} = \left(0.00109 - 0.0036\lambda - 0.0027\theta_{.75} - 1.10\lambda^2 - 0.545\lambda\theta_{.75} + 0.122\theta^2_{.75}\right)$$
$$+ \left(0.00109 - 0.0027\theta_{.75} - 3.13\lambda^2 - 6.35\lambda\theta_{.75} - 1.93\theta^2_{.75}\right)\mu^2$$
$$- 0.133\lambda\theta_{.75}\mu^3 + \left(-0.976\lambda^2 - 6.38\lambda\theta_{.75} - 5.26\theta^2_{.75}\right)\mu^4 \qquad (36)$$

Thus,

$$Q_a = bcR^2\rho(R\Omega)^2 \frac{C_Q}{\sigma} \qquad (37)$$

The torque acting on the main rotor Q_{am} is calculated by using main-rotor parameters in equations (36) and (37). The reaction torque on the fuselage, which is a function of Q_{am}, is calculated in the engine dynamics and governor model discussed in the next section. The torque acting on the tail rotor Q_{at} is calculated by using tail-rotor variables in equations (36) and (37). It is assumed that the tail-rotor reaction torque acts on the fuselage directly and is equal to Q_{at}.

The rotor side force J in control axes is calculated from the following expression derived from equation (3) in reference 3, assuming that terms involving pitch and roll rate may be neglected and that the blade pitch θ_0 can be replaced by $\theta_{.75}$ and terms involving θ_1 dropped:

$$\frac{C_Y}{\sigma} = \frac{a}{2}\left[\frac{3}{4} b_1\lambda - \frac{3}{2} a_0\mu\lambda + \frac{1}{4} a_1b_1\mu - a_0a_1\mu^2 + \frac{1}{6} a_0a_1 \right.$$
$$\left. - \left(\frac{3}{4}\mu a_0 - \frac{1}{3} b_1 - \frac{1}{2}\mu^2 b_1\right)\theta_{.75}\right] \qquad (38)$$

from which

$$J = bcR\rho(R\Omega)^2\left(\frac{C_Y}{\sigma}\right) \qquad (39)$$

The rotor forces in control axes are resolved into shaft axes by assuming that the components of thrust along the x_s- and y_s-axes (fig. 3(b)) are TB'_{IC} and TA'_{IC}, respectively, and that the components of drag H and side force J along the z_s-axis are negligible compared with the thrust, so that

$$\left.\begin{aligned} X_{r,s} &= -H\cos\beta - J\sin\beta + TB'_{IC} \\ Y_{r,s} &= -H\sin\beta + J\cos\beta + TA'_{IC} \\ Z_{r,s} &= -T \end{aligned}\right\} \qquad (40)$$

These forces are expressed in helicopter body axes by using the transformation

$$\begin{Bmatrix} X_{r,h} \\ Y_{r,h} \\ Z_{r,h} \end{Bmatrix} = S \begin{Bmatrix} X_{r,s} \\ Y_{r,s} \\ Z_{r,s} \end{Bmatrix} \tag{41}$$

The hub moments due to flapping hinge offsets are given in shaft axes by the following approximate expressions derived from reference 3, where higher order terms have been neglected:

$$\left.\begin{aligned} L_{hub,s} &= \frac{1}{2} eb\Omega^2 \tilde{M}_w b_{1s} \\ M_{hub,s} &= \frac{1}{2} eb\Omega^2 \tilde{M}_w a_{1s} \end{aligned}\right\} \tag{42}$$

where the cyclic flapping angles relative to shaft axes are given by

and

$$\left.\begin{aligned} a_{1s} &= a_1 \cos\beta + b_1 \sin\beta - B'_{IC} \\ b_{1s} &= b_1 \cos\beta - a_1 \sin\beta + A'_{IC} \end{aligned}\right\} \tag{43}$$

The torque about the rotor shaft is given by

$$N_{hub,s} = Q_s \tag{44}$$

For the main rotor, Q_s is equal to Q_{eng}, the engine torque computed in the section "Engine Dynamics and Governor Model." For the tail rotor, Q_s is equal to Q_{at}. These hub moments are expressed in helicopter body axes by the transformation

$$\begin{Bmatrix} L_{hub,h} \\ M_{hub,h} \\ N_{hub,h} \end{Bmatrix} = S \begin{Bmatrix} L_{hub,s} \\ M_{hub,s} \\ N_{hub,s} \end{Bmatrix} \tag{45}$$

The total moments acting on the fuselage due to the main rotor and tail rotor are calculated by using the rotor forces given by equation (41) and hub moments given by equation (45) as

$$\begin{Bmatrix} L_{r,h} \\ M_{r,h} \\ N_{r,h} \end{Bmatrix} = \begin{Bmatrix} L_{hub,h} \\ M_{hub,h} \\ N_{hub,h} \end{Bmatrix} + \begin{bmatrix} 0 & -z_{r,h} & y_{r,h} \\ z_{r,h} & 0 & -x_{r,h} \\ -y_{r,h} & x_{r,h} & 0 \end{bmatrix} \begin{Bmatrix} X_{r,h} \\ Y_{r,h} \\ Z_{r,h} \end{Bmatrix} \tag{46}$$

The mathematical model developed here assumes no δ_{3t} hinges on the main rotor, that is, blade-coning and lead-lag motion does not affect blade pitch. It is assumed, however, that the tail rotor has large values of δ_{3t}; for example, if $\delta_{3t} = 45^{\circ}$, then 1° of increased coning reduces the blade pitch by 1° and conversely. This effect is modeled as follows: the tail-rotor coning angle a_{0t} is calculated using equation (29) with the current value of effective tail-rotor collective pitch θ_{0t}. The new value of θ_{0t} is determined by solving the first-order differential equation

$$\dot{\theta}_{0t} = \frac{1}{\tau_{\delta 3t}}(\theta_{ct} - a_{0t} \tan \delta_{3t} - \theta_{0t}) \tag{47}$$

where θ_{0t} is the collective pitch value commanded by the pilot's pedals and the automatic control system. The time constant $\tau_{\delta 3t}$ is taken as small as possible while maintaining a good margin of numerical stability. A value between 0.05 and 0.2 second is typical. This method is superior to a purely algebraic calculation of θ_{0t} in that the algebraic method was found to be numerically unstable in digital simulations.

Engine Dynamics and Governor Model

The engine dynamics and governor model was adapted from one used by Boeing Vertol Company in a simulation of a heavy-lift helicopter. This model includes the effects of a gas generator, a power turbine, rotor inertia, and shaft compliance. The following differential equations define this model:

$$\left.\begin{aligned} \dot{\Omega}_m &= \left[Q_{eng} - Q_{am} + K_{dgov}(\Omega_{pt} - \Omega_m)\right] \Big/ I_{mr} \\ \dot{Q}_{eng} &= K_m(\Omega_{pt} - \Omega_m) \\ \dot{\Omega}_{pt} &= \left[Q_{gen} + K_{gov}(\Omega_o - \Omega_{pt}) - Q_{eng} - K_{dgov}(\Omega_{pt} - \Omega_m)\right] \Big/ I_{pt} \\ \dot{Q}_{gen} &= \left[Q_{am} - Q_{gen} + G_{gov}(\Omega_o - \Omega_{pt})\right] \Big/ \tau_{eng} \end{aligned}\right\} \tag{48}$$

The input variables to these differential equations are Ω_o, the reference rotor speed, and Q_{am}, the aerodynamic torque acting on the main rotor, given by equation (37) with the appropriate parameters for the main rotor. The outputs are the rotor speed Ω_m and the engine torque Q_{eng}. The power-turbine speed Ω_{pt} and the gas-generator torque Q_{gen} are internal variables. The constant K_m represents the shaft compliance. The constant K_{dgov} is needed for computational stability. The constants K_{gov} and G_{gov} are the power-turbine and gas-generator speed governor gains, and τ_{eng} is the gas-generator time constant. The aerodynamic torque Q_{am} appears in the Q_{gen} differential equation to allow the governor to hold reasonably constant rotor speed under widely varying aerodynamic torques.

Fuselage Aerodynamics

The helicopter fuselage force and moment data are assumed to be given in equation and table form in wind-tunnel axes in terms of local angle of attack, local angle of incidence at the tail, angle of sideslip, body angular rates, and dynamic pressure.

The free-stream angle of attack is given by

$$\alpha_f = \tan^{-1} \frac{w_{as,h}}{u_{as,h}} \qquad (-\pi \leq \alpha_f \leq \pi) \tag{49}$$

where the velocity components are calculated by using equations (20). The free-stream dynamic pressure is given by

$$\bar{q}_h = \frac{1}{2} \rho V_{as,h}^2 \tag{50}$$

where

$$V_{as,h} = \sqrt{u_{as,h}^2 + v_{as,h}^2 + w_{as,h}^2} \tag{51}$$

The effect of the main-rotor downwash on the local angle of attack is accounted for by introducing a rotor downwash factor obtained from unpublished Sikorsky Aircraft data as

$$e_{mr} = \frac{C_{Tm}}{2\left(\lambda_m^2 + \mu_m^2\right)} \tag{52}$$

where λ_m and μ_m are the main-rotor inflow and tip-speed ratios, respectively, and C_{Tm} is the main-rotor thrust coefficient. The local angle of attack for the fuselage is given by

$$\alpha_{f\ell} = \alpha_f - e_{mr}e_{kf} \qquad (-\pi \leqq \alpha_{f\ell} \leqq \pi) \tag{53}$$

and the local incidence at the tail is given by

$$i_t = i_{to} - (e_{kt} - e_{kf})e_{mr} \tag{54}$$

where e_{kt} and e_{kf} are empirical constants which have been determined by Sikorsky Aircraft from wind-tunnel and flight-test correlation. The constant i_{to} is the fixed incidence of the horizontal-tail surface.

The fuselage sideslip angle is given by

$$\beta_f = \sin^{-1}\frac{v_{as,h}}{V_{as,h}} \qquad \left(-\frac{\pi}{2} \leqq \beta_f \leqq \frac{\pi}{2}\right) \tag{55}$$

and the wind-tunnel yaw angle is given by

$$\psi_{wt} = -\beta_f \tag{56}$$

Since wind-tunnel data generally do not cover the full ranges of angle of attack and sideslip, it is assumed that force and moment coefficients remain constant beyond the limits of these angles. This assumption is based on the fact that generally when these angles are large, the airspeed is low, so that the fuselage forces and moments are relatively small.

The forces in wind-tunnel stability axes are transformed into body axes by the relation

$$\begin{Bmatrix} X_{f,h} \\ Y_{f,h} \\ Z_{f,h} \end{Bmatrix} = \begin{bmatrix} -\cos\alpha_f \cos\beta_f & -\cos\alpha_f \sin\beta_f & \sin\alpha_f \\ -\sin\beta_f & \cos\beta_f & 0 \\ -\sin\alpha_f \cos\beta_f & -\sin\alpha_f \sin\beta_f & -\cos\alpha_f \end{bmatrix} \begin{Bmatrix} \tilde{D}_h \\ \tilde{Y}_h \\ \tilde{L}_h \end{Bmatrix} \tag{57}$$

The basic fuselage aerodynamic moments are assumed to be given in body axes, and the total fuselage aerodynamic moments, including the effects of the c.g. being offset from the wind-tunnel mounting point as well as damping due to angular velocity and rotor downwash, are obtained as follows:

$$\left.\begin{aligned} L_{f,h} &= L_{wt} + Z_{f,h}y_{wt,h} - Y_{f,h}z_{wt,h} + L_{d,h} \\ M_{f,h} &= M_{wt} + X_{f,h}z_{wt,h} - Z_{f,h}x_{wt,h} + M_{d,h} + K_{fe}T_m \\ N_{f,h} &= N_{wt} + Y_{f,h}x_{wt,h} - X_{f,h}y_{wt,h} + N_{d,h} \end{aligned}\right\} \tag{58}$$

The last term in the $M_{f,h}$ equation represents the static moment due to main-rotor downwash at the horizontal tail. The terms $L_{d,h}$, $M_{d,h}$, and $N_{d,h}$ account for the aerodynamic moments due to body angular velocities and are discussed subsequently in "Application to U.S. Army CH-54 Helicopter and Cargo Container."

External-Load Aerodynamics

The aerodynamic forces and moments acting on the external load are calculated in essentially the same way as the fuselage aerodynamics: in terms of dynamic pressure, angles of attack and sideslip, and body angular rates. The rotor downwash effects are not considered important for long cables as far as pendulum and rocking motions are concerned, but experience has shown that some simulated downwash is necessary to provide aerodynamic damping of vertical bounce-type oscillations near hover due to cable elasticity. Generally force and moment data are missing at large angles of attack, so that some type of trigonometric formulation for forces and moments is required. Specific details of the aerodynamic characteristics for a particular external load are discussed subsequently in the application section.

Load-Ground Contact Model

Since the pickup and release of sling loads are to be studied, a mathematical model of the load-ground contact forces is required. This model is derived on the assumptions that (1) the ground can be represented by springs and dashpots, so that vertical forces act on each corner of the base of the load in proportion to the distance that the corner is below ground level, and (2) viscous sliding friction retards translational motion.

The inertial position of the ith contact point is determined from the relations

$$\begin{Bmatrix} x_{ci,e} \\ y_{ci,e} \\ z_{ci,e} \end{Bmatrix} = \begin{Bmatrix} x_{\ell cg,e} \\ y_{\ell cg,e} \\ z_{\ell cg,e} \end{Bmatrix} + C_\ell^T \begin{Bmatrix} x_{ci,\ell} \\ y_{ci,\ell} \\ z_{ci,\ell} \end{Bmatrix} \qquad (i = 1, 2, 3, 4) \tag{59}$$

where the first term on the right-hand side defines the inertial position of the load c.g.; the second term, the contact point with respect to the c.g. The inertial velocities of this load contact point are given by

$$\begin{Bmatrix} u_{ci,e} \\ v_{ci,e} \\ w_{ci,e} \end{Bmatrix} = \begin{Bmatrix} u_{\ell cg,e} \\ v_{\ell cg,e} \\ w_{\ell cg,e} \end{Bmatrix} + C_{\ell}^{T} \begin{Bmatrix} q_{\ell} z_{ci,\ell} - r_{\ell} y_{ci,\ell} \\ r_{\ell} x_{ci,\ell} - p_{\ell} z_{ci,\ell} \\ p_{\ell} y_{ci,\ell} - q_{\ell} x_{ci,\ell} \end{Bmatrix} \qquad (i = 1, 2, 3, 4) \tag{60}$$

The vertical ground contact forces are computed for each corner of the load by the equation

$$Z_{ci,e} = -K_p z_{ci,e} - K_v w_{ci,e} \qquad (i = 1, 2, 3, 4) \tag{61}$$

If $Z_{ci,e} > 0$, then the load is being pulled toward the Earth; therefore, $Z_{ci,e}$ is set to zero. The viscous sliding forces are then determined in terms of the vertical force and the horizontal component of velocity as

$$X_{ci,e} = \begin{cases} \mu_f Z_{ci,e} \dfrac{u_{ci,e}}{V_o} & (-V_o \leq u_{ci,e} \leq V_o) \\ \mu_f Z_{ci,e} & (u_{ci,e} > V_o) \\ -\mu_f Z_{ci,e} & (u_{ci,e} < -V_o) \end{cases} \tag{62}$$

and

$$Y_{ci,e} = \begin{cases} \mu_f Z_{ci,e} \dfrac{v_{ci,e}}{V_o} & (-V_o \leq v_{ci,e} \leq V_o) \\ \mu_f Z_{ci,e} & (v_{ci,e} > V_o) \\ -\mu_f Z_{ci,e} & (v_{ci,e} < -V_o) \end{cases} \tag{63}$$

for $i = 1, 2, 3, 4$. This model assumes that the sliding force is proportional to the vertical force $Z_{ci,e}$ for sliding velocities greater than $V_o = 0.31$ m/sec and proportional to the product of vertical force and sliding velocity for velocities less than this value. The load contact forces at the ith contact point are transformed into load body axes by the transformation

$$\begin{Bmatrix} X_{ci,\ell} \\ Y_{ci,\ell} \\ Z_{ci,\ell} \end{Bmatrix} = C_{\ell} \begin{Bmatrix} X_{ci,e} \\ Y_{ci,e} \\ Z_{ci,e} \end{Bmatrix} \qquad (i = 1, 2, 3, 4) \qquad (64)$$

and the moments acting on the load due to ground contact forces at the ith contact point are

$$\left.\begin{aligned} L_{ci,\ell} &= Z_{ci,\ell}Y_{ci,\ell} - Y_{ci,\ell}Z_{ci,\ell} \\ M_{ci,\ell} &= X_{ci,\ell}Z_{ci,\ell} - Z_{ci,\ell}X_{ci,\ell} \\ N_{ci,\ell} &= Y_{ci,\ell}X_{ci,\ell} - X_{ci,\ell}Y_{ci,\ell} \end{aligned}\right\} \qquad (i = 1, 2, 3, 4) \qquad (65)$$

The total forces and moments acting on the load are thus given by

$$\left.\begin{aligned} X_{c,\ell} &= \Sigma X_{ci,\ell} \\ Y_{c,\ell} &= \Sigma Y_{ci,\ell} \\ Z_{c,\ell} &= \Sigma Z_{ci,\ell} \end{aligned}\right\}$$

and

$$\left.\begin{aligned} L_{c,\ell} &= \Sigma L_{ci,\ell} \\ M_{c,\ell} &= \Sigma M_{ci,\ell} \\ N_{c,\ell} &= \Sigma N_{ci,\ell} \end{aligned}\right\} \qquad (i = 1, 2, 3, 4) \qquad (66)$$

Load Suspension System

The mathematical model for the external-load suspension system is based on the assumption that the cable(s) may be represented by spring(s) without damping. This assumption allows the cable tension to be calculated easily in terms of the cable spring constant and the vector distance between the cable attachment points. With a digital simulation the inertial positions of the cable attachment points are readily calculated, thus simplifying the calculation of the distance between the points. It was found by trial and error that

the simulated cable spring constant should be selected such that the cable vertical bounce frequency is not higher than approximately 2 Hz, in order to maintain numerical stability with an integration step size of 1/32 second in digital simulations.

The inertial position of the cable attachment point on the helicopter shown in figure 4 is calculated in terms of the inertial position of the helicopter c.g. and the distance between this position and the attachment point as

$$\begin{Bmatrix} x_{ha,e} \\ y_{ha,e} \\ z_{ha,e} \end{Bmatrix} = \begin{Bmatrix} x_{hcg,e} \\ y_{hcg,e} \\ z_{hcg,e} \end{Bmatrix} + C_h^T \begin{Bmatrix} x_{a,h} \\ y_{a,h} \\ z_{a,h} \end{Bmatrix} \tag{67}$$

The inertial position of the cable attachment point on the load shown in figure 4 is calculated similarly as

$$\begin{Bmatrix} x_{\ell a,e} \\ y_{\ell a,e} \\ z_{\ell a,e} \end{Bmatrix} = \begin{Bmatrix} x_{\ell cg,e} \\ y_{\ell cg,e} \\ z_{\ell cg,e} \end{Bmatrix} + C_\ell^T \begin{Bmatrix} x_{a,\ell} \\ y_{a,\ell} \\ z_{a,\ell} \end{Bmatrix} \tag{68}$$

The cable length is determined from the square root of the sum of the squares of differences in inertial coordinates of cable attachment points as

$$\ell_c = \sqrt{(x_{ha,e} - x_{\ell a,e})^2 + (y_{ha,e} - y_{\ell a,e})^2 + (z_{ha,e} - z_{\ell a,e})^2} \tag{69}$$

If the unstretched cable length is ℓ_{c0}, then the cable tension is simply

$$T_c = K_{sc}(\ell_c - \ell_{c0}) \tag{70}$$

where K_{sc} is the cable spring constant. A test on the sign of T_c is continuously made to insure that the cable does not exert a compression force. If $(\ell_c - \ell_{c0})$ becomes negative, then T_c is set to zero.

The cable tension force must be expressed in helicopter and load body axes so that its effect can be included in the equations of motion. Before the

tension force can be expressed in body axes, the inertial orientation of the cable - assumed straight - must be determined.

The angle that the cable makes with the vertical in the north-vertical plane is defined in figure 4 and is given by

$$\beta_{c,e} = \tan^{-1} \frac{x_{\ell a,e} - x_{ha,e}}{z_{\ell a,e} - z_{ha,e}} \tag{71}$$

The inertial cable angle in the east-west direction is also defined in figure 4 and is given by

$$\alpha_{c,e} = \tan^{-1} \frac{(y_{ha,e} - y_{\ell a,e}) \cos \beta_{c,e}}{z_{\ell a,e} - z_{ha,e}} \tag{72}$$

Three cable direction cosines are defined with respect to Earth axes by

$$\left.\begin{aligned} d_{1c,e} &= \sin \beta_{c,e} \cos \alpha_{c,e} = (x_{\ell a,e} - x_{ha,e})/\ell_c \\ d_{2c,e} &= -\sin \alpha_{c,e} = (y_{\ell a,e} - y_{ha,e})/\ell_c \\ d_{3c,e} &= \cos \beta_{c,e} \cos \alpha_{c,e} = (z_{\ell a,e} - z_{ha,e})/\ell_c \end{aligned}\right\} \tag{73}$$

The tension force is resolved into helicopter body axes by the expression

$$\begin{Bmatrix} X_{t,h} \\ Y_{t,h} \\ Z_{t,h} \end{Bmatrix} = T_c C_h \begin{Bmatrix} d_{1c,e} \\ d_{2c,e} \\ d_{3c,e} \end{Bmatrix} \tag{74}$$

The moments acting on the helicopter due to the cable tension are computed according to

$$\left.\begin{aligned} L_{t,h} &= Z_{t,h} y_{a,h} - Y_{t,h} z_{a,h} \\ M_{t,h} &= X_{t,h} z_{a,h} - Z_{t,h} x_{a,h} \\ N_{t,h} &= Y_{t,h} x_{a,h} - X_{t,h} y_{a,h} \end{aligned}\right\} \tag{75}$$

The tension force is resolved into load body axes by the expression

$$\begin{Bmatrix} X_{t,\ell} \\ Y_{t,\ell} \\ Z_{t,\ell} \end{Bmatrix} = -T_c C_\ell \begin{Bmatrix} d_{1c,e} \\ d_{2c,e} \\ d_{3c,e} \end{Bmatrix} \tag{76}$$

and the moments acting on the load due to the cable tension are given by

$$\left.\begin{aligned} L_{t,\ell} &= Z_{t,\ell} y_{a,\ell} - Y_{t,\ell} z_{a,\ell} \\ M_{t,\ell} &= X_{t,\ell} z_{a,\ell} - Z_{t,\ell} x_{a,\ell} \\ N_{t,\ell} &= Y_{t,\ell} x_{a,\ell} - X_{t,\ell} y_{a,\ell} \end{aligned}\right\} \tag{77}$$

Equations of Motion

The equations of motion for both the helicopter and the external sling load are developed in body axes with respect to a flat, nonrotating Earth. It is assumed for convenience that each body is rigid and that the x_h-z_h plane and the x_ℓ-z_ℓ plane are planes of mass symmetry and that gyroscopic effects of engines are negligible. The equations of motion for the helicopter are developed first.

The translational motion equations for the helicopter are given in terms of body-axes components of angular velocity, translational velocity, accelerations, and components of gravity as

$$\left.\begin{aligned} \dot{u}_{cg,h} &= r_h v_{cg,h} - q_h w_{cg,h} + a_{x,h} - g \sin \theta_h \\ \dot{v}_{cg,h} &= p_h w_{cg,h} - r_h u_{cg,h} + a_{y,h} + g \cos \theta_h \sin \phi_h \\ \dot{w}_{cg,h} &= q_h u_{cg,h} - p_h v_{cg,h} + a_{z,h} + g \cos \theta_h \cos \phi_h \end{aligned}\right\} \tag{78}$$

where

$$\left.\begin{aligned} a_{x,h} &= \Sigma F_{x,h}/m_h \\ a_{y,h} &= \Sigma F_{y,h}/m_h \\ a_{z,h} &= \Sigma F_{z,h}/m_h \end{aligned}\right\} \tag{79}$$

The summations include all external forces: main- and tail-rotor forces, fuselage aerodynamic forces, and cable suspension forces. The last terms on the right-hand side of equations (78) give the acceleration components due to gravity. The inertial velocity of the helicopter is given in body axes by integrating equations (78) as

$$\left.\begin{aligned} u_{cg,h} &= \int \dot{u}_{cg,h}\, dt + u_{cg,h}(0) \\ v_{cg,h} &= \int \dot{v}_{cg,h}\, dt + v_{cg,h}(0) \\ w_{cg,h} &= \int \dot{w}_{cg,h}\, dt + w_{cg,h}(0) \end{aligned}\right\} \tag{80}$$

The equations of rotational motion are used in the following form:

$$\left.\begin{aligned} \dot{p}_h &= \left\{ \Sigma L_h - (I_{zz,h} - I_{yy,h}) q_h r_h + I_{xz,h} p_h q_h \right. \\ &\quad \left. + \left[\Sigma N_h - (I_{yy,h} - I_{xx,h}) p_h q_h - I_{xz,h} q_h r_h \right] \frac{I_{xz,h}}{I_{zz,h}} \right\} \Big/ \left(I_{xx,h} - I_{xz,h}^2 / I_{zz,h} \right) \\ \dot{q}_h &= \left[\Sigma M_h - (I_{xx,h} - I_{zz,h}) p_h r_h + I_{xz,h} \left(r_h^2 - p_h^2 \right) \right] \Big/ I_{yy,h} \\ \dot{r}_h &= \left[\Sigma N_h - (I_{yy,h} - I_{xx,h}) p_h q_h + I_{xz,h} (\dot{p}_h - q_h r_h) \right] \Big/ I_{zz,h} \end{aligned}\right\} \tag{81}$$

The body-axes components of angular velocity are determined by integrating equations (81) as

$$\left.\begin{aligned} p_h &= \int \dot{p}_h\, dt + p_h(0) \\ q_h &= \int \dot{q}_h\, dt + q_h(0) \\ r_h &= \int \dot{r}_h\, dt + r_h(0) \end{aligned}\right\} \tag{82}$$

The helicopter Euler angles shown in figure 3(a) are determined by integrating the following differential equations:

$$\left.\begin{aligned}
\dot{\psi}_h &= (q_h \sin \phi_h + r_h \cos \phi_h)/\cos \theta_h \\
\dot{\theta}_h &= q_h \cos \phi_h - r_h \sin \phi_h \\
\dot{\phi}_h &= p_h + (q_h \sin \phi_h + r_h \cos \phi_h)/\tan \theta_h
\end{aligned}\right\} \tag{83}$$

The inertial velocity of the helicopter c.g. expressed in body axes is given in Earth coordinates by the transformation

$$\begin{Bmatrix} u_{hcg,e} \\ v_{hcg,e} \\ w_{hcg,e} \end{Bmatrix} = C_h^T \begin{Bmatrix} u_{cg,h} \\ v_{cg,h} \\ w_{cg,h} \end{Bmatrix} \tag{84}$$

The Earth-axes coordinates of the helicopter c.g. are determined by integrating equation (84) to obtain

$$\left.\begin{aligned}
x_{hcg,e} &= \int u_{hcg,e}\, dt + x_{hcg,e}(0) \\
y_{hcg,e} &= \int v_{hcg,e}\, dt + y_{hcg,e}(0) \\
z_{hcg,e} &= \int w_{hcg,e}\, dt + z_{hcg,e}(0)
\end{aligned}\right\} \tag{85}$$

The equations of motion for the external load may be obtained by changing all the subscripts h to ℓ in equations (78) to (85). The external-load equations of motion thus obtained may then be solved together with the equations of motion for the helicopter to obtain load motions.

APPLICATION TO U.S. ARMY CH-54 HELICOPTER AND CARGO CONTAINER

Rotor and fuselage data for the U.S. Army CH-54 helicopter were obtained from unpublished Sikorsky Aircraft data, flight tests at Langley Research Center, and reference 9. The fuselage and main- and tail-rotor data used in the simulation are listed in table I. The fuselage wind-tunnel data are given in figures 5 to 11. These curves are entered with local fuselage angle of attack $\alpha_{f\ell}$, wind-tunnel yaw (sideslip) angle ψ_{wt}, local incidence at the tail i_t, and dynamic pressure $\bar{q}_h$ as determined from equations (53), (56), (54), and (50), respectively. Values of e_{kt} and e_{kf} of 1.8 and 0.5, respectively, were used in these equations to determine fuselage lift, side force, rolling moment, pitching moment, and yawing moment.

The fuselage lift is calculated by using the data from figures 5 and 6 and the following equation:

$$\tilde{L}_h = \left(\frac{\Delta\tilde{L}_{1h}}{\bar{q}_h} + \frac{\Delta\tilde{L}_{2h}}{\bar{q}_h}\right)\bar{q}_h \tag{86}$$

The fuselage wind-tunnel pitching moment is calculated by using the data from figures 9 and 10 and the following equation:

$$M_{wt} = \left(\frac{\Delta M_{1wt}}{\bar{q}_h} + \frac{\Delta M_{2wt}}{\bar{q}_h}\right)\bar{q}_h \tag{87}$$

The fuselage drag is calculated according to the formula obtained from Sikorsky Aircraft

$$\tilde{D}_h = \left(7.25 + 2.4\alpha_{f\ell} + 42.9\alpha_{f\ell}^2 + 45.6\psi_{wt}^2\right)\bar{q}_h \tag{88}$$

where $\alpha_{f\ell}$ and ψ_{wt} are in radians.

The fuselage moments due to body angular rates are computed according to the formulas obtained from unpublished Sikorsky Aircraft data as

$$\left.\begin{aligned} L_{d,h} &= 95.6 r_h V_{as,h} \\ M_{d,h} &= -218 q_h V_{as,h} \\ N_{d,h} &= -322 r_h V_{as,h} \end{aligned}\right\} \tag{89}$$

where $V_{as,h}$ is computed by using equation (51), and r_h and q_h are in radians per second. Note that the rolling moment $L_{d,h}$ is a function of r_h not p_h. The fuselage aerodynamic forces and moments thus determined are used in equations (58). It is noted that in the transformation of aerodynamic forces from wind-tunnel to body axes given by equation (57), the sideslip angle β_f was inadvertently set to zero. The change in handling qualities caused by this error is considered to be negligible at cruise conditions and nonexistent at hover.

Mass data, cable attachment point coordinates, ground contact coordinates and parameters, and nominal cable length used for a 2.4-m by 2.4-m by 6.1-m cargo container are given in table II. Aerodynamic data used for the cargo container are derived below from data given in references 10 and 11. Since large angles of sideslip and angles of attack were expected during cruise and hover flight, the wind-tunnel data - which ranged from -5° to 45° in pitch and

from 0^{o} to 95^{o} in yaw - had to be modified to allow $\pm 180^{o}$ angle-of-attack variation and $\pm 90^{o}$ angle-of-sideslip variation. This was accomplished by fitting trigonometric functions to the existing data, as shown in equations (92) and (94).

The load components of free-stream velocity $u_{as,\ell}$, $v_{as,\ell}$, and $w_{as,\ell}$ are obtained by adding steady-wind, gust, and inertial components calculated by using the load version of equations (4), (10), and (80) as follows:

$$\left.\begin{aligned} u_{as,\ell} &= u_{cg,\ell} + u_{gust,\ell} + u_{wind,\ell} \\ v_{as,\ell} &= v_{cg,\ell} + v_{gust,\ell} + v_{wind,\ell} \\ w_{as,\ell} &= w_{cg,\ell} + w_{gust,\ell} + w_{wind,\ell} \end{aligned}\right\} \tag{90}$$

Then the load angles of attack and sideslip and the dynamic pressure are calculated from the following expressions:

$$\left.\begin{aligned} \alpha_{\ell} &= \tan^{-1}\frac{w_{as,\ell}}{u_{as,\ell}} && \left(-\pi \leq \alpha_{\ell} \leq \pi\right) \\ \beta_{\ell} &= \sin^{-1}\frac{v_{as,\ell}}{V_{as,\ell}} && \left(-\frac{\pi}{2} \leq \beta_{\ell} \leq \frac{\pi}{2}\right) \\ \bar{q}_{\ell} &= \frac{1}{2}\rho V_{as,\ell}^{2} \\ V_{as,\ell} &= \sqrt{u_{as,\ell}^{2} + v_{as,\ell}^{2} + \hat{w}_{as,\ell}^{2}} \end{aligned}\right\} \tag{91}$$

It was found in simulation that during hover with no winds, divergent oscillations of load angular motions would occur. This was due to the fact that in the zero-airspeed condition, load oscillations due to cable stretch were essentially undamped and the slight phase shift due to the numerical integration of the equations of motion caused a numerical instability. This instability was eliminated by adding a constant "rotor downwash" value to the z_{ℓ}-component of velocity as follows:

$$\hat{w}_{as,\ell} = w_{as,\ell} - 9.14$$

The cargo container lift, drag, and side forces in wind axes at the load geometric center are calculated from expressions derived from the data in reference 10 as

$$\left.\begin{aligned}
\tilde{L}_\ell &= (6.5 \sin 2\alpha_\ell \cos \beta_\ell)\bar{q}_\ell \\
\tilde{D}_\ell &= \left[20.9 - 7.66(1 + \cos 2\alpha_\ell \cos \beta_\ell)\right]\bar{q}_\ell \\
\tilde{Y}_\ell &= (-7.9 \sin 2\beta_\ell \cos 2\alpha_\ell)\bar{q}_\ell
\end{aligned}\right\} \tag{92}$$

These forces are expressed in load body axes by using the transformation

$$\begin{Bmatrix} X_\ell \\ Y_\ell \\ Z_\ell \end{Bmatrix} = \begin{bmatrix} -\cos \alpha_\ell \cos \beta_\ell & -\cos \alpha_\ell \sin \beta_\ell & \sin \alpha_\ell \\ -\sin \beta_\ell & \cos \beta_\ell & 0 \\ -\sin \alpha_\ell \cos \beta_\ell & -\sin \alpha_\ell \sin \beta_\ell & -\cos \alpha_\ell \end{bmatrix} \begin{Bmatrix} \tilde{D}_\ell \\ \tilde{Y}_\ell \\ \tilde{L}_\ell \end{Bmatrix} \tag{93}$$

The cargo container aerodynamic moments are given below and are based on the assumption that the static pitching and rolling moments are negligible in comparison with the pitching and rolling moments caused by the suspension system. The static yawing moment was derived from the data in reference 10 as

$$N_{S,\ell} = \left(-7.73 \sin 2\beta_\ell + 4.47 \sin 4\beta_\ell \left|\cos \alpha_\ell\right|\right)\bar{q}_\ell \tag{94}$$

The aerodynamic moments due to rolling, pitching, and yawing angular velocities are assumed to be proportional to the product of airspeed and angular velocity, as in the case of the fuselage moments given by equations (89), and are given by

$$\left.\begin{aligned}
L_{d,\ell} &= -89V_{as,\ell}p_\ell \\
M_{d,\ell} &= -89V_{as,\ell}q_\ell \\
N_{d,\ell} &= -89V_{as,\ell}r_\ell
\end{aligned}\right\} \tag{95}$$

where p_ℓ, q_ℓ, and r_ℓ are in radians per second. The total aerodynamic moments acting on the load are thus given by

$$\left.\begin{aligned}
L_\ell &= L_{d,\ell} \\
M_\ell &= M_{d,\ell} \\
N_\ell &= N_{d,\ell} + N_{S,\ell}
\end{aligned}\right\} \tag{96}$$

SIMULATION DESCRIPTION

Computer Hardware

The mathematical model has been programed in FORTRAN IV for operation on the Langley real-time simulation system using the Control Data CYBER 175 digital computer system. The program accepts inputs from the simulation cockpit through ADC's, and outputs voltages to the simulator through DAC's. The program flow is controlled by an operator through use of a simulation control console (fig. 12).

The simulation control console consists of white indicator lights, red indicator lights, function sense switches, mode control switches, a data entry keyboard, digital decimal display unit, and potentiometers. The white indicator lights are used to indicate program status or diagnostics. The red indicator lights are used to indicate program diagnostics. The function sense switches are used to select program options. The mode control switches shown in figures 13 and 14(a) are used to control the running of the RTS computer program. Each switch (mode) is briefly described as to its use (mode nominally active when switch depressed):

OPER (OPERATE) - begins updating time and integrating the differential equations

HOLD - holds integrated variables at previous value

RESET - initializes program at Time = 0

IDLE - idles the computer (no computations)

CHANGE - changes program variable to the new value entered on the data entry keyboard

SCAN - scans through tables and displays values on the digital decimal display unit

RELEASE - releases CHANGE and SCAN modes

ERASE - erases real-time disk file

TERM (TERMINATE) - terminates program at simulation control console and transfers control to the Tektronix terminal

READ - loads read overlay

PRINT - loads print overlay

RELEASE - releases ERASE, TERM, READ, and PRINT modes

The data entry keyboard shown in figures 13 and 14(b) is used to input new values for program variables. The keyboard is used in conjunction with the

digital decimal display shown in figures 13 and 14(c). Any program variable can be changed with these two units by following a simple procedure.

The potentiometers are used to input variables (through ADC's). They are mainly used for checkout.

The Tektronix terminal is used to communicate interactively with the CYBER 175. When the RTS program is running, the terminal is used as an output device, for example, for error messages.

Cockpit

The cockpit, which is linked to the CYBER 175 computer for the simulation, is shown in figures 15 to 18. It has simulated instrumentation, pilot controls, and a visual landing display system to simulate a helicopter cockpit.

The cockpit instrument panel is shown in figure 15. Figure 16 shows the controls by which pilot inputs are fed into the CYBER 175 computer. They include the standard helicopter controls: cyclic stick with trim release button and "coolie hat" trim control, collective stick, and antitorque pedals.

The cyclic stick is operated by a three-axis hydraulic control loader which is controlled by the analog computer shown in figure 19. Stick travel at the center of the hand grip is limited by mechanical stops to ±12.7 cm in the lateral direction and ±14.0 cm in the longitudinal direction. The stick dynamics are modeled on the analog computer as second-order systems with the damping chosen by the pilot. The stick force gradient used is 4.4 N/cm in the longitudinal axis and 8.9 N/cm in the lateral axis and was obtained from reference 9. The force the pilot applies to the stick is opposed by the hydraulic control loader and measured by force transducers. The force transducer signals are fed into the analog computer and the stick acceleration is calculated. The acceleration signal is processed together with the actual stick position and a position error signal is formed. This error signal is then sent to the control loader servo which moves the stick. The new stick position is fed through an ADC to the CYBER 175 computer as the pilot's cyclic stick input. The lateral position of the stick is the input x_{lat} in equations (12) and the longitudinal position is the input x_{lon} in equations (12).

In the trimming mode, the CYBER 175 computer uses the trim algorithms discussed subsequently in the section "Trim Calculations" to obtain the trim position of the cyclic stick. This position is fed through a DAC to the control loader analog computer as a command to drive the stick to the trim position.

Activating the trim release button on the cyclic stick or stick trim toggle switch shown in figures 16 and 18 removes the trim force. The stick position at the instant the pilot releases the button or turns the stick trim toggle on becomes the new trim position. The trim position may also be moved by the four-position coolie hat mentioned previously. By moving the coolie hat

in a certain direction, the stick's zero force position is moved in that direction. The trim release button, the stick trim toggle, and the coolie hat are discrete inputs to the CYBER 175 computer.

The analog output from the collective stick, the quantity x_{col} in equations (12), is fed through an ADC to the CYBER 175 computer. The stick travel is limited by mechanical stops to 35.6 cm. A friction collar can be adjusted to vary the stick friction. The trim algorithm calculates the collective-stick trim position. The pilot must then place the collective stick in its trim position, which is evidenced by the turning off of the collective trim light shown in figure 18.

The pedals are driven by the same three-axis hydraulic control loader system which drives the cyclic stick; however, the response characteristics are modeled on the CYBER 175 computer because the frequency response of the pedals is not as high as that of the cyclic stick. The pedal travel is limited by mechanical stops to approximately 10 cm. The pedal dynamics are second order with a force gradient of 62.2 N/cm, as obtained from reference 9. The pedal damping was chosen by the pilot. The operation of the pedal control loader is identical with that of the cyclic stick. Microswitches located on each pedal have the same function as the trim release push button located on the cyclic stick. In the trimming mode, the trim algorithm calculates the trim position for the pedals. These position commands are fed through DAC's to drive the pedals to their trim position.

The remaining pilot controls in the cockpit are discrete inputs to the CYBER 175 computer. They are

Winch control - three-position toggle switch to lengthen or shorten the load cable

Mode control buttons - shown in figure 18; select one of the following modes of operation:

RESET	resets to initial flight conditions
HOLD	holds present flight conditions
OPERATE	starts simulation

AFCS selector buttons - shown in figure 18; select the following options:

AFCS	automatic flight control system on
YAW	heading hold on
ALT	altitude hold on
HOVER	hover hold on

Stick trim switch - two-position toggle switch to turn cyclic-stick-force trim system on and off; shown in figure 18

Load release button - located on the cyclic stick; when pressed, external load is released

Several additional features are included in the cockpit.

The pilot views a visual terrain scene provided by the visual landing display system (VLDS), and a computer-generated load/landing zone scene. Pilots' comments during checkout indicated that a separate and independent computer-generated video display of the sling load and landing zone as viewed by a down-looking TV camera attached to the helicopter at the pilot's location is unacceptable. Many hours of simulation experience with NASA pilots and pilots from industry have shown that an acceptable simulation sling load display can be made by electronically combining the visual terrain scene with the computer-generated scene. The resulting image is then displayed on the video monitor placed in the normal eye-level position. Figure 17 shows the virtual image lens system through which the pilot views the color monitor which displays the visual terrain scene electronically mixed with the down-looking load scene. The virtual image lens causes the pilot's eyes to be focused at infinity. Also, shown in figure 17 is a small black and white monitor which shows the same displays as the pilot's color monitor. The black and white monitor is used by the researcher sitting in the right seat of the cockpit.

An audio generator creates cockpit noise, with one component having a frequency equal to 6 times rotor speed (in rpm) and the other component having white noise with magnitude proportional to the quantity $(V_{as,h} + 24.4)$ m/sec to represent wind noise. These audio signals are output on a speaker in the cockpit with volume level based on pilot comments.

Simulation Software

The simulation software is written in FORTRAN, with some assembly language. It is broken down into primary and secondary overlays with many subroutines and general-purpose functions.

Figure 20 shows the central memory layout with the various overlays. The large block labeled (0,0) represents the base overlay, which requires $40\ 000_8$ storage locations. It contains all variables which must be communicated between overlays, subroutines required by more than one overlay, and some real-time system software.

The primary level overlays (1,0), (2,0), (3,0), and (4,0) share the same memory locations. Their functions are necessarily mutually exclusive. Overlay (1,0) initializes program variables and initializes the real-time system. Overlay (2,0) prints trim sheets or time histories. Overlay (3,0) reads in data for various loads. Overlay (4,0) is the main overlay and contains the real-time loop. It is further described below and in figure 21(a). Secondary level overlays (4,1) to (4,10) are optionally executed by overlay (4,0).

The secondary overlays share the same memory locations. Overlay (4,1) executes static checks; (4,2) contains the load/landing zone display equations; (4,3) contains the trim algorithm and logic; (4,4) contains preprocessing equations, i.e., calculations which can be done out of the real-time loop for a given run; (4,5) checks and prints out function data; (4,6) calculates stability derivatives; (4,7) prints error messages to the console operator; (4,10) calculates linearization derivatives. Of these eight functions, only the load/landing zone display equations are needed in the real-time loop. The others are brought in as necessary between runs.

The real-time overlay (overlay (4,0)) is the main loop, with all the other overlays supporting it. A general flow diagram of the main loop is shown in figure 21(a). This real-time loop consists of three separate loops: reset, hold, and operate. The reset loop is cycled through at Time = 0. The hold loop is selected at any time to hold all simulation variables fixed. The operate loop begins the simulation, calculating and integrating the equations of motion and updating the independent variable time in synchronization with real time, with a step size Δt of 1/32 sec. This rate was selected as the largest time interval allowed by the real-time system which gives accurate results and updates cockpit instruments with no visible jumps.

The block in figure 21(a) labeled (A) represents the section of the reset loop in which various secondary overlays can be selected and executed. For example, when the console operator depresses the trim button, overlay (4,4) is executed to calculate preprocessing equations, and then overlay (4,3) is loaded to execute the trim algorithm. Overlay (4,3) will stay in memory until another option is selected.

Blocks (B) to (E) are cycled through in both hold and reset modes. Block (B) represents the sampling of 5 analog signals (via ADC's) and 27 discrete inputs from the cockpit. These voltages are scaled and the resulting parameters (e.g., stick inputs) saved for later use.

Block (C) represents all the calculations necessary to compute the equations of motion for the helicopter and, optionally, for the load. This block is broken down in figure 21(b), where each block refers to a portion of the previously developed mathematical model. Some of the general-purpose algorithms used in this section are a convolution integration scheme used to represent first- and second-order filters, a linear interpolation scheme for function data table look-ups for functions of one or two variables, and an Euler integrator for use when speed is desirable and accuracy not critical.

Block (D) represents the calculations for the VLDS and Adage displays. The VLDS drive equations are computed, 19 analog signals are output, and 11 analog error signals are fed back. The Adage display equations are computed, and the data are transmitted in digital form to the Adage Graphics Terminal (AGT 130). Further descriptions of the VLDS and Adage displays are given below.

Block (E) represents the scaling of program variables and the outputting of those variables via DAC's and discrete channels. Twenty-nine voltages and 12 discrete outputs are trunked to the simulator cockpit.

Blocks (F) and (G) are only cycled through in the operate mode. Data for the time-history printout are recorded in block (F), every specified number of iterations. These data can be printed later at the researcher's option.

Block (G) represents the integration of the equations of motion. The real-time loop is designed to be as fast as possible, while maintaining good accuracy. The Adams-Bashforth second-order (AB-2), one-pass scheme is very fast, and is accurate enough for this particular simulation, as was shown in the comparison of time-history plots with the independent check program. The AB-2 integration scheme is fully described in reference 12.

The complete real-time loop requires a minimum of 2.5 msec (in reset) and a maximum of 6.2 msec (in operate). The 2.5-msec figure includes only the helicopter with AFCS, whereas the 6.2-msec figure includes the 2.4-m by 2.4-m by 6.1-m load, winds, gust, and so forth. Table III shows a complete breakdown of the required time.

Visual Landing Display System

The visual landing display system (VLDS) consists of a fixed, colored-terrain board system and a movable camera transport and is designed for use with a monitor and virtual image lens system for displaying an "out-the-window" scene in a simulated cockpit. A brief description follows. A more detailed description is given in reference 13.

The 7.3-m by 18.3-m terrain model board of the VLDS includes two airports and surrounding terrain, one at 750/1 scale and the other at 1500/1 scale, and is shown in figure 22. There are a total of five paved runways, from 0.6 km to 3.5 km in length. A helipad is located on the 750/1 airport and is shown in figure 23. It consists of a Maltese cross with a 45-m by 45-m border. The terrain is generally flat, and provision is made for variable visibility, variable cloud-base heights, and day, dusk, and night scenes.

The camera system has a field of view 48° wide and 36° high and uses a 525-line color video raster system. This system provides nominal resolution on the order of 9 minutes of arc. The pilot's eye position and the orientation of the pilot's line of sight out the forward window are both calculated with respect to the simulated runway. These positions and orientation angles (and their rates) are used to drive the camera system. The dynamic characteristics of the VLDS transport system are given in table IV.

Load/Landing Zone Visual Display

The simulation is intended to be used by pilots to evaluate sling load stabilization systems, and since sling load piloting is a visual task, a

realistic display of load motions and landing zone position must be available in the simulated cockpit. Preliminary work with pilots defined the format of the simulation display as follows. The display should show in perspective the three-dimensional outline of the external load, the cable(s), and the Earth-fixed features such as the landing zone and lead-in distance marks. The center line of the display should be located at the cable attachment point on the helicopter and the view should be stabilized in pitch and roll; that is, the view should always be vertically oriented. Load altitude above ground level should be presented in analog form by a pointer and altitude scale, and helicopter pitch and roll attitude bars should be generated to provide the pilot precise attitude information needed while hovering. A sketch of the desired load/landing zone display is given in figure 24.

The load/landing zone computer graphic display is defined by vector end points. These end points are computed by using the formulas developed in equations (97) to (101).

The coordinates of the load c.g. are given with respect to helicopter body axes by

$$\begin{Bmatrix} x_{\ell cg,h} \\ y_{\ell cg,h} \\ z_{\ell cg,h} \end{Bmatrix} = C_h \begin{Bmatrix} x_{\ell cg,e} - x_{hcg,e} \\ y_{\ell cg,e} - y_{hcg,e} \\ z_{\ell cg,e} - z_{hcg,e} \end{Bmatrix} \tag{97}$$

The coordinates of any point p on the load expressed in helicopter body axes are thus given by

$$\begin{Bmatrix} x_{\ell p,h} \\ y_{\ell p,h} \\ z_{\ell p,h} \end{Bmatrix} = \begin{Bmatrix} x_{\ell cg,h} \\ y_{\ell cg,h} \\ z_{\ell cg,h} \end{Bmatrix} + C_h C_\ell{}^T \begin{Bmatrix} x_{\ell p,\ell} \\ y_{\ell p,\ell} \\ z_{\ell p,\ell} \end{Bmatrix} \tag{98}$$

The coordinates of the helicopter viewpoint expressed in Earth axes are given by

$$\begin{Bmatrix} x_{v,e} \\ y_{v,e} \\ z_{v,e} \end{Bmatrix} = \begin{Bmatrix} x_{hcg,e} \\ y_{hcg,e} \\ z_{hcg,e} \end{Bmatrix} + C_h{}^T \begin{Bmatrix} x_{v,h} \\ y_{v,h} \\ z_{v,h} \end{Bmatrix} \tag{99}$$

where $x_{v,h}$, $y_{v,h}$, $z_{v,h}$ are the coordinates of the viewpoint in helicopter axes. Thus, the coordinates of any point p on the Earth with respect to the viewpoint are given in helicopter axes by

$$\begin{Bmatrix} x_{zp,h} \\ y_{zp,h} \\ z_{zp,h} \end{Bmatrix} = C_h \begin{Bmatrix} x_{zp,e} - x_{v,e} \\ y_{zp,e} - y_{v,e} \\ z_{zp,e} - z_{v,e} \end{Bmatrix} \tag{100}$$

where $x_{zp,e}$, $y_{zp,e}$, $z_{zp,e}$ are the coordinates of any point p in Earth axes. Since the load/landing zone display will be shown on a screen, these points must be expressed in the coordinate system of the screen. The following equations are used to transform these points to screen coordinates and to add perspective:

$$\left.\begin{aligned} x_{screen} &= x_{p,h}/z_{p,h} \\ y_{screen} &= y_{p,h}/z_{p,h} \end{aligned}\right\} \tag{101}$$

where $x_{p,h}$, $y_{p,h}$, $z_{p,h}$ are the coordinates at any point p in helicopter axes. The helicopter attitude bars are generated directly in screen coordinates. The data defined in screen coordinates must be clipped at the screen boundary. The clipping algorithm employed is described in reference 14.

The load/landing zone display requirements are met by the Adage Graphics Terminal in conjunction with the CYBER 175 computer. The Adage is an independent, digital, graphics computer with an operator console shown in figure 25. Computations required for the display are performed on the CYBER 175 computer and data are transmitted to the Adage, which generates the display. Sample displays are shown in figures 26 and 27.

Trim Calculations

In order for the simulation to start in an unaccelerated flight condition, it is required that an algorithm that renders certain mathematical model time derivatives zero be available for determining the helicopter attitude and control positions and the load attitude and position with respect to the helicopter. The algorithm used is based on the so-called method of secants and is described in appendix D of reference 15. The algorithm determines the values of the following independent variables: x_{lon}, x_{lat}, x_{col}, x_{ped}, α_f, ϕ_h, θ_h, v_m, v_t, θ_{0t}, α_ℓ, ϕ_ℓ, θ_ℓ, $x_{\ell cg,e}$, $y_{\ell cg,e}$, $z_{\ell cg,e}$ so that the following dependent

variables are approximately zero: $\dot{u}_{cg,h}$, $\dot{v}_{cg,h}$, $\dot{w}_{cg,h}$, $\dot{p}_h$, $\dot{q}_h$, $\dot{r}_h$, $\dot{w}_{hcg,e}$, $\dot{\nu}_m$, $\dot{\nu}_t$, $\dot{\theta}_{0t}$, $\dot{u}_{cg,\ell}$, $\dot{v}_{cg,\ell}$, $\dot{w}_{cg,\ell}$, $\dot{p}_\ell$, $\dot{q}_\ell$, $\dot{r}_\ell$.

For the simulation of the CH-54 helicopter and cargo container the algorithm trims at any specified airspeed from -20 to 100 knots in approximately 1 sec. Values of the major helicopter variables in trim at 0.1, 30, 60, and 90 knots are given in table V. The use of 0.1 knot was to prevent singularities that would occur at exactly zero airspeed.

VERIFICATION AND VALIDATION

Simulation Verification

The simulation software verification was accomplished with an independent check program. The check program was written in FORTRAN and was designed to run in a batch environment. It was developed from the mathematical model independently of the real-time program. As the independent check program is not required to run in real time, a more accurate integration algorithm than AB-2 was selected for this use. This procedure provided a verification of both the programing of the mathematical model and the accuracy of the numerical solution. A Runge-Kutta seventh-order, 13-pass integration algorithm with variable step size was used in the independent check program. This algorithm and its accuracy are described in reference 16.

The check case selected consisted of a 30-sec run, during which the four control inputs were disturbed independently with a half-cycle sine-wave forcing function. The AFCS was off for the first 3 sec, and was cut on and off in 3-sec intervals during the run. This allowed for large, but reasonable, perturbations in the state variables. The check case was run for the helicopter alone at hover and at 60 knots and for the helicopter with sling load at hover and at 60 knots. The time histories of the state variables showed excellent agreement with those from the real-time program, and further analysis proved that the negligible differences were due to integration errors. These errors were small enough to verify that the AB-2 integration scheme was sufficiently accurate for the simulation.

Hardware verification consists of a static check performed before each real-time session. The instruments are checked visually for conformity with static check values. All the control inputs are deflected to their maximum and minimum positions while the console operator monitors the voltages. Finally, all the discrete inputs are activated while the console operator monitors them.

Mathematical Model Validation

The helicopter portion of the previously described mathematical model was validated by comparison of simulated time histories with flight data, analysis of eigenvalues and eigenvectors, and by pilot evaluation.

Eleven simulations were made for comparison with flight time histories, and the results from two of these are shown in figures 28 and 29. In all cases the simulated helicopter mass characteristics were set equal to those of the helicopter that generated the flight time histories. (These flights were conducted at Langley in 1972 in an unrelated sling load project reported in ref. 17.) Table I gives the mass characteristics and other data used in the simulation. The AFCS was off in all cases. When reviewing figures 28 and 29, the reader should keep in mind that the basic helicopter is unstable about each axis, so that any perturbation from trim will result in divergent roll, pitch, and yaw motion because of the dynamic cross coupling. This divergence tends to amplify differences between flight and simulation as time increases. It was the manufacturer's opinion that about 2 or 3 sec of close agreement between simulation and flight data would be all that should be expected.

Figure 28 shows the data for a run in which the helicopter alone was hovering and the pilot made a longitudinal cyclic step input of about 3 cm for approximately 2 sec while holding the other controls approximately fixed. The simulation was trimmed at hover and the control position changes made in flight were duplicated in the simulation by using the recorded control input data. The upper two plots in figure 28 show the longitudinal and lateral cyclic stick motion for the first 5 sec of this case. The pedals moved less than 0.05 cm during this run and the collective stick moved less than 0.09 cm at the grip. The differences in Euler angles and body rates between flight and simulation at time zero noted in the figure were due to trim and flight data bias and should be disregarded throughout the run when comparing these data. Except for the slight roll acceleration reversal noted in the figure at about 3 sec, the data for attitude and angular rates show very close agreement. The helicopter altitude data agreed closely between simulation and flight and showed a decrease of about 1.5 m during the 5-sec period.

Figure 29 shows the data for a run in which the helicopter was flying straight and level at approximately 38 knots and the pilot made a longitudinal cyclic step input of about 2 cm for several seconds followed by a pedal input of about 1 cm and a lateral cyclic input of approximately 2 cm. The same trim airspeed was used in the simulation, and the control position changes made in flight were duplicated in the simulation as before. The upper three plots in figure 29 show the time histories of the flight and simulation control inputs for the first 7 sec of this run. The collective stick was not moved during the 7-sec period shown. The time histories of helicopter altitude and airspeed are given in the fourth and fifth plots, where good agreement is noted between flight and simulation. As for the hover run, the differences in Euler angles and body angular rates at time zero should be disregarded throughout the run when comparing the data. Here the agreement in pitch and yaw data is considered excellent, whereas the agreement in roll data is only fair. The remaining nine comparison cases between flight data and simulation data showed excellent agreement for the first few seconds in each case. In some cases the agreement remained good for several more seconds; in others the agreement degraded slightly, as in the examples shown in figures 28 and 29. In general, the agreement between simulation data and flight data was believed to indicate that the simulation mathematical model is adequate for studying helicopter sling load control systems.

The helicopter was trimmed at 0.1, 30, 60, and 90 knots and the linearization algorithm described in reference 19 was applied to determine the linear system derivative matrices A and B defined in reference 19 and the system eigenvalues and eigenvectors. In order that the time-varying rotor inflow ratios ν_m and ν_t and the tail-rotor effective pitch angle θ_{0t} would not appear as variables in the linear system, 30 iterations with the ν_m, ν_t, and θ_{0t} differential equations (eqs. (26) and (47)) were performed after each state variable perturbation was made so that these three variables would reach semi-steady-state before the linear system derivatives were calculated. The A and B linear system matrices are given in table VI for the four airspeeds. Unpublished derivatives obtained from Sikorsky Aircraft, derivatives calculated by methods given in reference 7, and derivatives given in reference 18 were compared with those in the table and generally good agreement was found.

The eigenvalues and eigenvectors for the system A matrix were calculated and are also given in table VI. The upper half-plane of the loci of eigenvalues at the four airspeeds is shown in figure 30. The eigenvectors were used to identify the eigenvalues with respect to the helicopter modes of motion. The identification is noted on the figure. The real roots ranging from -0.85 to -1.0 are associated with rolling velocity and vertical velocity. The zero at the origin corresponds to the heading angle ψ_h. The root loci were compared with unpublished Sikorsky Aircraft data for a CH-53 helicopter, which is similar to the CH-54, and with data at 60 knots given in reference 18. In general, the loci trends were found to be similar but the agreement in magnitudes was only fair.

The comparison of the linear system matrices and the eigenvalues and eigenvectors obtained from the nonlinear mathematical model with data from other sources indicates that the mathematical model does represent the dynamics of a CH-54 helicopter fairly well.

The sling load portion of the mathematical model was validated by comparing measured frequencies of simulated pendulum, rocking, and bounce motions with theoretical values and by pilot evaluation. The theoretical and measured frequencies of these modes are given in table VII. In each case the theoretical values are based on the assumptions that the helicopter attachment point is fixed in space and that the cable is inelastic except in the bounce mode. In each mode the measured frequencies are slightly higher than the theoretical values. This discrepancy is believed to be due to the motion of the helicopter attachment point and the interaction between the bounce mode and the rocking modes. The agreement is considered adequate.

As mentioned earlier, the suspension system cable spring rate K_{sc} was critical in terms of numerical stability. Trial and error showed that the spring rate had to be selected so that the frequencies associated with the cable stretch would be no higher than 2 Hz. A value of $K_{sc} = 1.8 \times 10^5$ N/m was used with the 4536-kg load, giving a theoretical bounce natural frequency of 1 Hz.

Pilot's Comments

The project test pilot acquired experience in the Army CH-54 helicopter during the flight tests reported in reference 17. This pilot also received additional flight training with long-line sling loads in connection with the present report. Numerous simulated flights both with and without a simulated sling load attached were performed for the purpose of validating the simulation mathematical model.

Several combinations of simulated cyclic stick and pedal force gradients and dynamic characteristics were considered. The set used in this report represent a usable set for the simulation. The VLDS and load/landing zone visual display system described earlier is considered to be marginally adequate for the simulation of helicopter sling load operations. The lack of peripheral visual cues in the horizontal and vertical planes makes hover and transitions to hover especially difficult. The computer-generated load/landing zone display and the VLDS also lack the depth and natural cues that are so useful in actual flight.

The simulated helicopter alone with and without winds and turbulence seemed like a large helicopter in all flight regimes. It seemed underdamped in yaw motions when approaching hover, and its vertical motions seemed much more sensitive to collective movements than those for the actual helicopter. The simulated helicopter seemed slower than the actual helicopter to respond to cyclic step and pulse inputs. Autorotation was simulated and seemed realistic to touchdown.

The simulation with the external load seemed realistic in spite of the visual display shortcomings. Simulated flights with the external load were performed over the entire speed range and the ensuing load motions were observed on the load/landing zone display. In all cases the load motions appeared realistic. The helicopter motions definitely were affected by load motions, and hovering over a spot was very difficult, as it is in actual flight. All normal sling load operations were tried with and without winds and turbulence and were found to be possible to execute but with slightly higher work load than in actual flight. Simulator motion validation was not necessary since it was thought that for studies of sling load stabilization and control system comparison, simulator motion would not be required.

It is thought that the simulation described in the report can be used to compare various systems for stabilizing helicopter sling loads and improving helicopter sling load handling qualities.

CONCLUDING REMARKS

A generalized, full-flight envelope, real-time, piloted visual simulation of a single-rotor helicopter, suspension system, and external load is described and validated for the full flight envelope of the U.S. Army CH-54 helicopter

and cargo container as an example. The mathematical model described uses modified nonlinear classical rotor theory for both the main rotor and tail rotor, nonlinear fuselage aerodynamics, an elastic suspension system, nonlinear load aerodynamics, and a load-ground contact model. The implementation of the mathematical model on a large digital computing system is described, and validation of the simulation is discussed. The mathematical model is validated by (1) comparison of flight data with simulated data; (2) comparison of linearized system coefficient matrices, eigenvalues, and eigenvectors with calculated values, manufacturer's data, and data obtained from flight tests; and (3) by pilot evaluation. A visual landing display system that generates the pilot's forward-looking real-world display is discussed, and a special head-up, down-looking load/landing zone display is described. It was the test pilot's opinion that the simulation described in this report can be used to compare various systems for stabilizing helicopter sling loads and improving helicopter sling load handling qualities.

Langley Research Center
National Aeronautics and Space Administration
Hampton, VA 23665
October 23, 1978

REFERENCES

1. Daniels, Glenn E., ed.: Terrestrial Environment (Climatic) Criteria Guidelines for Use in Aerospace Vehicle Development, 1973 Revision. NASA TM X-64757, 1973.

2. Wilcock, T.; and Thorpe, Ann C.: Flight Simulation of a Wessex Helicopter - A Validation Exercise. C.P. No. 1299, British A.R.C., 1974.

3. Seckel, Edward; and Curtiss, H. C., Jr.: Aerodynamic Characteristics of Helicopter Rotors. Rep. No. 659, Dep. Aerosp. Mech. Sci., Princeton Univ., Dec. 1963.

4. Bailey, F. J., Jr.: A Simplified Theoretical Method of Determining the Characteristics of a Lifting Rotor in Forward Flight. NACA Rep. 716, 1941.

5. Amer, Kenneth B.; and Gustafson, F. B.: Charts for Estimation of Longitudinal-Stability Derivatives for a Helicopter Rotor in Forward Flight. NACA TN 2309, 1951.

6. Gessow, Alfred; and Myers, Garry C., Jr.: Aerodynamics of the Helicopter. Macmillan Co., c.1952. (Republished 1967 by Frederick Ungar Pub. Co.)

7. Seckel, Edward: Stability and Control of Airplanes and Helicopters. Academic Press, Inc., c.1964.

8. Amer, Kenneth B.: Theory of Helicopter Damping in Pitch or Roll and a Comparison With Flight Measurements. NACA TN 2136, 1950.

9. Bailes, Edward E.; Diekmann, Vernon L.; Watts, Joseph C.; and Henderson, John C.: Instrument-Flight-Rules Capability Evaluation - CH-54B (TARHE) Helicopter. USAASTA Proj. No. 71-01, U.S. Army, Dec. 1972. (Available from DDC as AD 908 656.)

10. Laub, Georgene H.; and Kodani, Hifu M.: Wind Tunnel Investigation of Aerodynamic Characteristics of Scale Models of Three Rectangular Shaped Cargo Containers. NASA TM X-62,169, 1972.

11. Liu, David T.: In-Flight Stabilization of Externally Slung Helicopter Loads. USAAMRDL Tech. Rep. 73-5, U.S. Army, 1973.

12. Wilson, John W.; and Steinmetz, George C. (With Appendix A by Roland L. Bowles): Analysis of Numerical Integration Techniques for Real-Time Digital Flight Simulation. NASA TN D-4900, 1968.

13. Parrish, R. V.; Rollins, J. D.; and Martin, Dennis J., Jr.: Visual/Motion Simulation of CTOL Flare and Touchdown Comparing Data Obtained From Two Model Board Display Systems. AIAA Paper 76-1709, Apr. 1976.

14. Newman, William M.; and Sproull, Robert F.: Principles of Interactive Computer Graphics. McGraw-Hill Book Co., 1973, pp. 123-124.

15. Houck, Jacob A.; Gibson, Lucille H.; and Steinmetz, George G.: A Real-Time Digital Computer Program for the Simulation of a Single-Rotor Helicopter. NASA TM X-2872, 1974.

16. Fehlberg, Erwin: Classical Fifth-, Sixth-, Seventh-, and Eighth-Order Runge-Kutta Formulas With Stepsize Control. NASA TR R-287, 1968.

17. DiCarlo, Daniel J.; Kelley, Henry L.; and Yenni, Kenneth R.: An Exploratory Flight Investigation of Helicopter Sling-Load Placements Using a Closed-Circuit Television as a Pilot Aid. NASA TN D-7776, 1974.

18. Tomaine, Robert L.: Flight Data Identification of Six Degree-of-Freedom Stability and Control Derivatives of a Large "Crane" Type Helicopter. NASA TM X-73958, 1976.

19. Dieudonne, James E.: Description of a Computer Program and Numerical Technique for Developing Linear Perturbation Models From Nonlinear Systems Simulation. NASA TM-78710, 1978.

TABLE I.- VALUES OF PARAMETERS FOR CH-54 HELICOPTER

[Subscripts m and t denote main and tail rotor]

$x_{mr,h}$, m	-0.33
$y_{mr,h}$, m	0
$z_{mr,h}$, m	-2.26
$x_{tr,h}$, m	-13.74
$y_{tr,h}$, m	-0.84
$z_{tr,h}$, m	-2.22
$x_{wt,h}$, m	-0.51
$y_{wt,h}$, m	0
$z_{wt,h}$, m	-0.37
$x_{ps,h}$, m	5.77
$y_{ps,h}$, m	-0.53
$z_{ps,h}$, m	0.11
FSCG, m	8.20
WLCG, m	4.28
BLCG, m	0
$x_{a,h}$, m	0.33
$y_{a,h}$, m	0
$z_{a,h}$, m	0.24
$I_{xx,h}$, kg-m^2	39 800
$I_{yy,h}$, kg-m^2	2.04×10^5
$I_{zz,h}$, kg-m^2	1.78×10^5
$I_{xz,h}$, kg-m^2	11 400
e_m, m	0.610
I_{bm}, kg-m^2	4.75×10^3
$\tilde{M}_{wm}$, kg-m	715.0
R_m, m	10.97
$\tau_{\lambda m}$, sec	0.20
δ_{3m}, rad	0
θ_{1m}, rad	-0.183
σ_m	0.115

TABLE I.- Continued

θ_{sm}, rad	-0.0524
ϕ_{sm}, rad	0
Ω_o, rpm	184.5
G_{gov}, N-m/(rad/sec)	85 160
K_{dgov}, N-m/(rad/sec)	1.32×10^5
K_m, N-m/(rad/sec)	1.572×10^6
K_{gov}, N-m/(rad/sec)	833.3
I_{pt}, kg-m^2	4325
I_{mr}, kg-m^2	31 310
τ_{eng}, sec	0.50
$G_{B\theta}$, rad/rad	0.281
$G_{A\phi}$, rad/rad	-0.133
G_{Bxlon}, rad/m	0.363
G_{Axlat}, rad/m	0.475
$G_{\theta ch}$, rad/m	-0.00037
G_{Bq}, rad/(rad/sec)	0.727
G_{Ap}, rad/(rad/sec)	-0.096
$G_{\theta tr}$, rad/(rad/sec)	0.335
$G_{\theta t\psi}$, rad/rad	0.133
K_{c0}, rad	0.128
K_{c1}, rad/m	0.955
K_{c2}, rad/m	1.361
K_{c3}, rad/m	-0.096
K_{c4}, rad/m	0.824
K_{c5}, rad	0.0494
K_{c6}, rad/m	3.64
K_{c7}, rad/m	1.09
K_{fe}, N-m/N	0.0243
K_{sc}, N/m	1.8×10^5
m_h, kg	13 610
a_t, per rad	5.73

TABLE I.- Concluded

B_t	0.92
b_t	4
c_t, m	0.343
e_t, m	0.127
I_{bt}, kg-m^2	13.88
$\tilde{M}_{wt}$, kg-m	11.84
$\tau_{\lambda t}$, sec	0.20
$\tau_{\delta 3t}$, sec	0.20
θ_{lt}, rad	-0.140
R_t, m	2.44
σ_t	0.179
θ_{st}, rad	0
ϕ_{st}, rad	1.57
δ_{3t}, rad	0.78
B_m	0.97
b_m	6
c_m, m	0.661
a_m, per rad	5.73
ω_a, rad/sec	14.0
ρ_a	1.0
e_{kt}	1.8
e_{kf}	0.5
i_{to}	0

TABLE II.- VALUES OF PARAMETERS FOR 2.4-m BY 2.4-m BY 6.1-m

CARGO CONTAINER

$I_{xx\ell}$, kg-m^2	1124
$I_{yy\ell}$, kg-m^2	14 610
$I_{zz\ell}$, kg-m^2	14 610
$I_{xz\ell}$, kg-m^2	0
m_ℓ, kg	4536
$x_{a,\ell}$, m	0
$y_{a,\ell}$, m	0
$z_{a,\ell}$, m	-6.1
$x_{c1,\ell}$, m	3.05
$y_{c1,\ell}$, m	-1.22
$z_{c1,\ell}$, m	1.22
$x_{c2,\ell}$, m	3.05
$y_{c2,\ell}$, m	1.22
$z_{c2,\ell}$, m	1.22
$x_{c3,\ell}$, m	-3.05
$y_{c3,\ell}$, m	1.22
$z_{c3,\ell}$, m	1.22
$x_{c4,\ell}$, m	-3.05
$y_{c4,\ell}$, m	-1.22
$z_{c4,\ell}$, m	1.22
V_o, m/sec	0.305
μ_f	0.25
K_p, N/m	45 000
K_v, N/(m/sec)	7100
ℓ_{c0}, m	30.5

TABLE III.- REQUIRED COMPUTER TIMES

Calculation	Computer time, msec, for mode -		
	Reset	Hold	Operate
Helicopter only	2.5	1.7	2.0
Cockpit interface	.3	.2	.3
Winds and gusts	.0	.1	.2
Visual landing display system	.7	.7	.8
Load/suspension system	.9	.9	1.0
Load landing zone visual display	1.5	1.4	1.9
Total simulation	5.9	5.0	6.2

TABLE IV.- DYNAMIC CHARACTERISTICS OF VLDS

Drive	Frequency, rad/sec	Damping ratio
Altitude	27.9	0.64
Lateral	24.1	.6
Longitudinal	22.8	.3
Roll	18.6	.7
Pitch	24.3	.7
Yaw	22.6	.7

TABLE V.- TRIMMED VALUES OF MAJOR VARIABLES AT FOUR AIRSPEEDS

[Subscripts m and t denote main and tail rotor]

Variable	Value at airspeed, knots, of -			
	0.1	30	60	90
x_{lon}, cm	-5.48	-3.98	-2.55	-1.10
x_{lat}, cm	-0.12	-1.09	-1.79	-2.79
x_{ped}, cm	2.04	1.05	0.06	-0.48
x_{col}, cm	16.4	13.7	11.9	13.1
A'_{IC}, deg	-0.95	-1.27	-1.50	-2.03
B'_{IC}, deg	-4.27	-3.10	-1.99	-0.86
θ_{0m}, deg	16.3	14.9	13.8	14.5
θ_{0t}, deg	15.2	12.0	9.3	8.8
$u_{as,h}$, m/sec	0.05	15.4	30.9	46.2
$v_{as,h}$, m/sec	0	0	0	0
$w_{as,h}$, m/sec	-0.001	-0.45	-1.46	-4.06
ϕ_h, deg	-2.8	-2.2	-1.6	-1.7
θ_h, deg	-1.3	-1.7	-2.7	-5.0
α_f, deg	-29.9	-15.0	-6.9	-6.9
β_f, deg	0	0	0	0
$V_{as,h}$, m/sec	0.05	15.4	30.9	46.3
a_{1sm}, deg	4.3	4.1	3.8	3.7
b_{1sm}, deg	-0.95	-0.73	-0.49	-0.53
a_{0sm}, deg	5.82	5.59	5.31	5.35
a_{1st}, deg	0.004	0.83	0.96	1.33
b_{1st}, deg	0.001	0.18	0.26	0.44
a_{0st}, deg	2.14	1.57	1.09	1.14
$X_{mr,h}$, N	-2947	-2605	-1828	-1635
$Y_{mr,h}$, N	-2204	-1831	-1796	-1955
$Z_{mr,h}$, N	-1.33×10^5	-1.34×10^5	-1.34×10^5	-1.34×10^5
$L_{mr,h}$, N-m	-1.93×10^4	-1.53×10^4	-1.21×10^4	-1.33×10^4

TABLE V.- Continued

Variable	Value at airspeed, knots, of -			
	0.1	30	60	90
$M_{mr,h}$, N-m	-939	-3420	-7734	-8927
$N_{mr,h}$, N-m	1.20×10^5	9.44×10^4	7.54×10^4	8.37×10^4
$X_{tr,h}$, N	-0.62	-99.6	-91.4	-138.4
$Y_{tr,h}$, N	8699	6868	5414	5912
$Z_{tr,h}$, N	0.17	25.3	19.4	29.5
$L_{tr,h}$, N-m	1.93×10^4	1.53×10^4	1.21×10^4	1.33×10^4
$M_{tr,h}$, N-m	-2288	-721	-254	59.2
$N_{tr,h}$, N-m	-1.20×10^5	-9.4×10^4	-7.4×10^4	-8.09×10^4
$X_{f,h}$, N	-0.010	-1161	-4401	-9904
$Y_{f,h}$, N	0	0	0	0
$Z_{f,h}$, N	-0.018	1046	376.5	865.3
$L_{f,h}$, N-m	0	0	0	0
$M_{f,h}$, N-m	3227	4142	7988	8868
$N_{f,h}$, N-m	-0.003	-340.1	-1252	-2824
h_h, m	30.5	30.5	30.5	30.5
ρ, kg/m^3	1.23	1.23	1.23	1.23
$\bar{q}$, N/m^2	0.0016	145.6	582.3	1310
Ω_m, rpm	184.5	184.5	184.5	184.5
C_{Tm}	0.00640	0.00646	0.00642	0.00643
μ_m	2.42×10^{-4}	0.0726	0.145	0.216
ν_m	0.0566	0.0388	0.0217	0.0146
λ_m	-0.057	-0.041	-0.031	-0.042
Q_{am}, N-m	1.19×10^5	9.43×10^4	7.51×10^4	8.33×10^4

TABLE V.- Concluded

Variable	Value at airspeed, knots, of -			
	0.1	30	60	90
T_m, N	1.33×10^5	1.34×10^5	1.33×10^5	1.33×10^5
H_m, N	89.9	2381	4198	6628
J_m, N	5.04	1135	1683	2775
Ω_t, rpm	835.6	835.6	835.6	835.6
C_{Tt}	0.00838	0.00662	0.00522	0.00570
μ_t	2.41×10^{-4}	0.0724	0.145	0.217
ν_t	0.0647	0.0400	0.0179	0.0131
λ_t	-0.065	-0.040	-0.018	-0.013
Q_{at}, N-m	2291	1291	724	653
T_t, N	8699	6868	5414	5912
H_t, N	0.624	100.2	92.2	140.4
J_t, N	0.16	22.4	15.1	17.2
$\dot{p}_h$, $1/sec^2$	-3.6×10^{-7}	-6.5×10^{-9}	3.8×10^{-8}	-1.4×10^{-7}
$\dot{q}_h$, $1/sec^2$	1.2×10^{-6}	-1.9×10^{-7}	2.3×10^{-8}	5.4×10^{-8}
$\dot{r}_h$, $1/sec^2$	5.9×10^{-7}	-1.2×10^{-8}	8.4×10^{-8}	-2.8×10^{-7}
$\dot{u}_h$, m/sec^2	2.1×10^{-9}	2.3×10^{-8}	2.1×10^{-9}	2.4×10^{-9}
$\dot{v}_h$, m/sec^2	-8.5×10^{-9}	2.4×10^{-12}	8.5×10^{-8}	3.3×10^{-7}
$\dot{w}_h$, m/sec^2	1.5×10^{-9}	6.9×10^{-8}	1.8×10^{-9}	2.1×10^{-8}
$w_{hcg,e}$, m/sec . . .	-3.4×10^{-12}	-1.8×10^{-11}	-5.2×10^{-11}	-4.2×10^{-10}
$\dot{\theta}_{0t}$, deg/sec	-2×10^{-5}	-2.5×10^{-5}	-1×10^{-5}	0
$\dot{\nu}_m$	-1.5×10^{-7}	0	0	0
$\dot{\nu}_t$	-1×10^{-7}	0	0	0

TABLE VI.- HELICOPTER LINEAR SYSTEM MATRICES, EIGENVALUES, AND EIGENVECTORS

(a) Values at 0.1 knot

TRIMMED VELOCITY = .1 KNOTS 7 POINT FORMULA 30 ITERATIONS

INDEPENDENT VARIABLE TOTAL INCREMENTS

$\dot{u}_{cg,h}$	.3048E-01	B'_{IC}	.1745E-02
$\dot{v}_{cg,h}$	.3048E-01	A'_{IC}	.1745E-02
$\dot{w}_{cg,h}$	.3048E-01	θ_{Om}	.1745E-02
$\dot{p}_h$	.1745E-02	θ_{ct}	.1745E-02
$\dot{q}_h$	.1745E-02		
$\dot{r}_h$	.1745E-02		
$\dot{\phi}_h$	.1745E-02		
$\dot{\theta}_h$	.1745E-02		
$\dot{\psi}_h$	.1745E-02		

A MATRIX

	$u_{cg,h}$	$v_{cg,h}$	$w_{cg,h}$	p_h	q_h	r_h	ϕ_h	θ_h	ψ_h
$\dot{u}_{cg,h}$	-.1396E-01	-.7327E-02	-.8304E-02	-.1647E-01	.2527E+00	.1701E-02	.1824E-09	-.9804E+01	-.1487E-18
$\dot{v}_{cg,h}$	.7121E-02	-.2995E-01	-.5138E-02	.1519E+00	-.7543E+00	.1966E+00	.9792E+01	-.1056E-01	.1487E-18
$\dot{w}_{cg,h}$	-.9204E-02	-.5904E-02	-.3337E+00	-.1788E-01	-.3789E-01	-.1012E-01	.4775E+00	.2165E+00	-.7667E-17
$\dot{p}_h$	.1361E-01	-.3444E-01	-.3684E-02	-.7563E+00	-.1262E+01	.7811E-01	-.5367E-06	-.5082E-20	-.5082E-20
$\dot{q}_h$	.5272E-02	.2554E-02	-.6207E-02	.1254E+00	-.2170E+00	-.5994E-02	.3961E-07	0.	0.
$\dot{r}_h$	.1061E-02	.1585E-01	.8314E-02	-.2209E-01	-.6732E-01	-.2458E+00	.1178E-05	-.1491E-18	-.1491E-18
$\dot{\phi}_h$	0.	0.	0.	.1000E+01	.1077E-02	-.2209E-01	0.	0.	0.
$\dot{\theta}_h$	0.	0.	0.	0.	.9988E+00	.4871E-01	0.	0.	0.
$\dot{\psi}_h$	0.	0.	0.	0.	-.4872E-01	.9991E+00	0.	0.	0.

B MATRIX

	B'_{IC}	A'_{IC}	θ_{Om}	θ_{ct}
$\dot{u}_{cg,h}$	.9754E+01	.7238E-13	-.2019E+01	-.5409E-03
$\dot{v}_{cg,h}$	.2823E-03	.9767E+01	-.1508E+01	.4165E+01
$\dot{w}_{cg,h}$	.5282E+00	-.7667E-17	-.9098E+02	.1378E-03
$\dot{p}_h$	.1965E-03	.2015E+02	-.7471E+00	.1941E+01
$\dot{q}_h$	-.3857E+01	-.8009E-10	-.1554E+01	-.9576E-01
$\dot{r}_h$	-.4245E-03	.1191E+01	.7857E+01	-.4260E+01
$\dot{\phi}_h$	0.	0.	0.	0.
$\dot{\theta}_h$	0.	0.	0.	0.
$\dot{\psi}_h$	0.	0.	0.	0.

REAL PARTS OF EIGENVALUES

ROLL(R)	SHORT PERIOD(SP)		SPIRAL(S)	HEADING(H)	PHUGOID(P)		DUTCH ROLL(DR)	
-.84932E+00	-.63450E+00	-.33748E+00	-.20704E+00	-.22678E-17	.10130E+00	.10130E+00	.11451E+00	.11451E+00

IMAG PARTS OF EIGENVALUES

0.	0.	0.	0.	0.	.32528E+00	-.32528E+00	.56938E+00	-.56938E+00

EIGENVECTORS

	$u_{cg,h}$	$v_{cg,h}$	$w_{cg,h}$	p_h	q_h	r_h	ϕ_h	θ_h	ψ_h
R	.30032E+00	.94308E+00	.81523E-01	.68313E-01	-.19306E-01	-.26074E-01	-.81086E-01	.24199E-01	.29564E-01
SP	-.58893E+00	-.79722E+00	-.86512E-01	-.31491E-01	.21029E-01	.37822E-01	.50912E-01	-.36006E-01	-.57939E-01
	-.69560E+00	-.12582E+00	-.64738E+00	.11696E-02	.30674E-02	.91051E-01	.24837E-02	-.22219E-01	-.26910E+00
S	-.26956E+00	.45238E+00	-.69506E-01	.63069E-02	-.71732E-02	.17156E+00	-.12123E-01	-.57536E-02	-.82955E+00
H	-.16901E-16	-.12536E-16	-.22201E-16	-.50138E-19	.11043E-18	-.22646E-17	.19108E-20	.39610E-19	.10000E+01
P	-.67355E+00	.11649E+00	.29888E-01	.13957E-02	-.10800E-01	-.61240E-02	.13586E-01	-.13253E-01	-.40960E-01
	-.62623E+00	-.36919E+00	.10529E-01	.40902E-02	-.64847E-03	-.12918E-01	-.43968E-03	.29952E-01	.44354E-02
DR	.12076E+00	.40355E+00	.29663E-01	.76050E-03	.42716E-02	-.13903E-01	.58937E-01	-.11665E-02	-.38743E-01
	.10955E-01	-.90221E+00	-.19436E-01	.34255E-01	-.43170E-03	-.20157E-01	.99701E-02	-.65386E-02	.16969E-01

TABLE VI.- Continued

(b) Values at 30 knots

TRIMMED VELOCITY = 30.0 KNOTS 7 POINT FORMULA 30 ITERATIONS

INDEPENDENT VARIABLE TOTAL INCREMENTS

$u_{cg,h}$	.3048E-01	B'_{IC}	.1745E-02
$v_{cg,h}$	.3048E-01	A'_{IC}	.1745E-02
$w_{cg,h}$	.3048E-01	θ_{Om}	.1745E-02
p_h	.1745E-02	θ_{ct}	.1745E-02
q_h	.1745E-02		
r_h	.1745E-02		
ϕ_h	.1745E-02		
θ_h	.1745E-02		
ψ_h	.1745E-02		

A MATRIX

	$u_{cg,h}$	$v_{cg,h}$	$w_{cg,h}$	p_h	q_h	r_h	ϕ_h	θ_h	ψ_h
$\dot{u}_{cg,h}$	-.2809E-01	-.6359E-02	-.1224E-01	-.1199E-01	.8423E+00	.8240E-03	.2675E-07	-.9802E+01	.9088E-19
$\dot{v}_{cg,h}$	.1265E-01	-.6052E-01	-.9035E-02	-.4713E+00	-.8463E+00	-.1508E+02	.9795E+01	-.1073E-01	.1872E-20
$\dot{w}_{cg,h}$	-.2238E+00	-.1553E-01	-.5558E+00	-.3334E-01	.1580E+02	-.5409E-02	.3702E+00	.2840E+00	.2324E-20
$\dot{p}_h$	.1642E-01	-.1596E-01	-.9701E-03	-.8808E+00	-.1324E+01	.1562E+00	-.1655E-06	.3970E-21	.3970E-21
$\dot{q}_h$	.1720E-02	.5378E-03	-.8478E-02	.1222E+00	-.2409E+00	-.2656E-02	.1255E-07	-.9741E-20	-.9741E-20
$\dot{r}_h$	-.9055E-02	.2371E-01	.5737E-02	-.7425E-02	-.4336E-01	-.3949E+00	.3567E-06	-.3812E-20	-.3812E-20
$\dot{\phi}_h$	0.	0.	0.	.1000E+01	.1095E-02	-.2897E-01	0.	0.	0.
$\dot{\theta}_h$	0.	0.	0.	0.	.9993E+00	.3777E-01	0.	0.	0.
$\dot{\psi}_h$	0.	0.	0.	0.	-.3779E-01	.9997E+00	0.	0.	0.

B MATRIX

	B'_{IC}	A'_{IC}	θ_{Om}	θ_{ct}
$\dot{u}_{cg,h}$	.1005E+02	.6638E-07	-.3256E+01	-.1122E+00
$\dot{v}_{cg,h}$	.1351E+00	.9850E+01	-.4579E+00	.3819E+01
$\dot{w}_{cg,h}$	.8364E+01	.3094E-05	-.8723E+02	.2839E-01
$\dot{p}_h$	.1314E-01	.2021E+02	.1162E+01	.1789E+01
$\dot{q}_h$	-.3750E+01	.3747E-07	-.9385E+00	-.1902E-01
$\dot{r}_h$	-.8849E-01	.1193E+01	.6510E+01	-.3898E+01
$\dot{\phi}_h$	0.	0.	0.	0.
$\dot{\theta}_h$	0.	0.	0.	0.
$\dot{\psi}_h$	0.	0.	0.	0.

REAL PARTS OF EIGENVALUES

ROLL(R)	SPIRAL(S)	HEADING(H)	PHUGOID(P)		DUTCH ROLL(DR)		SHORT PERIOD(SP)	
-.89431E+00	-.51224E-01	.11270E-18	.62776E-01	.62776E-01	-.12986E+00	-.12986E+00	-.54060E+00	-.54060E+00

IMAG PARTS OF EIGENVALUES

0.	0.	0.	.28606E+00	-.28606E+00	.66800E+00	-.66800E+00	.42172E+00	-.42172E+00

EIGENVECTORS

	$u_{cg,h}$	$v_{cg,h}$	$w_{cg,h}$	p_h	q_h	r_h	ϕ_h	θ_h	ψ_h
R	-.16631E+00	-.66433E+00	-.71209E+00	-.95506E-01	.97492E-02	.36125E-01	.10795E+00	-.12419E-01	-.39971E-01
S	.71857E-01	-.57018E+00	-.12758E-01	.20985E-02	.15405E-02	-.41684E-01	-.64578E-01	.68174E-03	.81465E+00
H	.12908E-17	.26637E-17	-.58547E-18	.32664E-20	-.42549E-20	.11257E-18	.18715E-18	.42156E-20	.10000E+01
P	-.60510E+00	-.41138E+00	.98880E-01	.39694E-02	-.69572E-02	-.76027E-02	-.63714E-02	-.11347E-01	-.56697E-02
	-.56526E+00	-.34447E+00	.12227E+00	-.28307E-02	-.18088E-02	-.15808E-03	-.16018E-01	.22817E-01	.24407E-01
DR	.77529E-02	.93523E+00	.12311E-01	-.15319E-01	-.86558E-03	.21823E-01	.28139E-02	.17297E-02	-.41951E-01
	.34118E-01	.34241E+00	.49796E-01	-.18702E-02	.21279E-02	-.24761E-01	.23334E-01	-.27533E-03	-.24554E-01
SP	-.41644E-01	-.51365E+00	.28407E+00	-.24127E-01	.17039E-01	.10898E-01	.39045E-01	-.17990E-01	.76034E-02
	-.40177E+00	.81604E-01	-.69323E+00	.12842E-01	.14830E-02	.21678E-01	.78622E-02	-.18289E-01	-.34053E-01

TABLE VI.- Continued

(c) Values at 60 knots

TRIMMED VELOCITY = 60.0 KNOTS 7 POINT FORMULA 30 ITERATIONS

INDEPENDENT VARIABLE TOTAL INCREMENTS

$u_{cg,h}$	.3048E-01	B'_{IC}	.1745E-02
$v_{cg,h}$	.3048E-01	A'_{IC}	.1745E-02
$w_{cg,h}$	.3048E-01	θ_{Om}	.1745E-02
p_h	.1745E-02	θ_{ct}	.1745E-02
q_h	.1745E-02		
r_h	.1745E-02		
ϕ_h	.1745E-02		
θ_h	.1745E-02		
ψ_h	.1745E-02		

A MATRIX

	$u_{cg,h}$	$v_{cg,h}$	$w_{cg,h}$	p_h	q_h	r_h	ϕ_h	θ_h	ψ_h
$\dot{u}_{cg,h}$	-.3330E-01	-.4792E-02	-.1466E-01	-.8590E-02	.1939E+01	.2016E-02	.2714E-07	-.9795E+01	-.3356E-20
$\dot{v}_{cg,h}$	.6410E-02	-.9340E-01	-.1445E-01	-.1637E+01	-.8464E+00	-.3037E+02	.9792E+01	-.1262E-01	-.9036E-21
$\dot{w}_{cg,h}$	-.1251E+00	-.2696E-01	-.7800E+00	-.5264E-01	.3092E+02	-.1117E-02	.2661E+00	.4646E+00	-.2582E-19
$\dot{p}_h$	.1269E-01	.4809E-03	.5033E-02	-.9786E+00	-.1317E+01	.2433E+00	.1102E-06	-.7412E-21	-.7412E-21
$\dot{q}_h$	.3674E-02	-.1469E-02	-.1098E-01	.1196E+00	-.2723E+00	.1300E-03	.1770E-08	-.1959E-20	-.1959E-20
$\dot{r}_h$	-.5580E-02	.3119E-01	.1871E-02	.1288E-01	-.5417E-01	-.5570E+00	-.2561E-06	.1059E-19	.1059E-19
$\dot{\phi}_h$	0.	0.	0.	.1000E+01	.1289E-02	-.4743E-01	0.	0.	0.
$\dot{\theta}_h$	0.	0.	0.	0.	.9996E+00	.2716E-01	0.	0.	0.
$\dot{\psi}_h$	0.	0.	0.	0.	-.2719E-01	.1001E+01	0.	0.	0.

B MATRIX

	B'_{IC}	A'_{IC}	θ_{Om}	θ_{ct}
$\dot{u}_{cg,h}$	.1038E+02	.5083E-05	-.4717E+01	-.1668E+00
$\dot{v}_{cg,h}$	.4378E+00	.9800E+01	-.1391E+00	.4478E+01
$\dot{w}_{cg,h}$	.2248E+02	.1866E-03	-.1034E+03	.3579E-01
$\dot{p}_h$	-.1322E+00	.2017E+02	.2833E+01	.2117E+01
$\dot{q}_h$	-.3564E+01	.2530E-05	-.6393E+00	.2769E-01
$\dot{r}_h$	.1022E-01	.1192E+01	.5376E+01	-.4560E+01
$\dot{\phi}_h$	0.	0.	0.	0.
$\dot{\theta}_h$	0.	0.	0.	0.
$\dot{\psi}_h$	0.	0.	0.	0.

REAL PARTS OF EIGENVALUES

ROLL(R)	HEADING(H)	SPIRAL(S)	PHUGOID(P)		SHORT PERIOD(SP)		DUTCH ROLL(DR)	
-.95639E+00	-.68986E-20	.56569E-01	.27343E-01	.27343E-01	-.60458E+00	-.60458E+00	-.33015E+00	-.33015E+00

IMAG PARTS OF EIGENVALUES

0.	0.	0.	.27284E+00	-.27284E+00	.57861E+00	-.57861E+00	.98819E+00	-.98819E+00

EIGENVECTORS

	$u_{cg,h}$	$v_{cg,h}$	$w_{cg,h}$	p_h	q_h	r_h	ϕ_h	θ_h	ψ_h
R	-.74926E-01	-.33428E+00	-.92509E+00	-.10735E+00	.35915E-02	.33338E-01	.11390E+00	-.47007E-02	-.34782E-01
H	.22279E-18	-.41880E-18	-.56071E-19	-.32693E-21	.18718E-21	-.68883E-20	-.25535E-19	-.77534E-21	.10000E+01
S	.10978E+00	-.72060E+00	.28991E-02	-.91584E-02	.10039E-02	-.37901E-01	-.13010E+00	-.46014E-03	-.67099E+00
P	-.42859E+00	-.29200E-02	.66278E-01	-.12421E-02	-.15230E-02	.47124E-02	.85820E-02	.26334E-01	.44468E-02
	.86452E+00	.21797E+00	.12442E+00	.25476E-02	.73736E-02	.94845E-03	.62392E-02	.77499E-02	-.16991E-01
SP	-.29349E+00	.20949E+00	-.79964E+00	.13746E-01	.29456E-02	.94079E-02	.95119E-02	-.17344E-01	-.17874E-01
	-.32067E-01	.17384E+00	-.44271E+00	.24850E-01	-.17320E-01	-.12341E-01	-.32931E-01	.12592E-01	.25430E-02
DR	-.27560E-01	.13054E+00	-.93108E-01	.71137E-02	-.27208E-02	.30520E-01	-.70329E-02	-.67308E-03	-.68489E-02
	.61961E-02	.98461E+00	.45431E-01	-.57054E-02	-.14440E-02	.26645E-02	-.33807E-02	.21382E-02	-.28695E-01

TABLE VI.- Concluded

(d) Values at 90 knots

TRIMMED VELOCITY = 90.0 KNOTS 7 POINT FORMULA 30 ITERATIONS

INDEPENDENT VARIABLE TOTAL INCREMENTS

$u_{cg,h}$	.3048E-01	B'_{IC}	.1745E-02
$v_{cg,h}$	.3048E-01	A'_{IC}	.1745E-02
$w_{cg,h}$	.3048E-01	θ_{Om}	.1745E-02
p_h	.1745E-02	θ_{ct}	.1745E-02
q_h	.1745E-02		
r_h	.1745E-02		
ϕ_h	.1745E-02		
θ_h	.1745E-02		
ψ_h	.1745E-02		

A MATRIX

	$u_{cg,h}$	$v_{cg,h}$	$w_{cg,h}$	p_h	q_h	r_h	ϕ_h	θ_h	ψ_h
$\dot{u}_{cg,h}$	-.4276E-01	-.5663E-02	-.1729E-01	-.9421E-02	.4478E+01	-.1404E-04	.3563E-07	-.9769E+01	-.9294E-20
$\dot{v}_{cg,h}$	.5430E-02	-.1233E+00	-.2212E-01	-.4238E+01	-.7714E+00	-.4560E+02	.9764E+01	-.2559E-01	-.1859E-19
$\dot{w}_{cg,h}$	-.7645E-01	-.4154E-01	-.9147E+00	-.8078E-01	.4606E+02	.1644E-02	.2911E+00	.8582E+00	.1652E-19
$\dot{p}_h$	.1159E-01	.1586E-01	.9965E-02	-.9689E+00	-.1245E+01	.3070E+00	.2939E-06	.2965E-20	.2965E-20
$\dot{q}_h$	.3025E-02	-.3043E-02	-.1129E-01	.1174E+00	-.2824E+00	.9356E-03	-.4026E-08	-.6353E-21	-.6353E-21
$\dot{r}_h$	-.4397E-02	.3452E-01	.5326E-02	.2505E-01	-.5239E-01	-.6505E+00	-.6670E-06	-.1863E-19	-.1863E-19
$\dot{\phi}_h$	0.	0.	0.	.1000E+01	.2619E-02	-.9785E-01	0.	0.	0.
$\dot{\theta}_h$	0.	0.	0.	0.	.9996E+00	.2980E-01	0.	0.	0.
$\dot{\psi}_h$	0.	0.	0.	0.	-.2992E-01	.1003E+01	0.	0.	0.

B MATRIX

	B'_{IC}	A'_{IC}	θ_{Om}	θ_{ct}
$\dot{u}_{cg,h}$	.1099E+02	.2015E-04	-.6631E+01	-.2725E+00
$\dot{v}_{cg,h}$	.1002E+01	.9810E+01	-.2125E+00	.5161E+01
$\dot{w}_{cg,h}$	.3828E+02	.6357E-03	-.1196E+03	.5712E-01
$\dot{p}_h$	-.4119E+00	.2018E+02	.4555E+01	.2462E+01
$\dot{q}_h$	-.3550E+01	.5326E-05	.1023E+00	.7364E-01
$\dot{r}_h$	-.9386E-01	.1192E+01	.5798E+01	-.5249E+01
$\dot{\phi}_h$	0.	0.	0.	0.
$\dot{\theta}_h$	0.	0.	0.	0.
$\dot{\psi}_h$	0.	0.	0.	0.

	ROLL(R)	HEADING(H)	SPIRAL(S)	PHUGOID(P)		SHORT PERIOD(SP)		DUTCH ROLL(DR)	
REAL PARTS OF EIGENVALUES	-.95300E+00	-.29866E-19	.89335E-01	.10409E-01	.10409E-01	-.64693E+00	-.64693E+00	-.42291E+00	-.42291E+00
IMAG PARTS OF EIGENVALUES	0.	0.	0.	.22610E+00	-.22610E+00	.67716E+00	-.67716E+00	.12965E+01	-.12965E+01
EIGENVECTORS	$u_{cg,h}$	$v_{cg,h}$	$w_{cg,h}$	p_h	q_h	r_h	ϕ_h	θ_h	ψ_h
R	.29092E-01	.49194E-01	.98748E+00	.95330E-01	.72726E-04	-.30462E-01	-.10284E+00	.87635E-03	.32075E-01
H	.37692E-18	.33163E-19	-.16052E-19	-.26148E-20	.88667E-21	-.29738E-19	-.13788E-18	-.21832E-20	.10000E+01
S	.21475E+00	-.83181E+00	.27103E-02	-.23195E-01	.10484E-02	-.40927E-01	-.21936E+00	-.19235E-02	-.46004E+00
P	.64875E+00	-.41069E-01	.21558E-01	.10165E-03	.28680E-02	-.64187E-02	-.28201E-01	-.19128E-01	.46048E-03
	-.73004E+00	-.10497E+00	-.17524E+00	-.63853E-02	-.44674E-02	.27021E-03	-.42750E-02	-.12713E-01	.28886E-01
SP	-.21021E-01	.14479E+00	-.48032E+00	.17289E-01	-.14425E-01	-.75577E-02	-.21204E-01	.87571E-02	.10441E-02
	.22966E+00	-.23859E+00	.79791E+00	-.10829E-01	-.24841E-02	-.55357E-02	-.61986E-02	.13260E-01	.95640E-02
DR	-.14162E-01	-.97265E+00	-.84000E-01	.37789E-02	.17078E-02	-.35652E-04	.86201E-02	-.22888E-02	.18409E-01
	-.24333E-01	.17057E+00	-.12472E+00	.15910E-01	-.35086E-02	.26185E-01	-.57325E-02	-.56925E-03	-.59382E-02

TABLE VII.- THEORETICAL AND MEASURED FREQUENCIES OF LOAD MOTIONS

Mode	Frequency	
	Theoretical, Hz	Measured, Hz
Vertical bounce	1.0	1.2
Longitudinal pendulum	.083	.097
Lateral pendulum	.083	.091
Longitudinal rocking	.58	.74
Lateral rocking	1.1	1.4

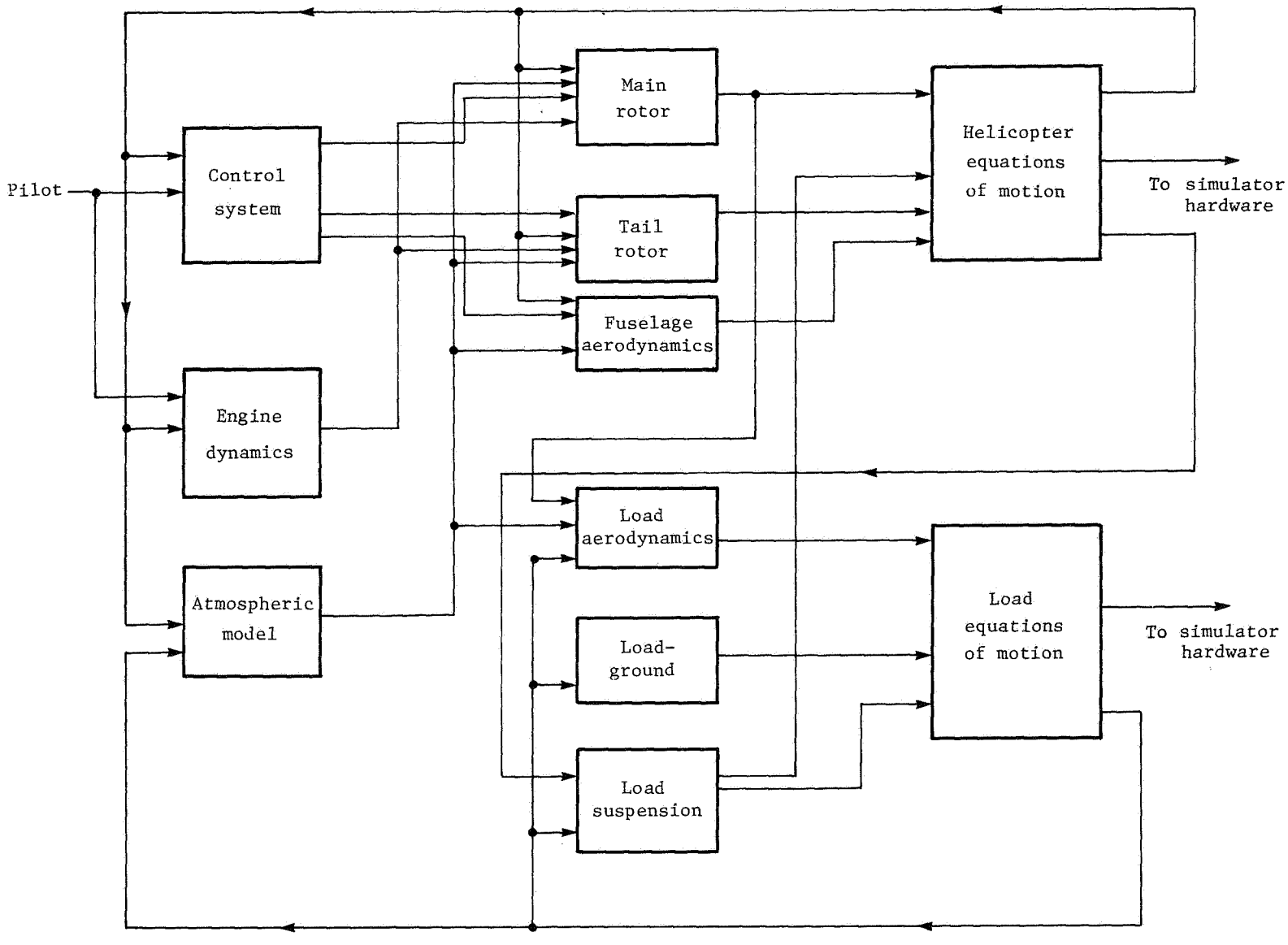

(a) Generalized block diagram.

Figure 1.- Simulation mathematical model block diagram.

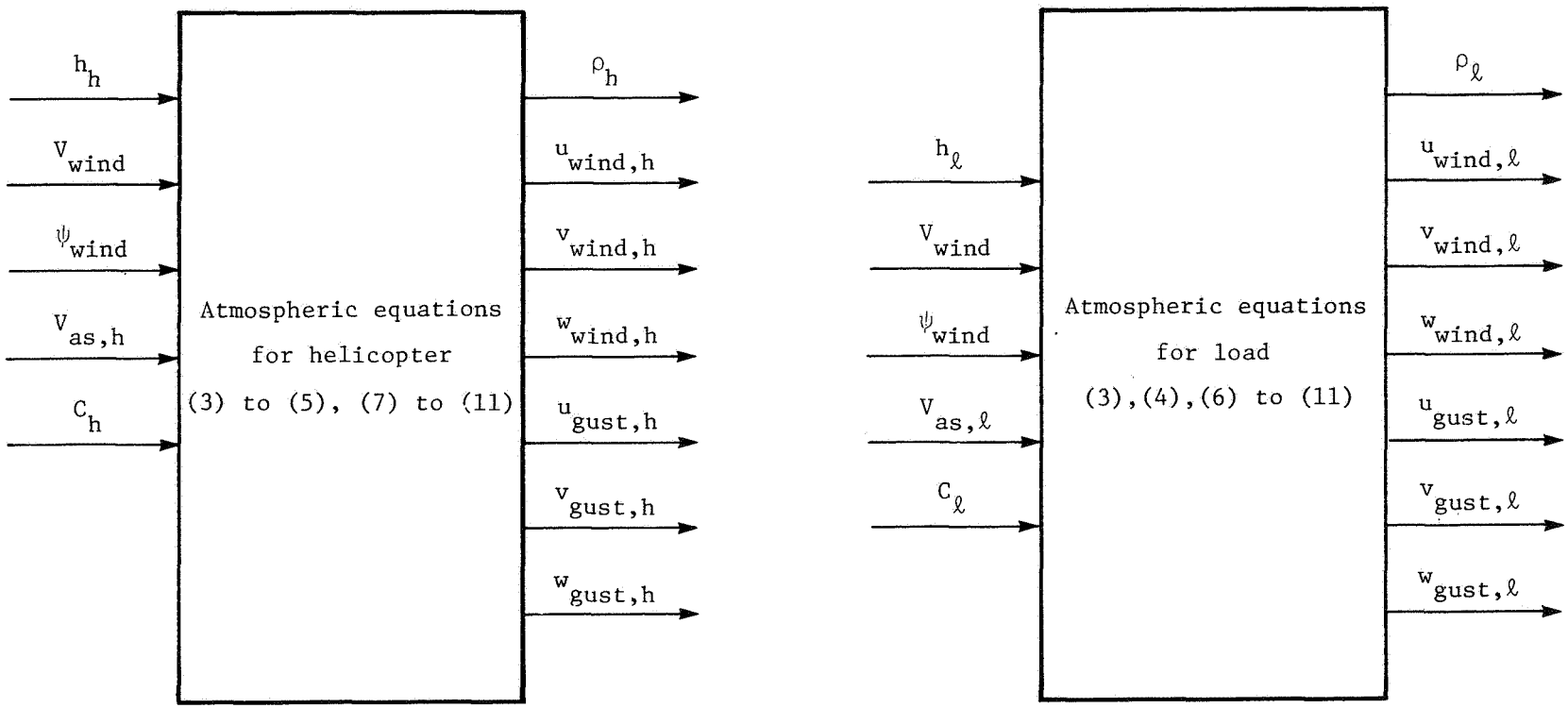

(b) Atmospheric model.

Figure 1.- Continued.

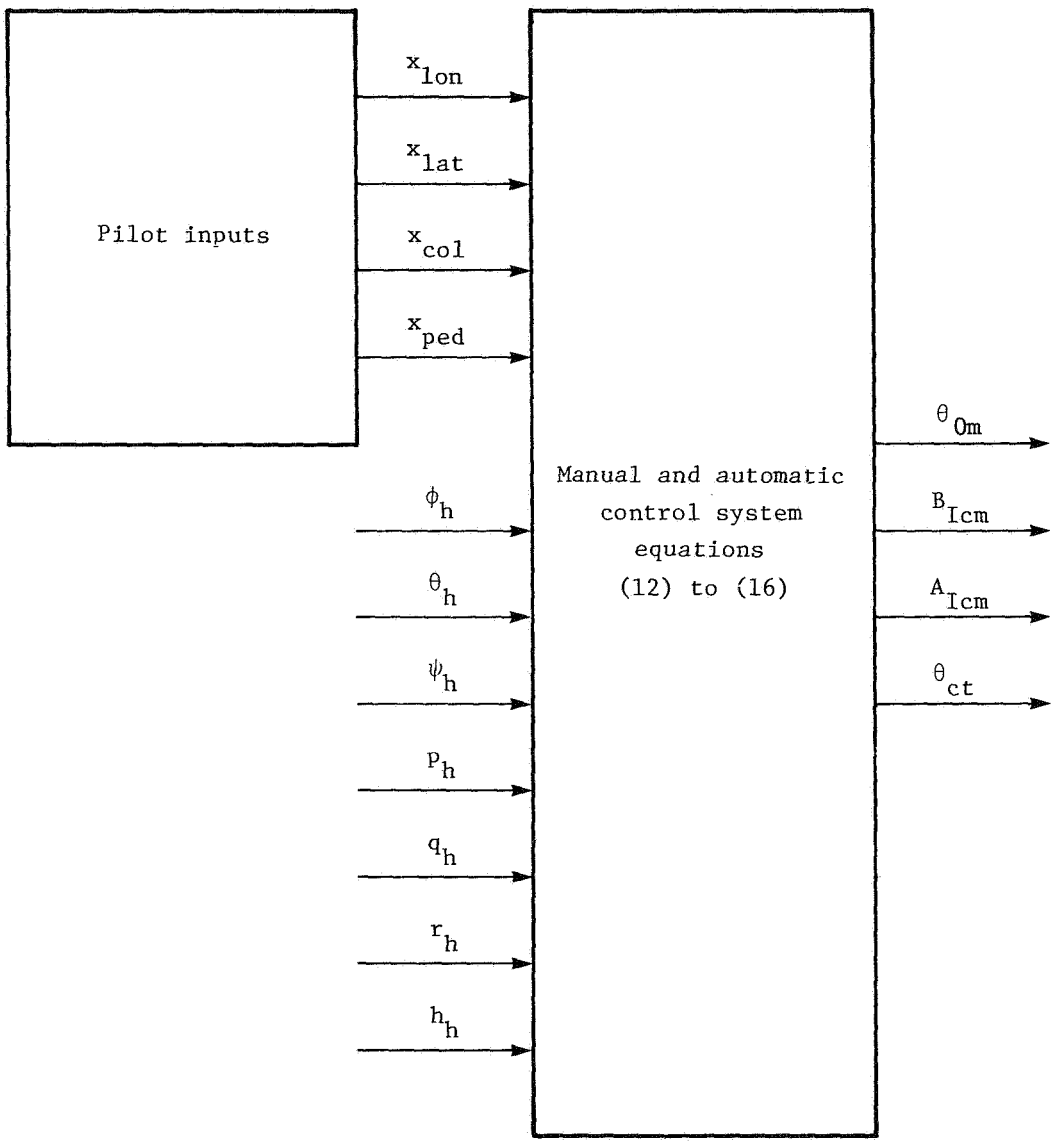

(c) Control system model.

Figure 1.- Continued.

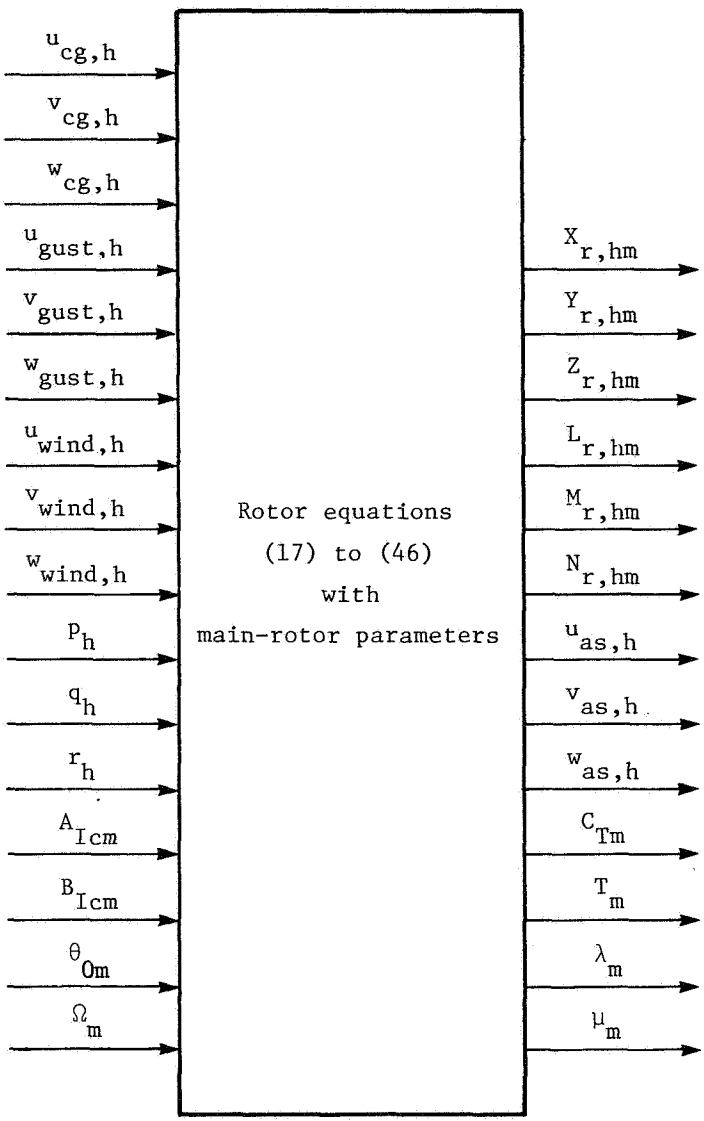

(d) Main-rotor (subscript m) model.

Figure 1.- Continued.

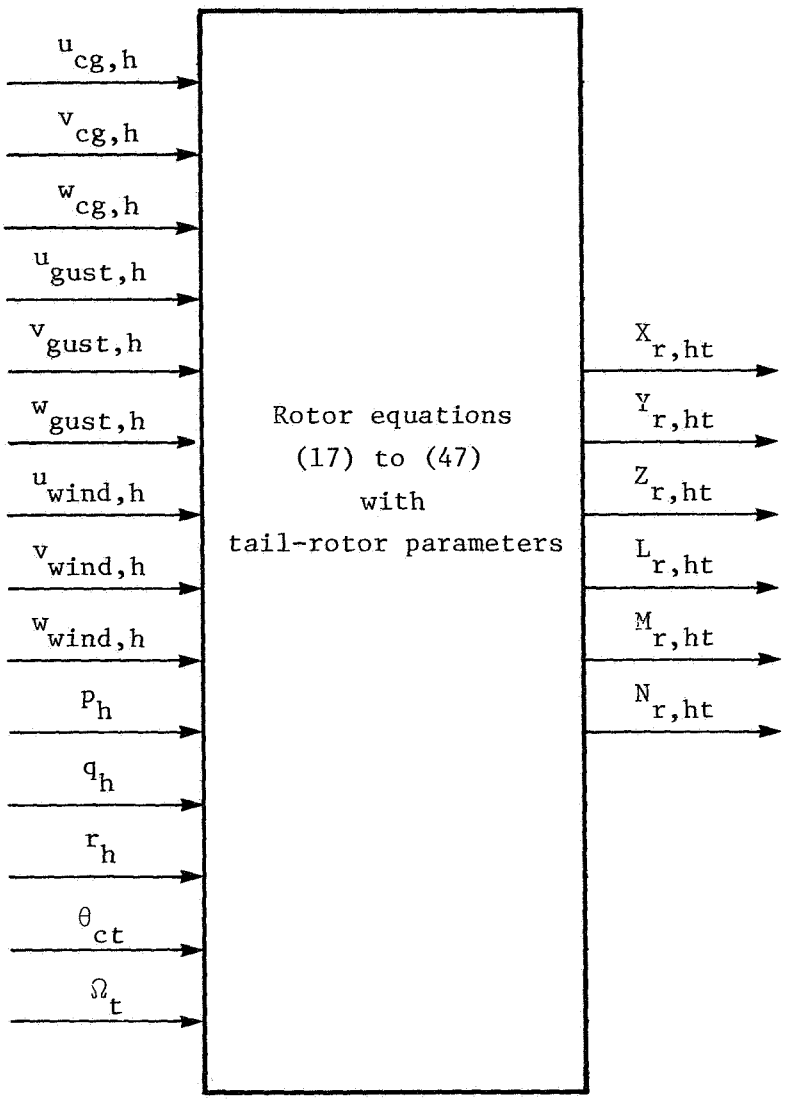

(e) Tail-rotor (subscript t) model.

Figure 1.- Continued.

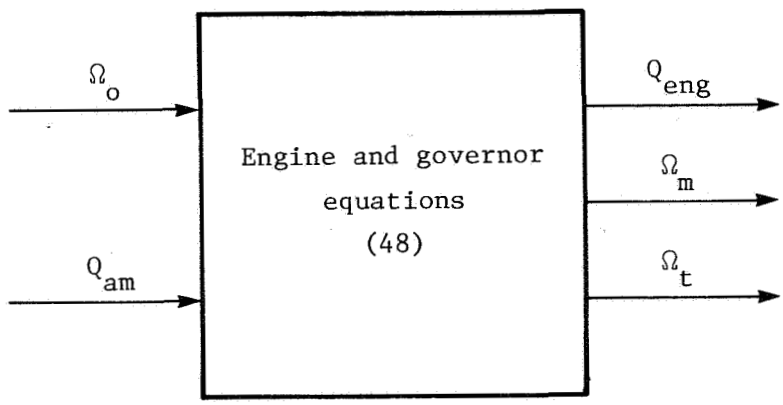

(f) Engine dynamics and governor model.

Figure 1.- Continued.

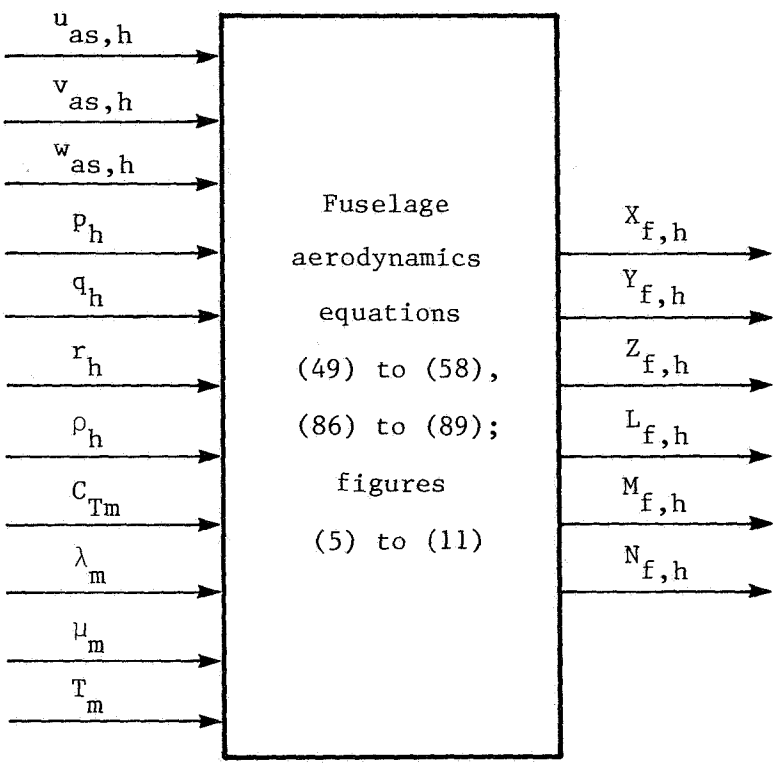

(g) Fuselage aerodynamics model.

Figure 1.- Continued.

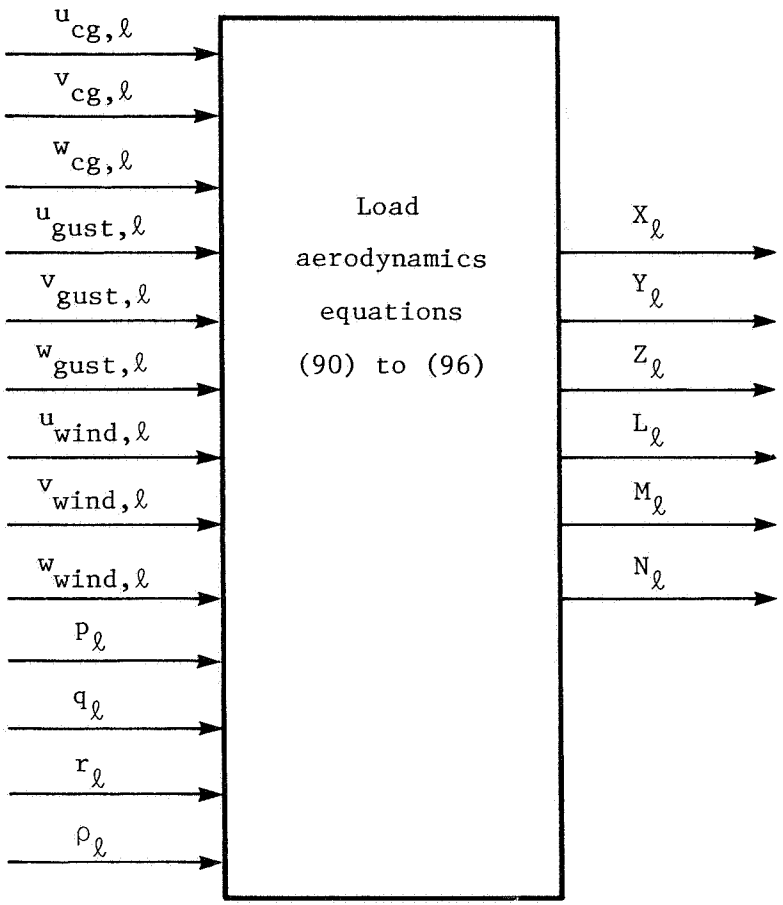

(h) Load aerodynamics model.

Figure 1.- Continued.

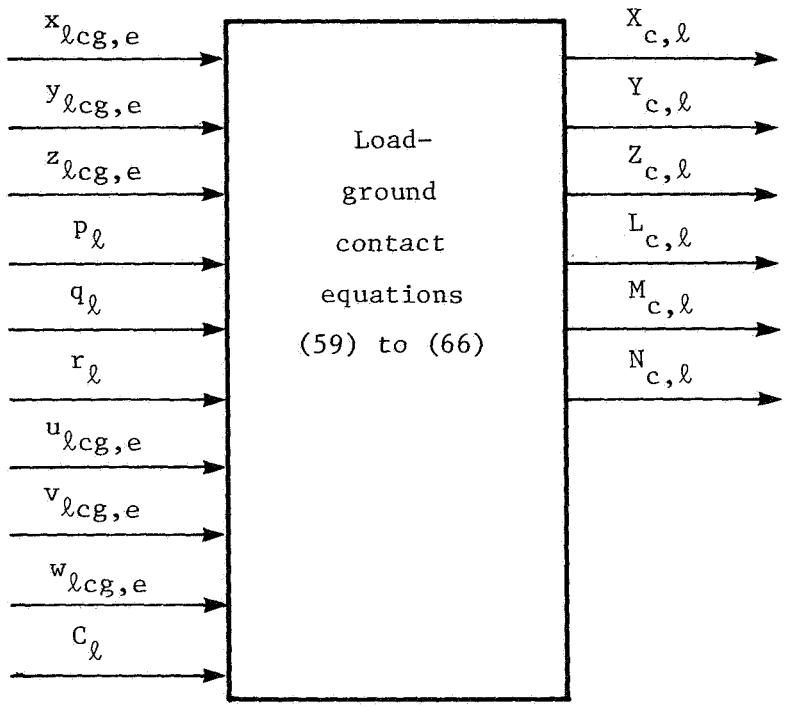

(i) Load-ground contact model.

Figure 1.- Continued.

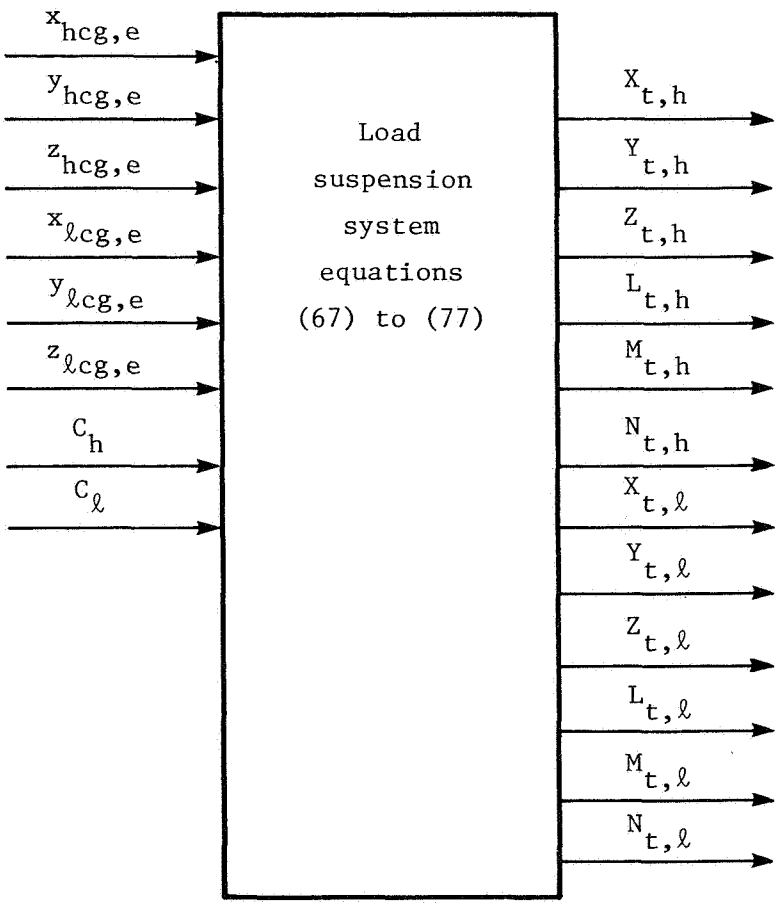

(j) Load suspension model.

Figure 1.- Continued.

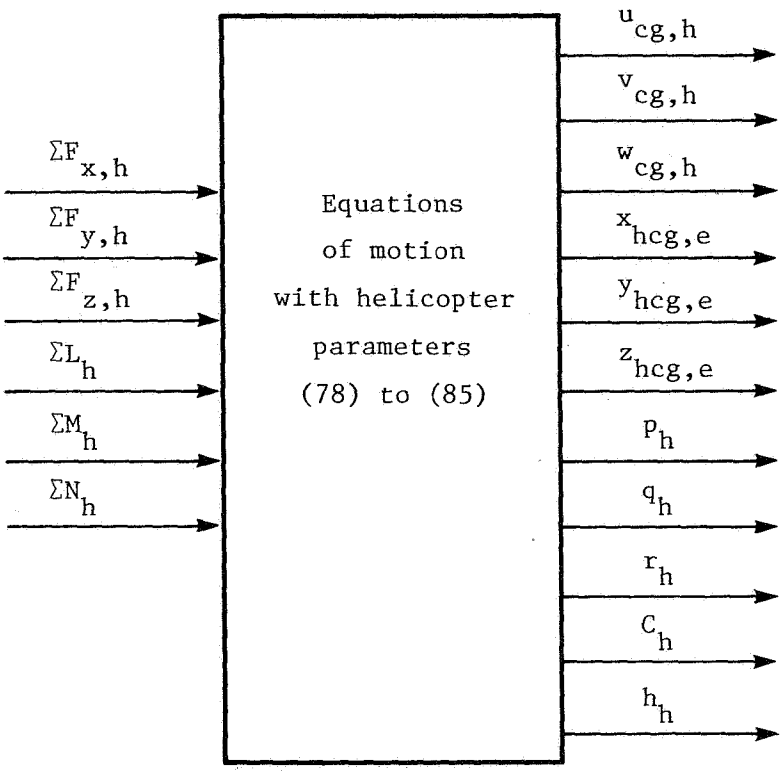

(k) Helicopter equations of motion.

Figure 1.- Continued.

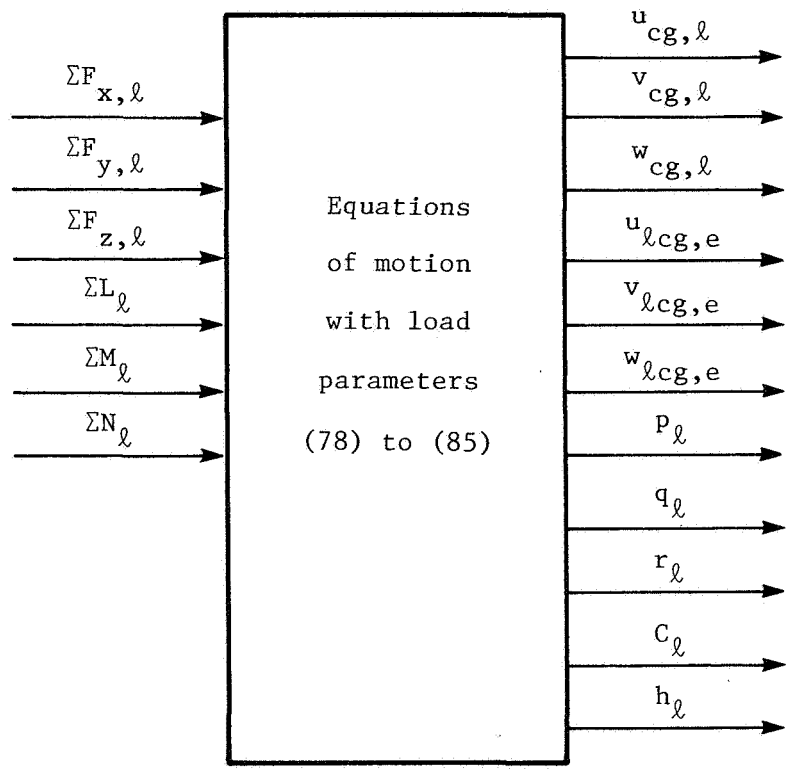

(ℓ) Load equations of motion.

Figure 1.- Concluded.

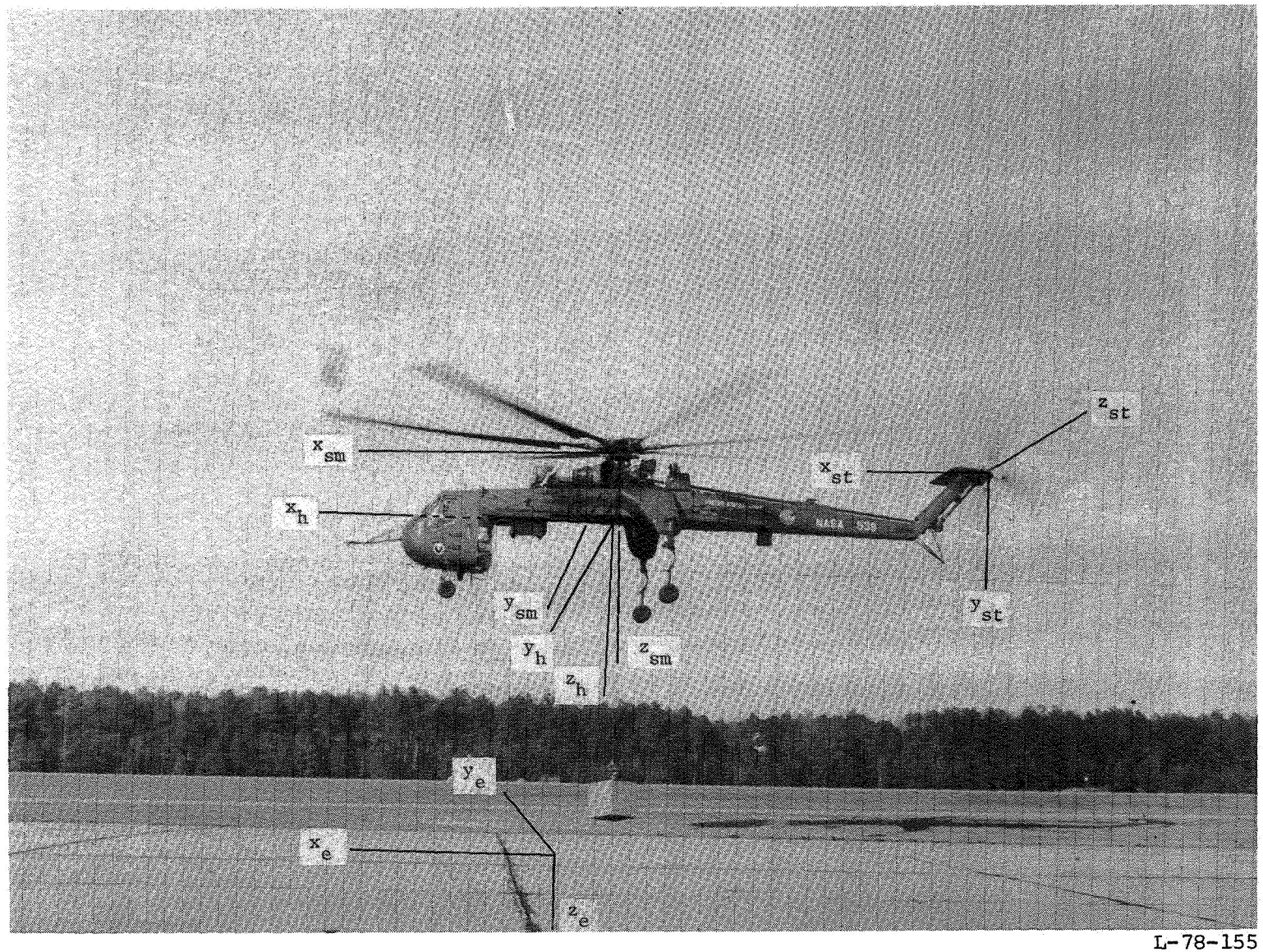

L-78-155

Figure 2.- U.S. Army CH-54 helicopter and concrete block load, showing helicopter body axes, main- and tail-rotor shaft axes, and Earth axes.

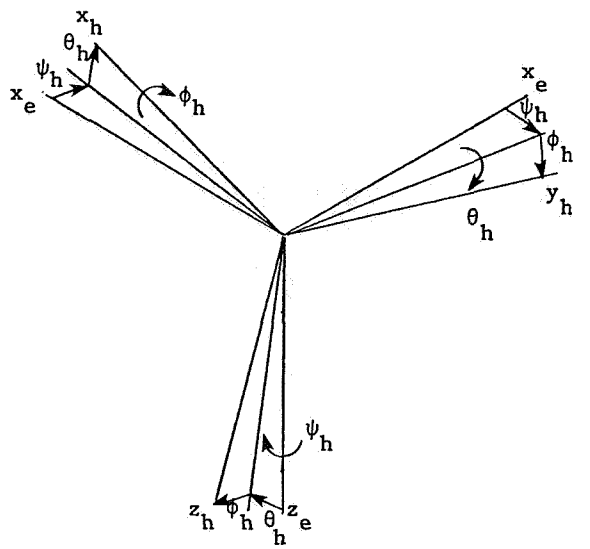

(a) Body axes.

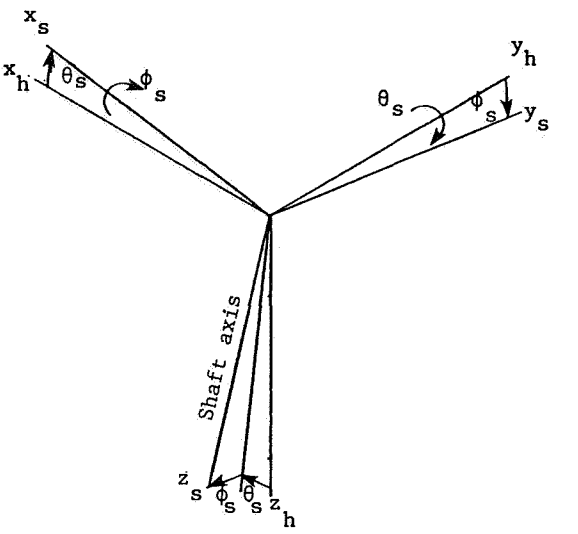

(b) Shaft axes.

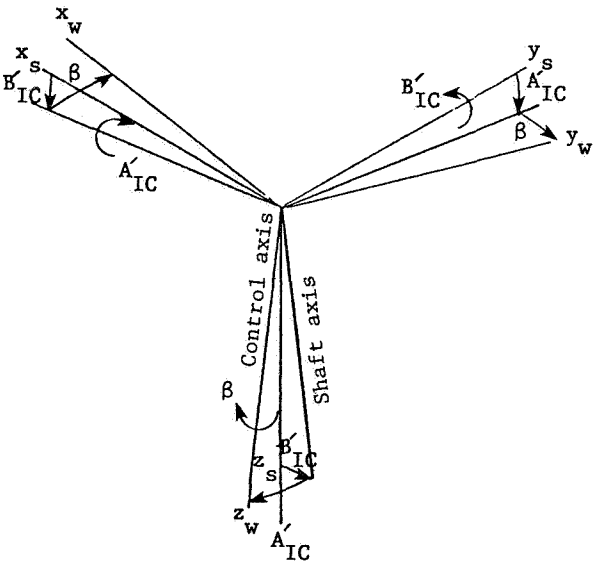

(c) Control axes.

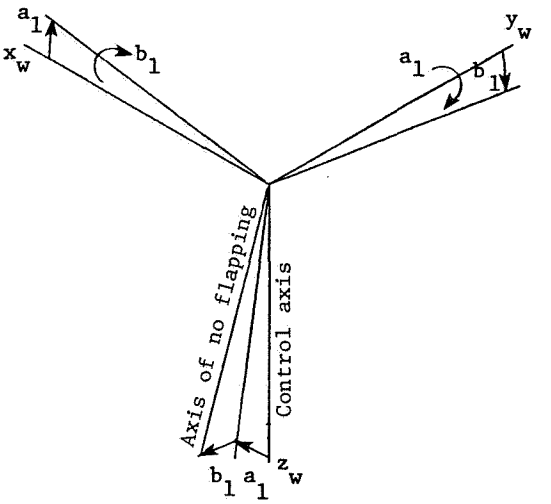

(d) Flapping angles.

Figure 3.- Helicopter body axes, shaft axes, control axes, and flapping angle definitions.

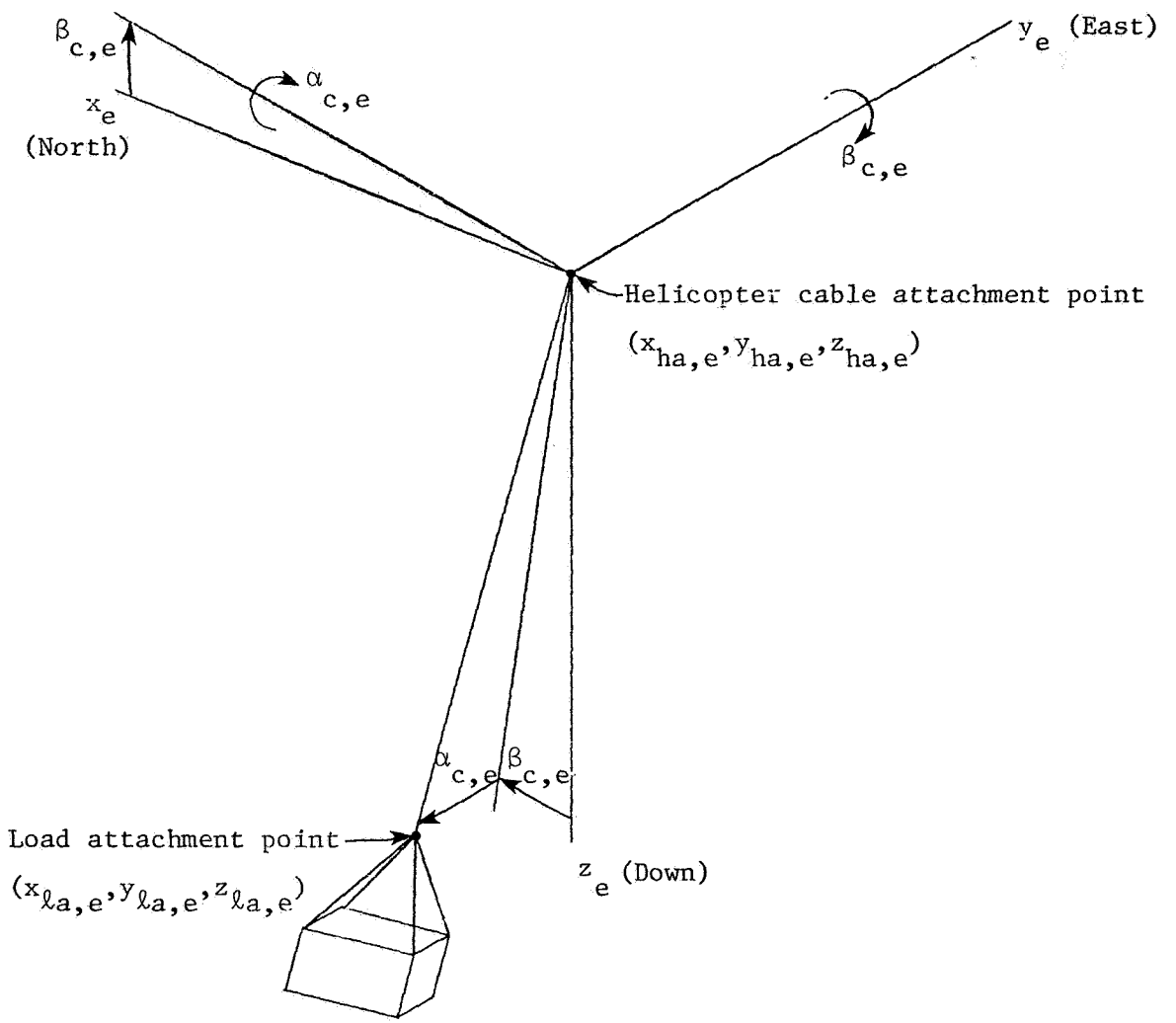

Figure 4.- Load suspension cable angle definitions.

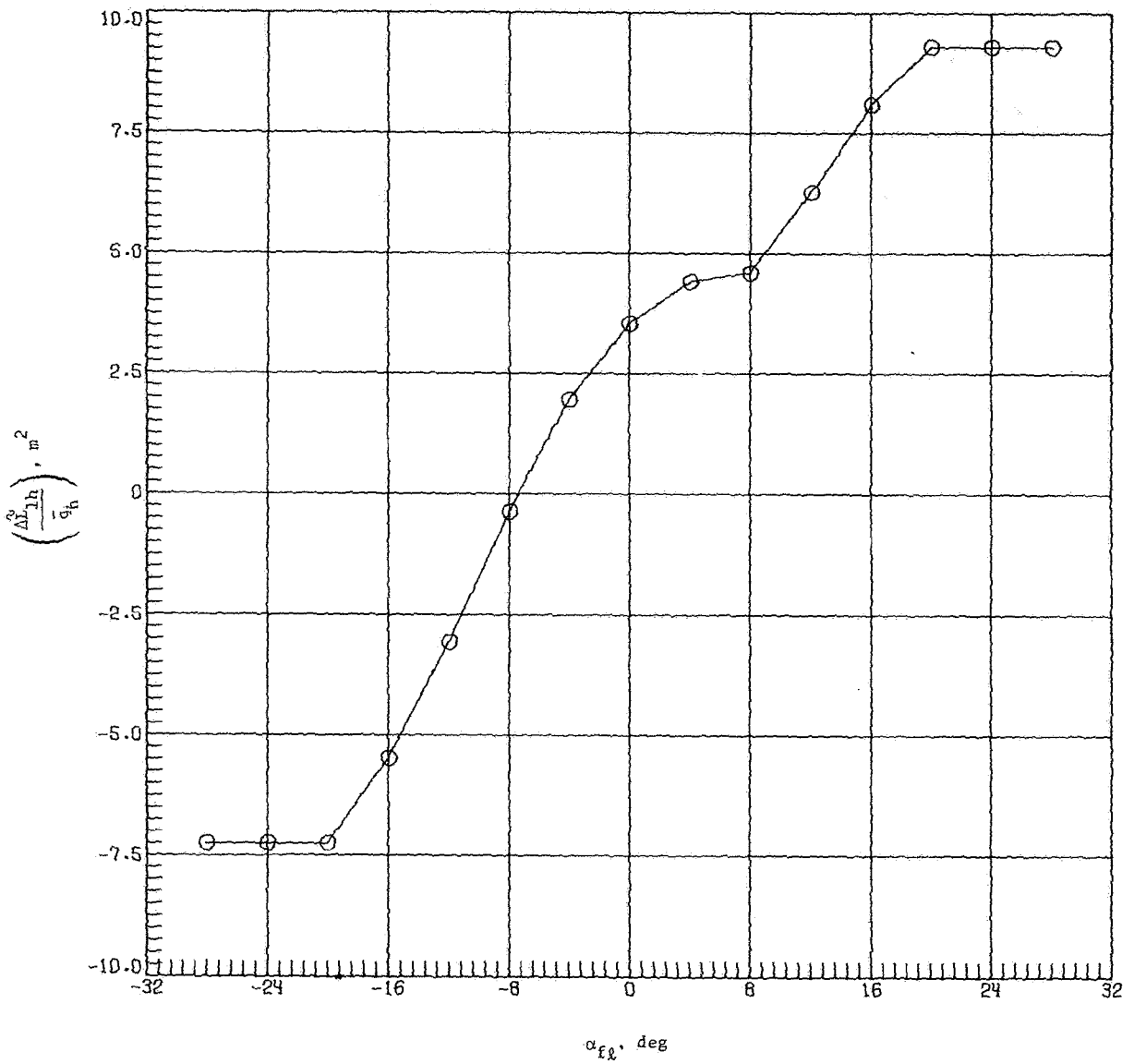

Figure 5.- Fuselage incremental lift as a function of angle of attack.

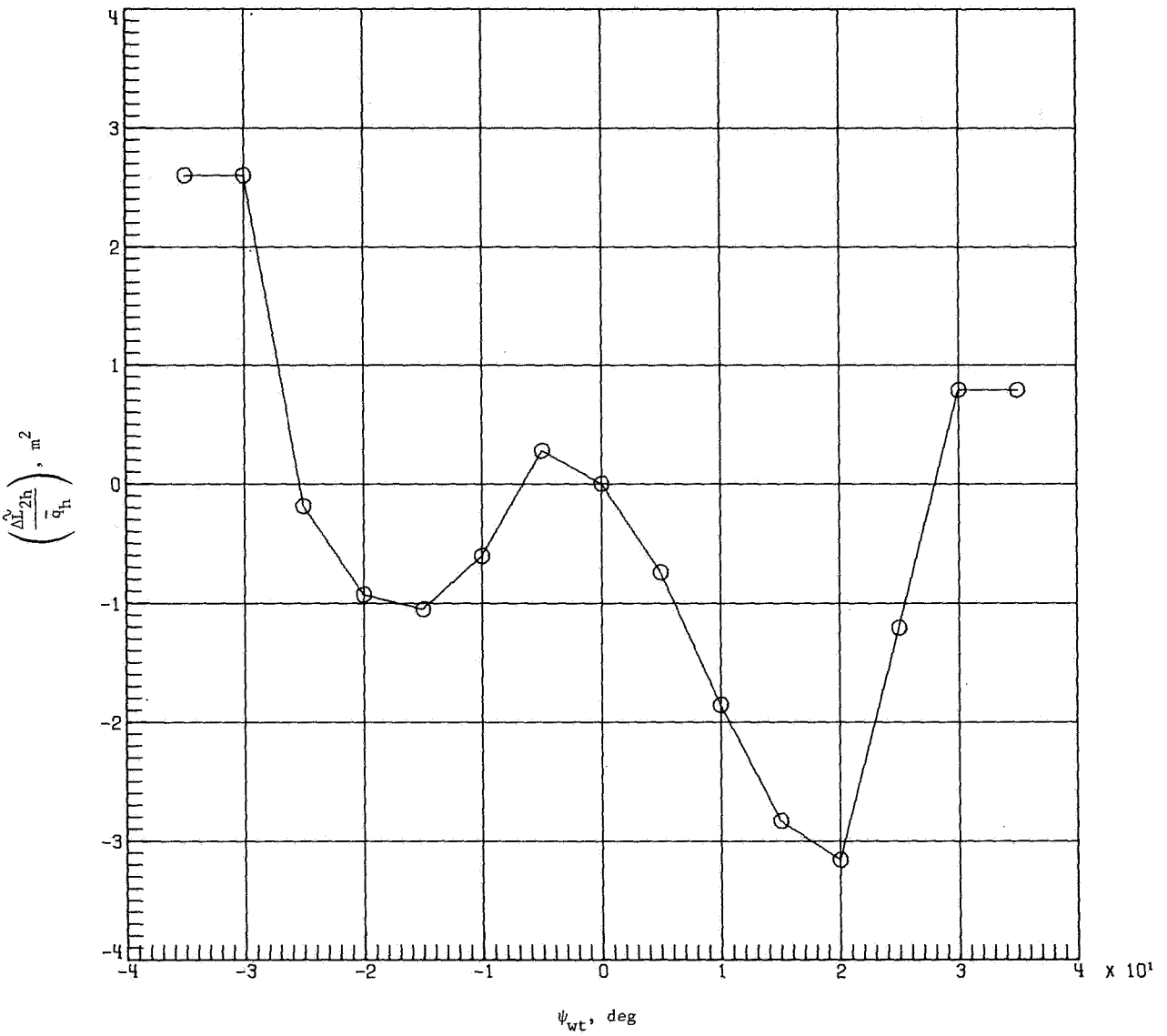

Figure 6.- Fuselage incremental lift as a function of sideslip angle.

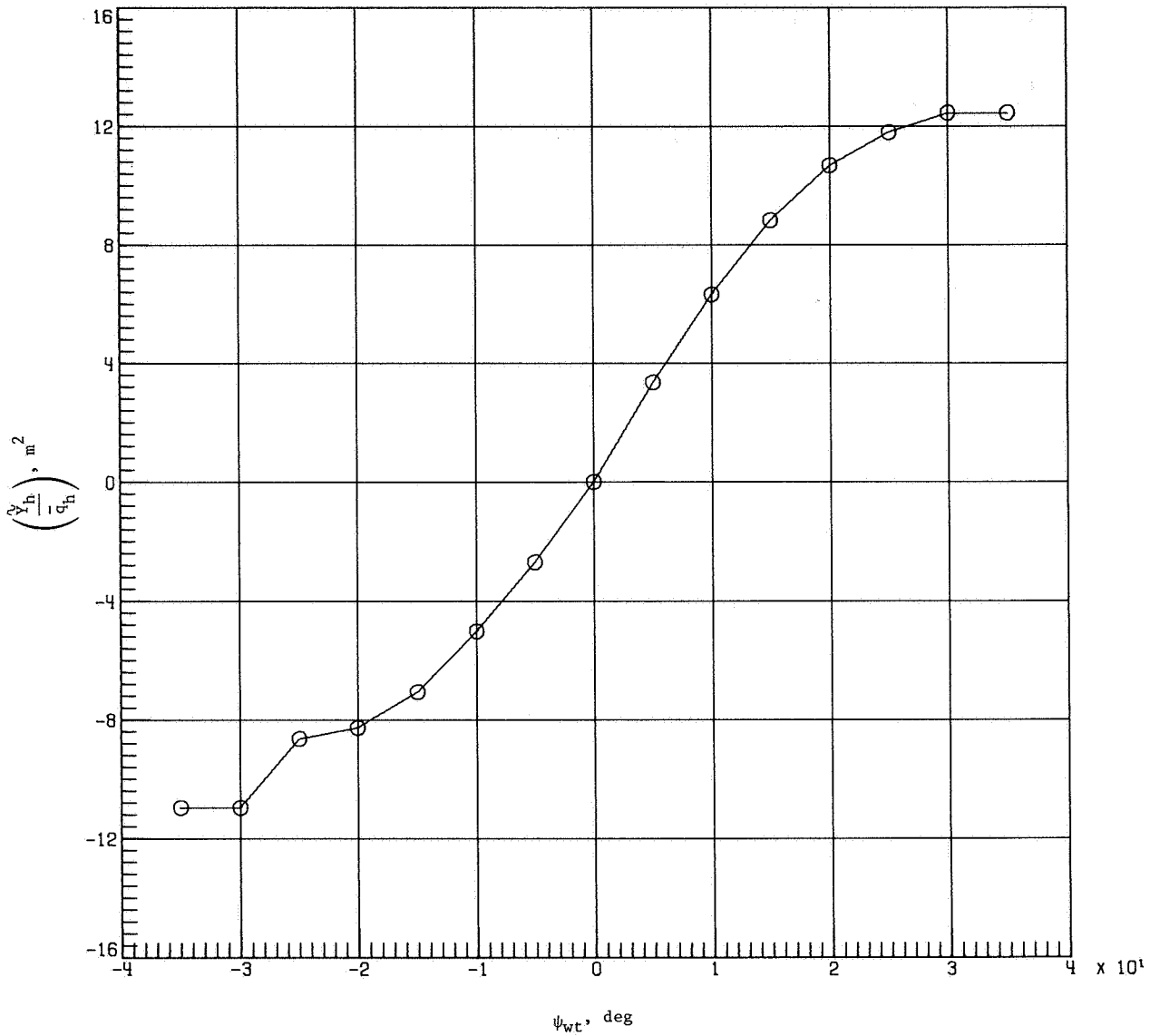

Figure 7.- Fuselage side force as a function of sideslip angle.

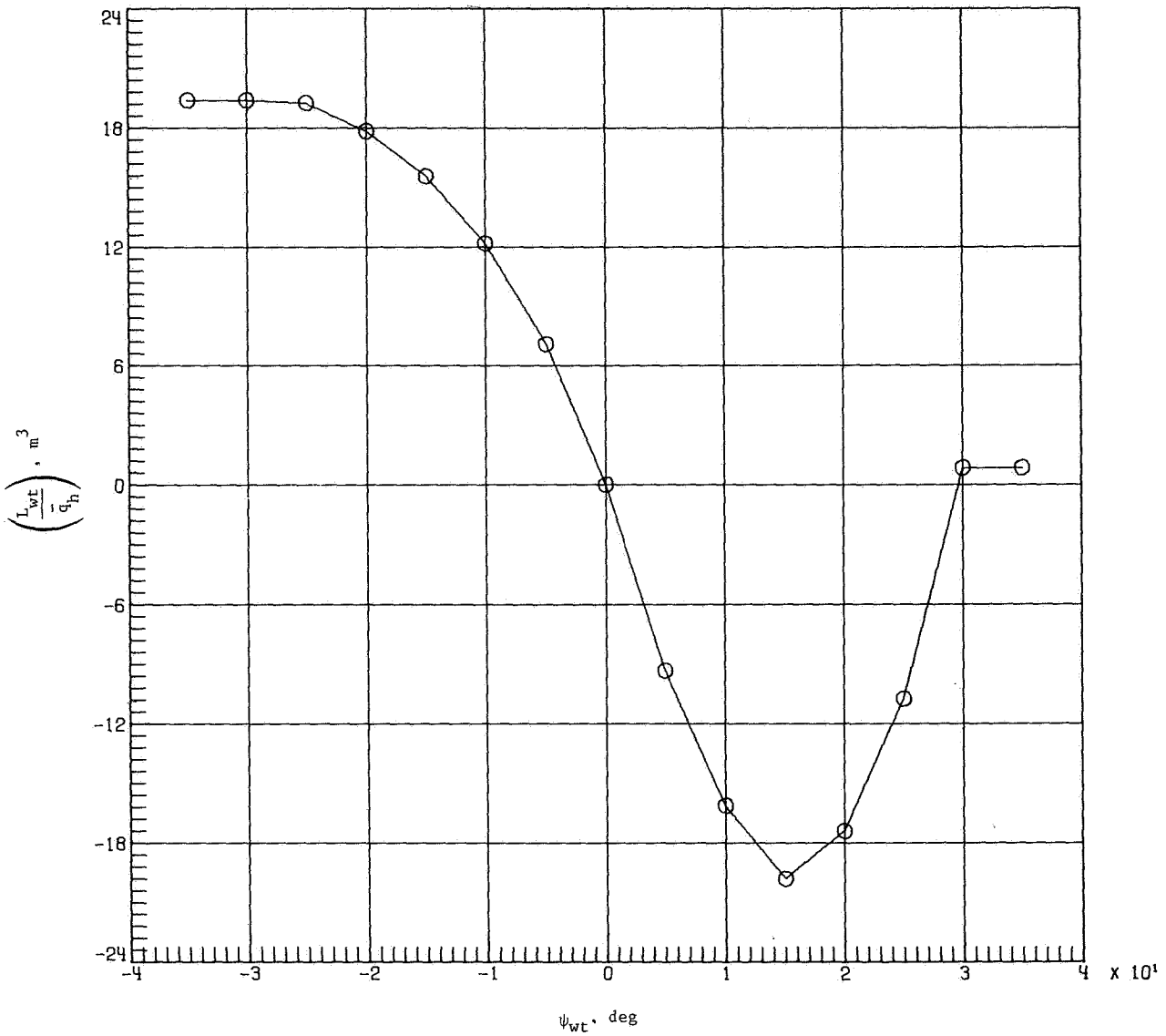

Figure 8.- Fuselage rolling moment as a function of sideslip angle.

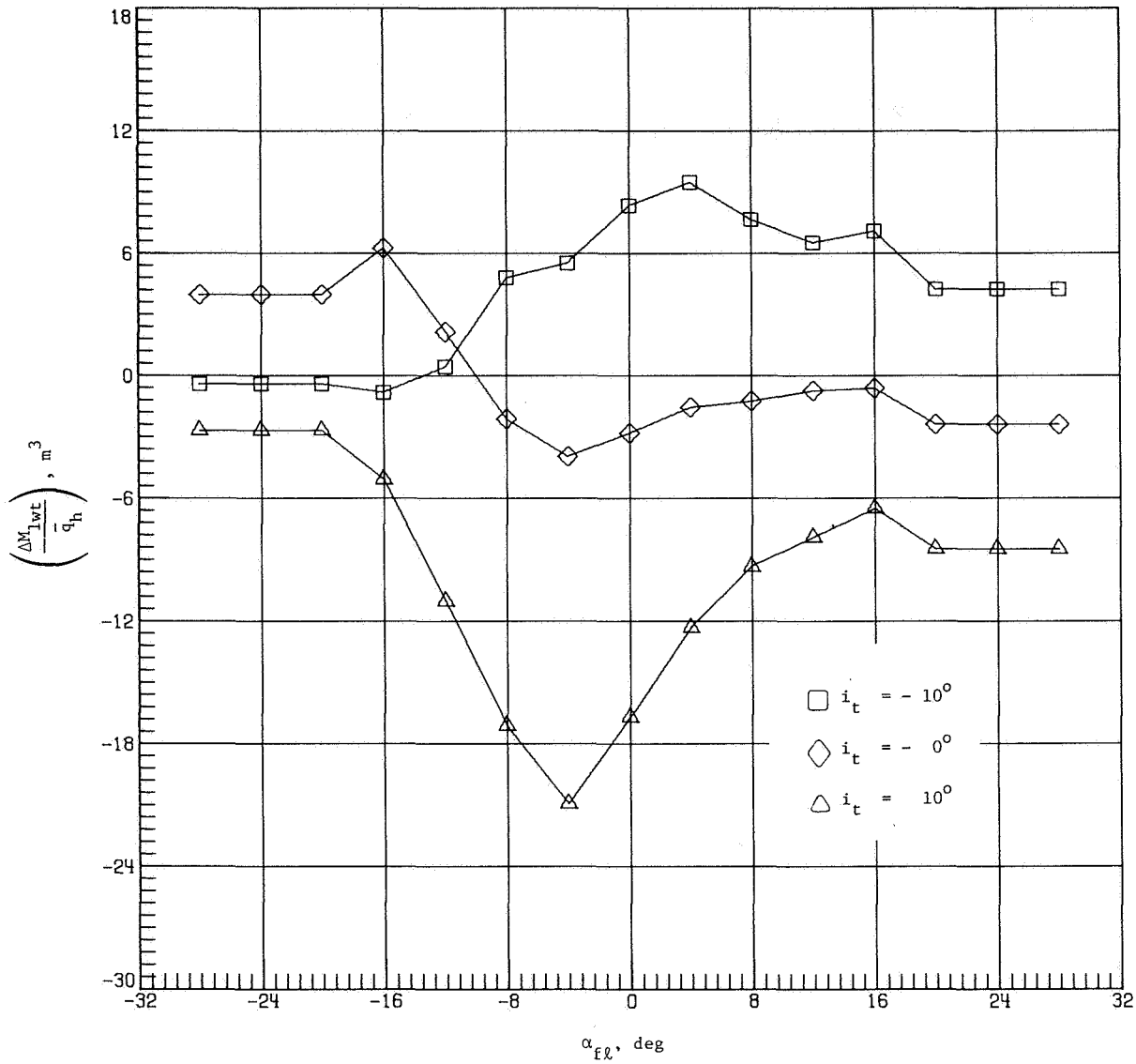

Figure 9.- Fuselage incremental pitching moment as a function of angle of attack for different values of incidence at the tail.

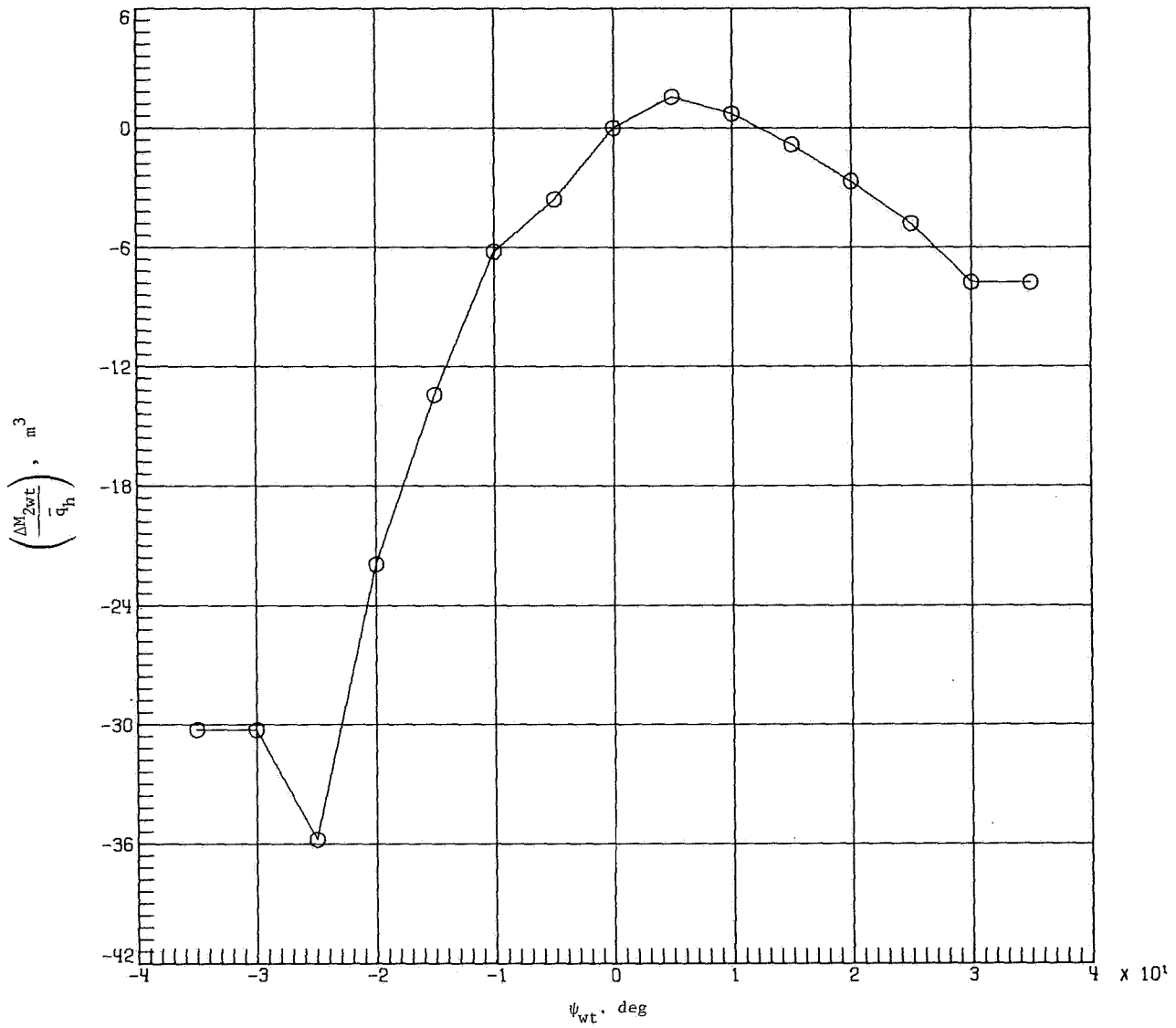

Figure 10.- Fuselage incremental pitching moment as a function of sideslip angle.

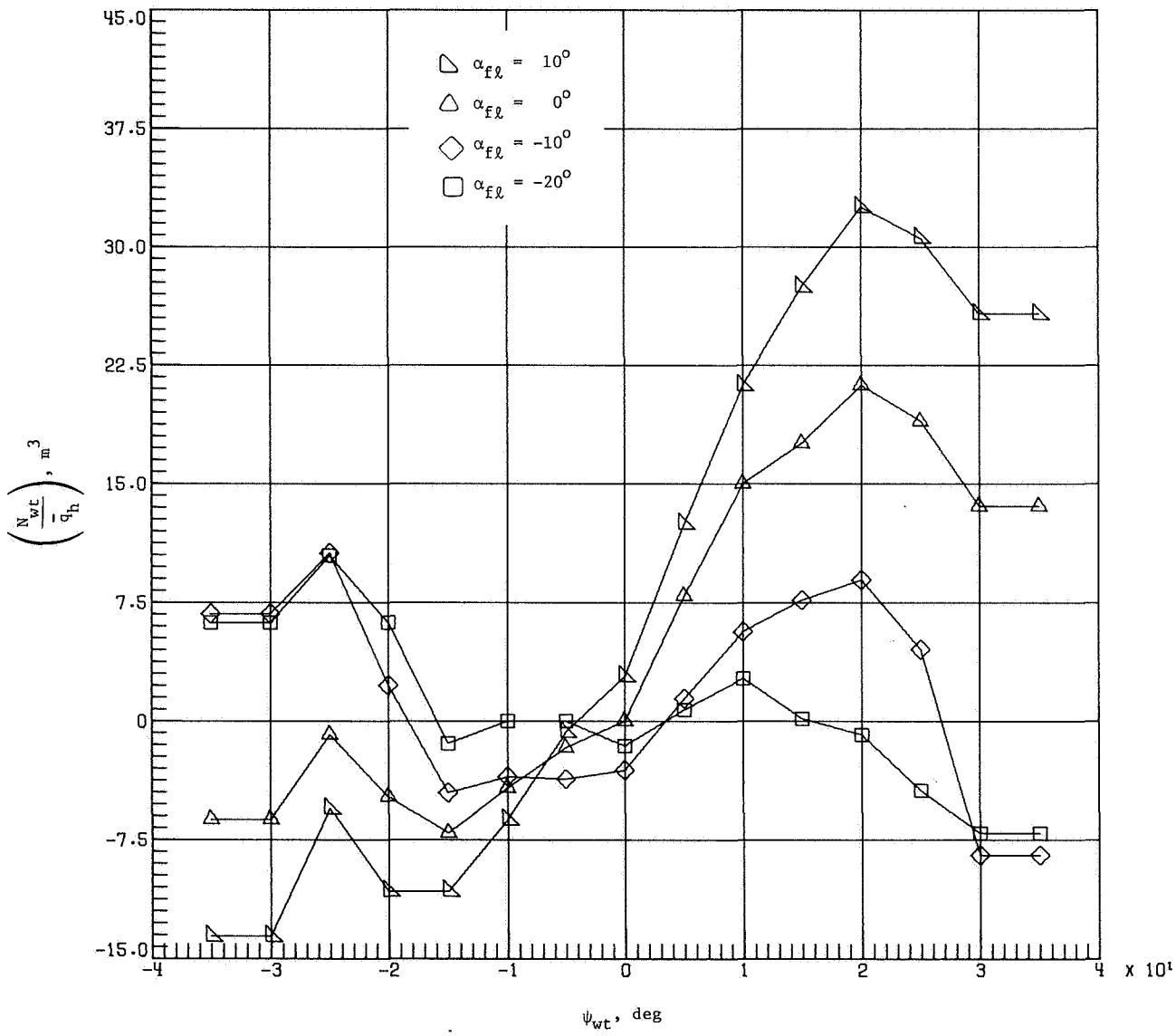

Figure 11.- Fuselage yawing moment as a function of sideslip angle for different values of angle of attack.

L-77-7919

Figure 12.- Simulation control console.

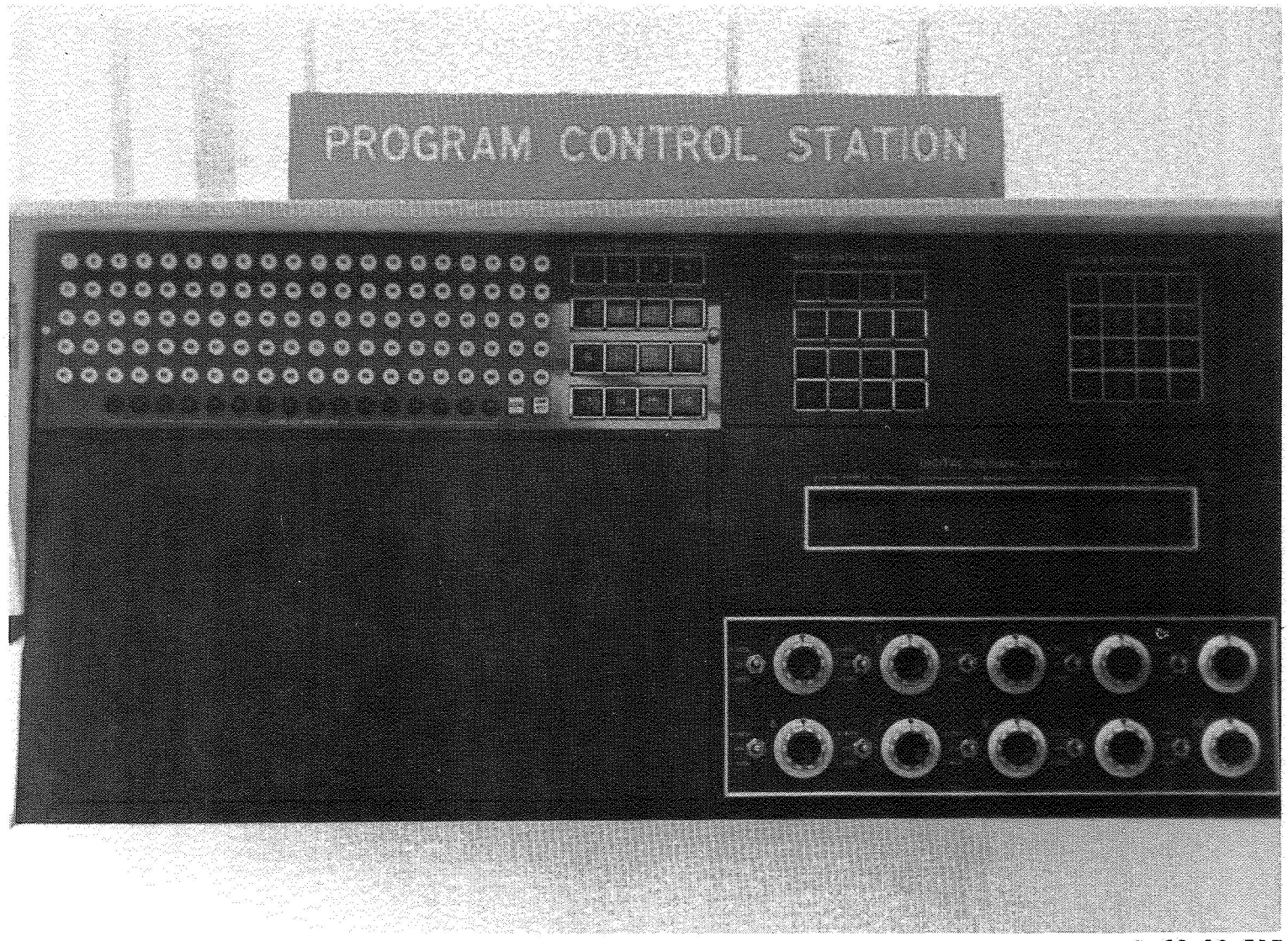

L-68-10 517

Figure 13.- Simulation control console close-up.

OPER	HOLD	RESET	IDLE
CHANGE	SCAN	RELEASE	
		ERASE	
TERM	READ	PRINT	RELEASE

(a) Mode control switches.

0	1	2	3
4	5	6	7
8	9	DECIMAL . POINT	(-)
TAB	(CR)	ERASE	CR

(b) Data entry keyboard.

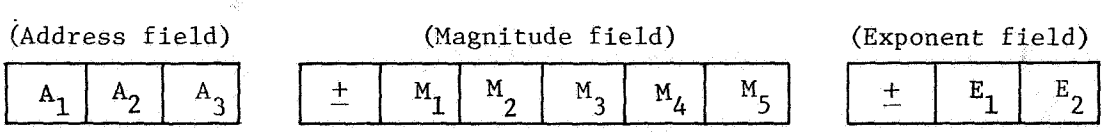

(c) Digital decimal display.

Figure 14.- Mode control, data entry, and digital display systems on simulation control console.

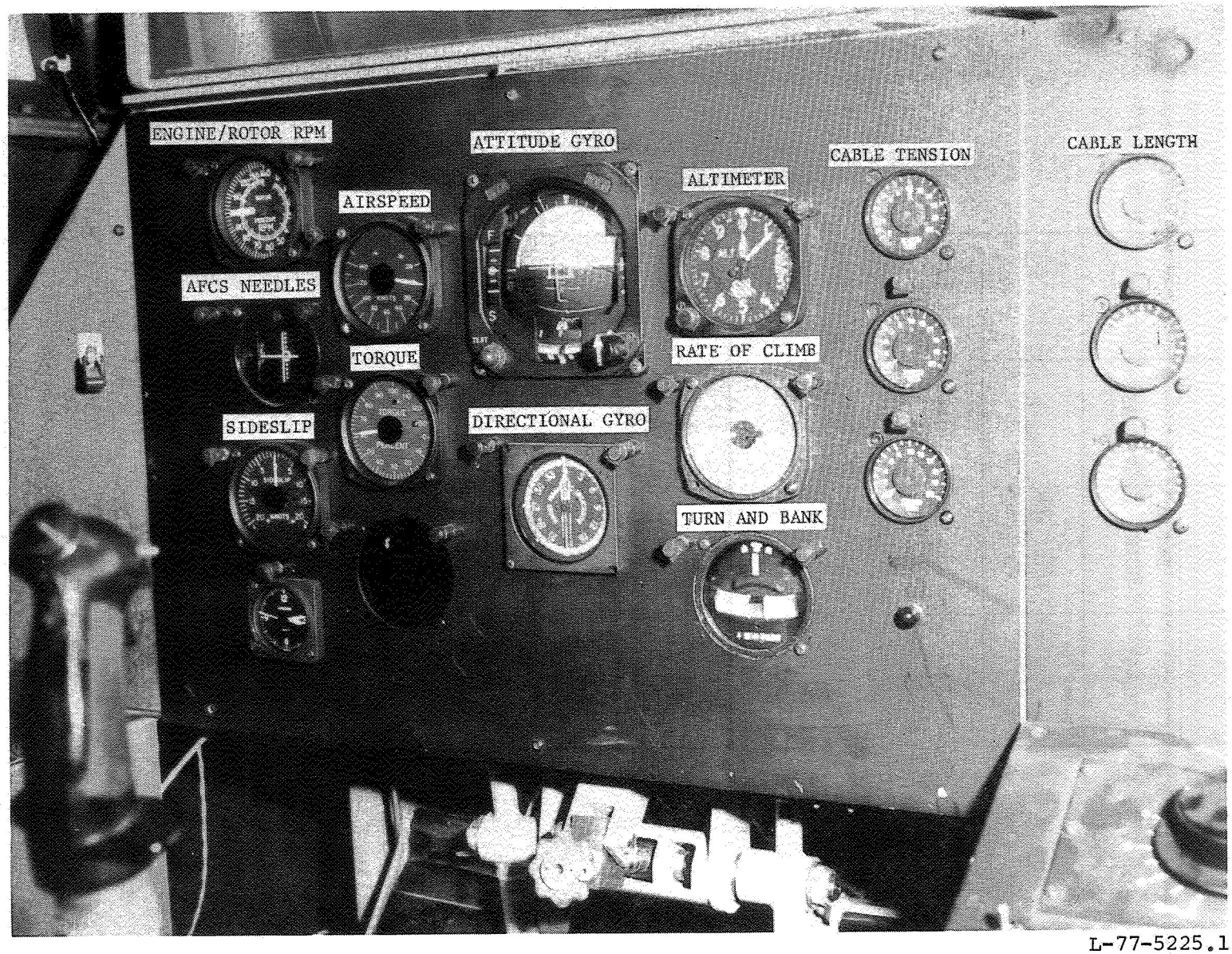

L-77-5225.1

Figure 15.- Simulator instrument panel.

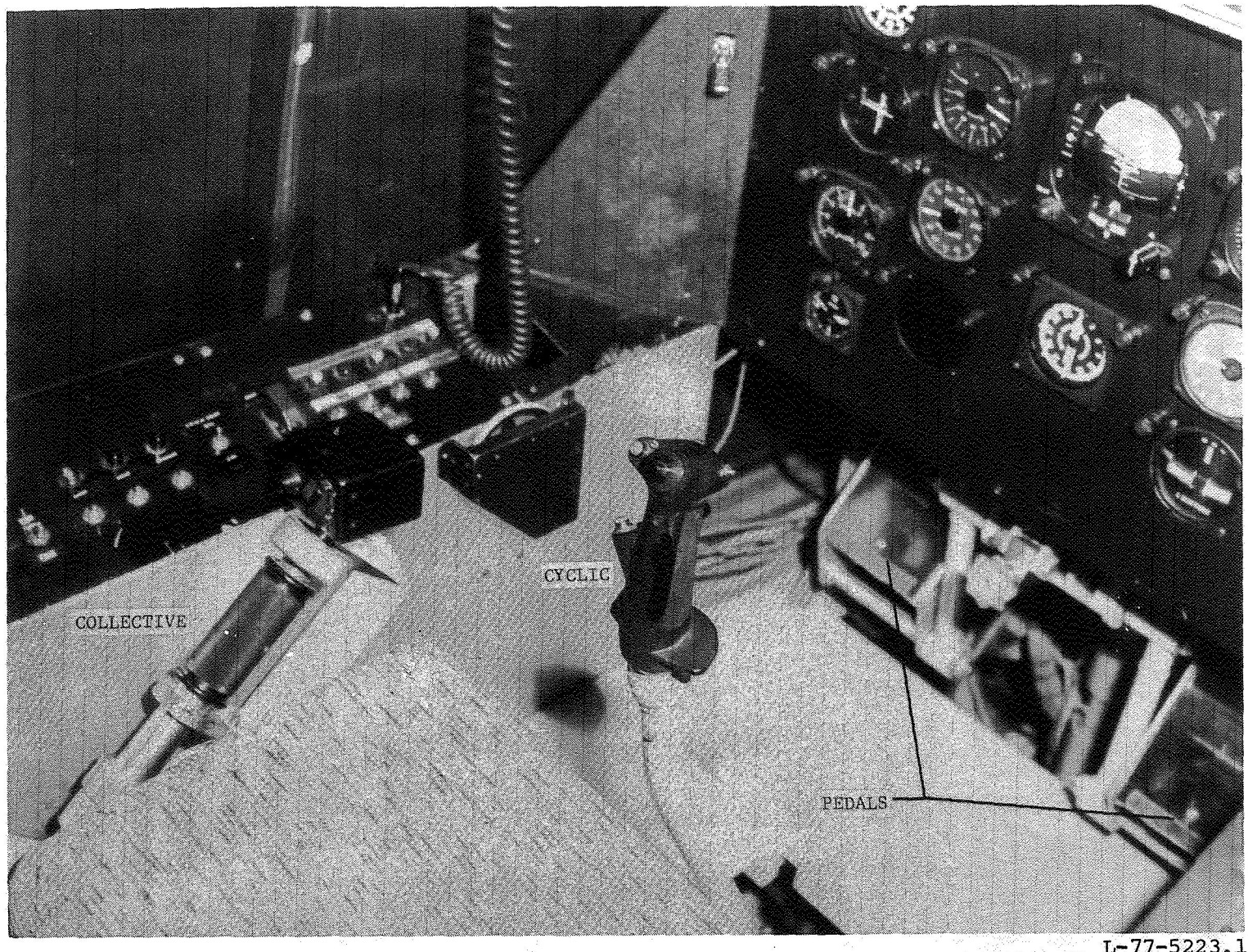

L-77-5223.1

Figure 16.- View of simulator cockpit showing cyclic, collective, and pedal controls.

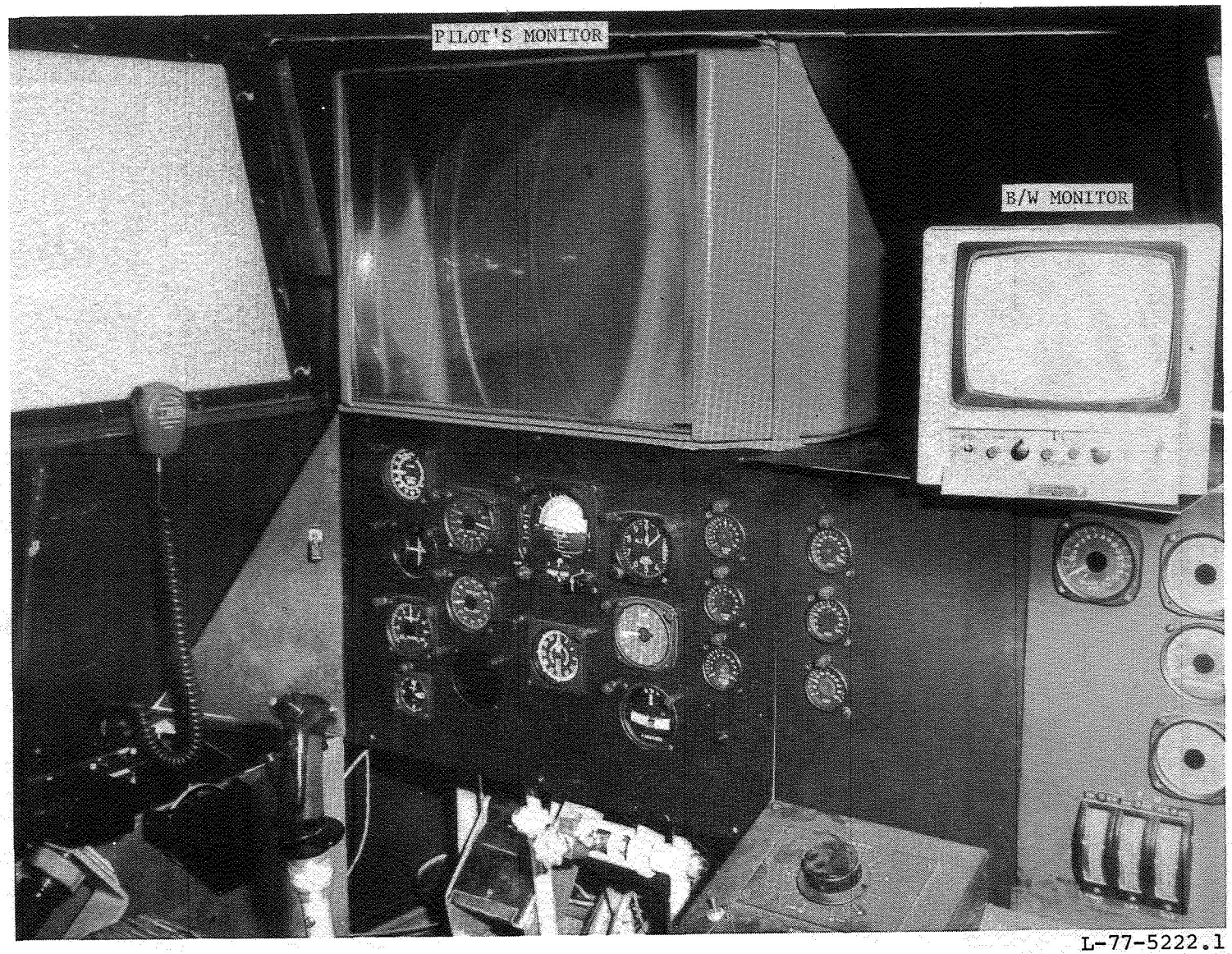

L-77-5222.1

Figure 17.- Simulator cockpit showing pilot's visual display monitor lens systems and researcher's black and white monitor.

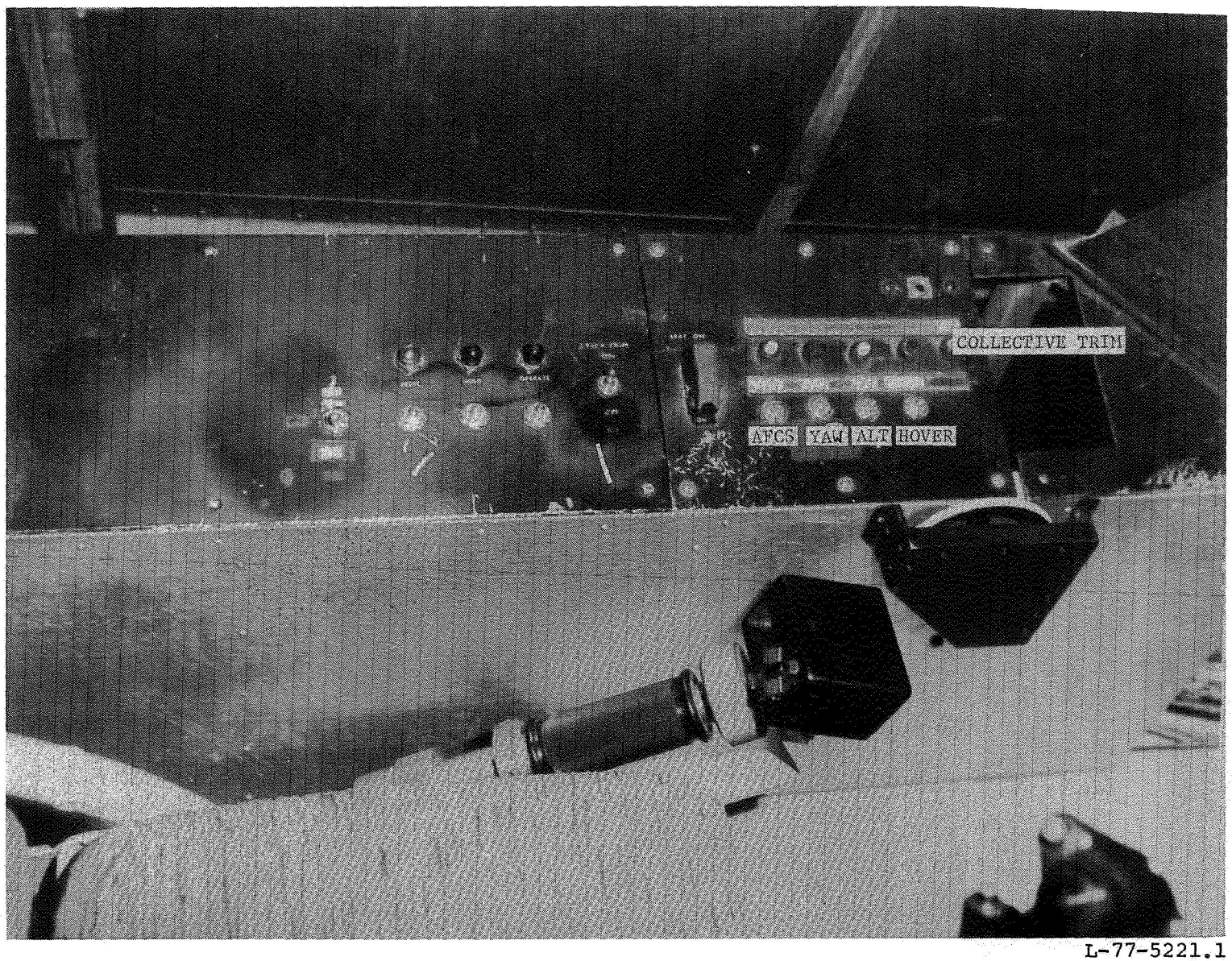

L-77-5221.1

Figure 18.- Simulator RESET, HOLD, and OPERATE push buttons as well as AFCS, YAW, altitude (ALT), and HOVER push buttons and indicators.

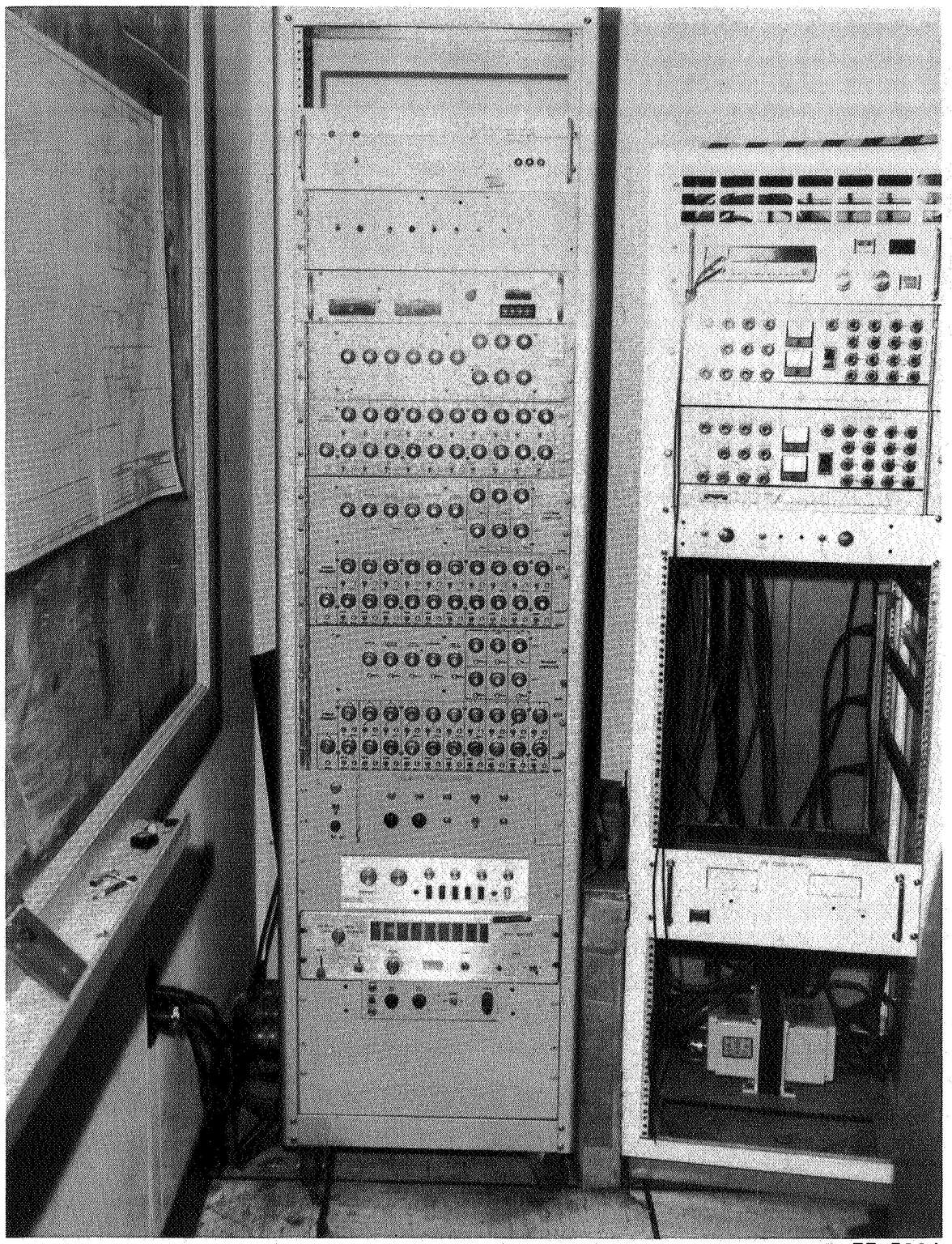

L-77-5224

Figure 19.- Simulator control system analog computer (on the left).

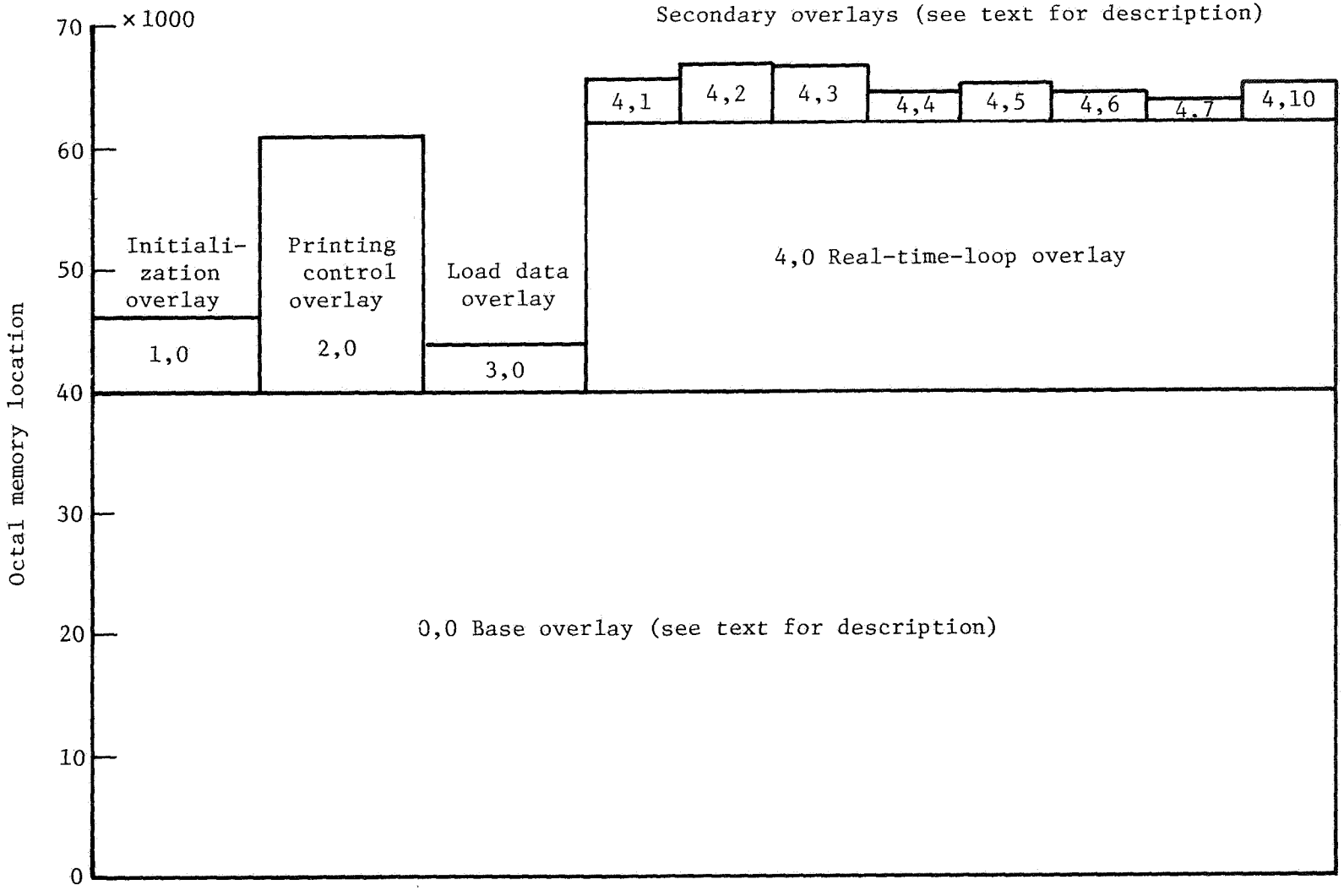

Figure 20.- Simulation central memory layout.

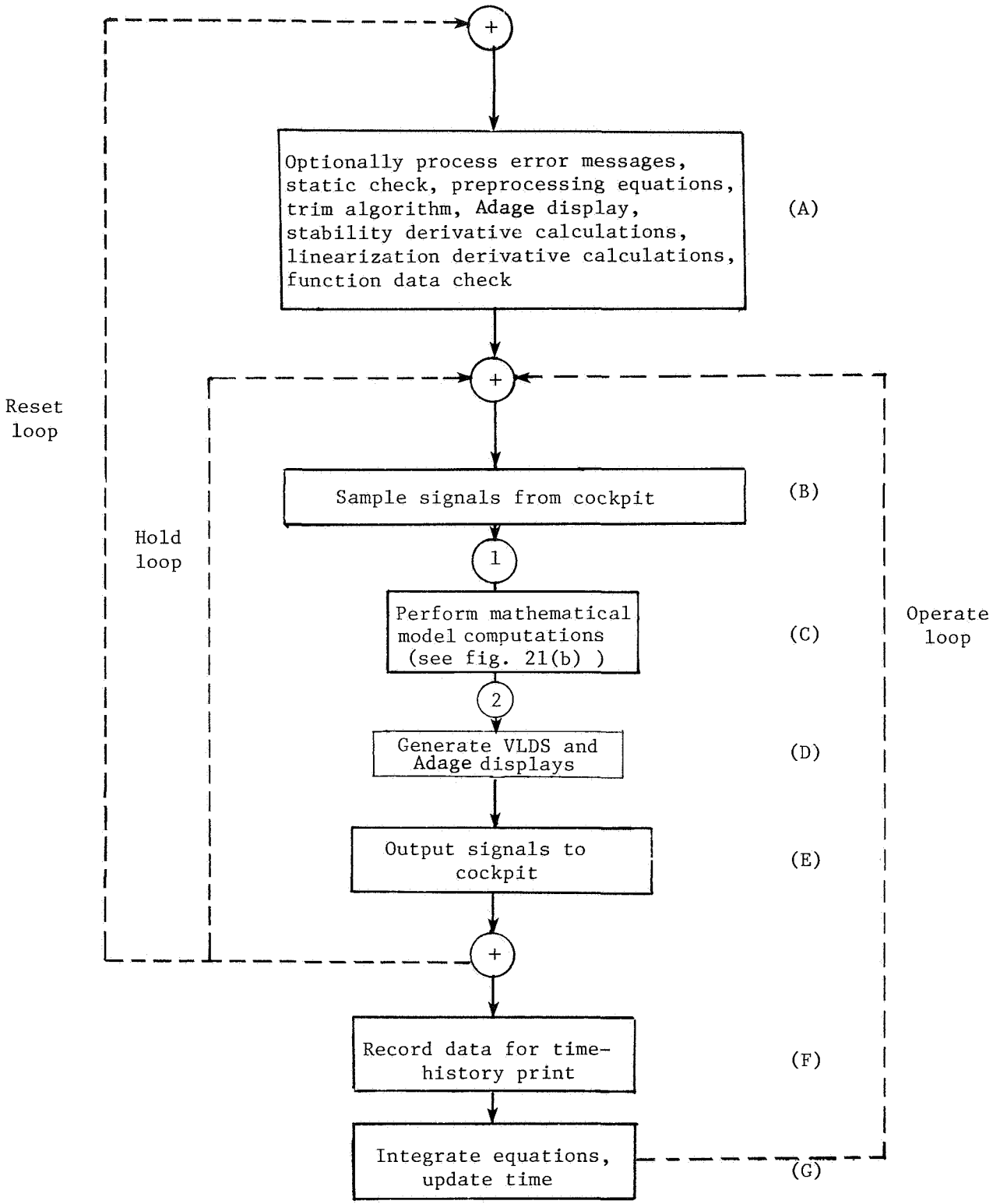

(a) General flow diagram.

Figure 21.- Simulation flow diagram.

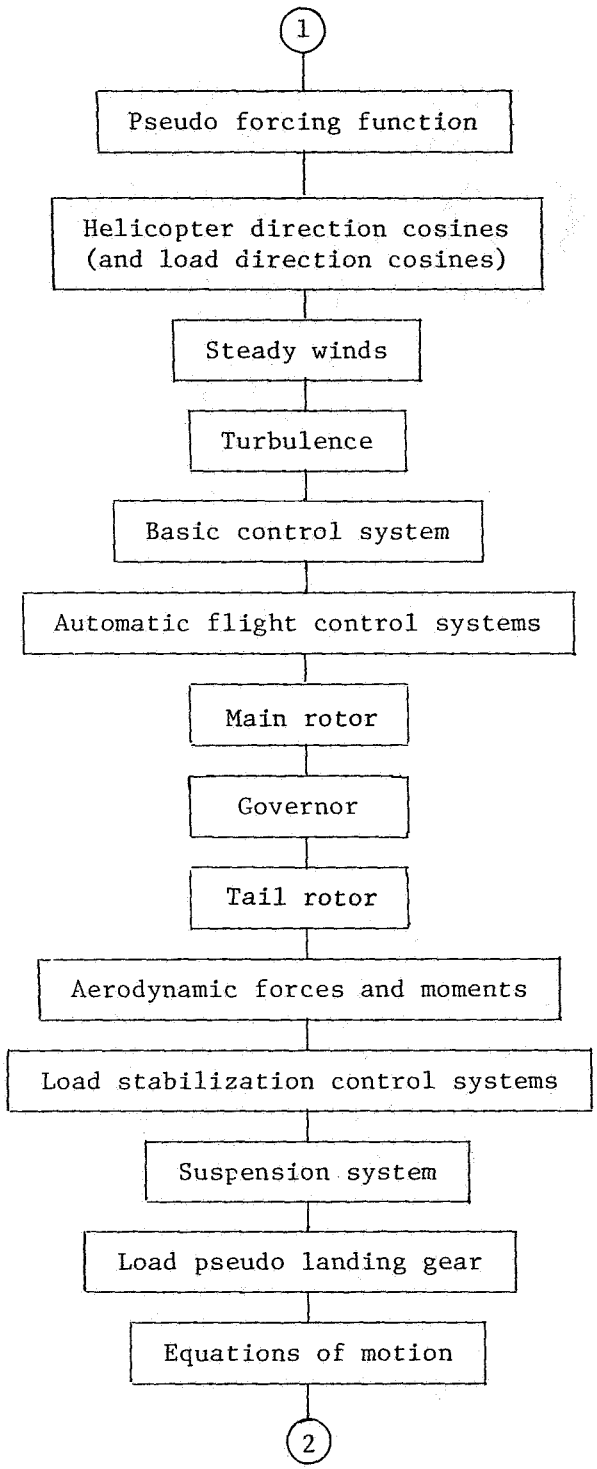

(b) Mathematical model flow diagram.

Figure 21.- Concluded.

L-75-7494

Figure 22.- VLDS model board mounted vertically and camera drive system.

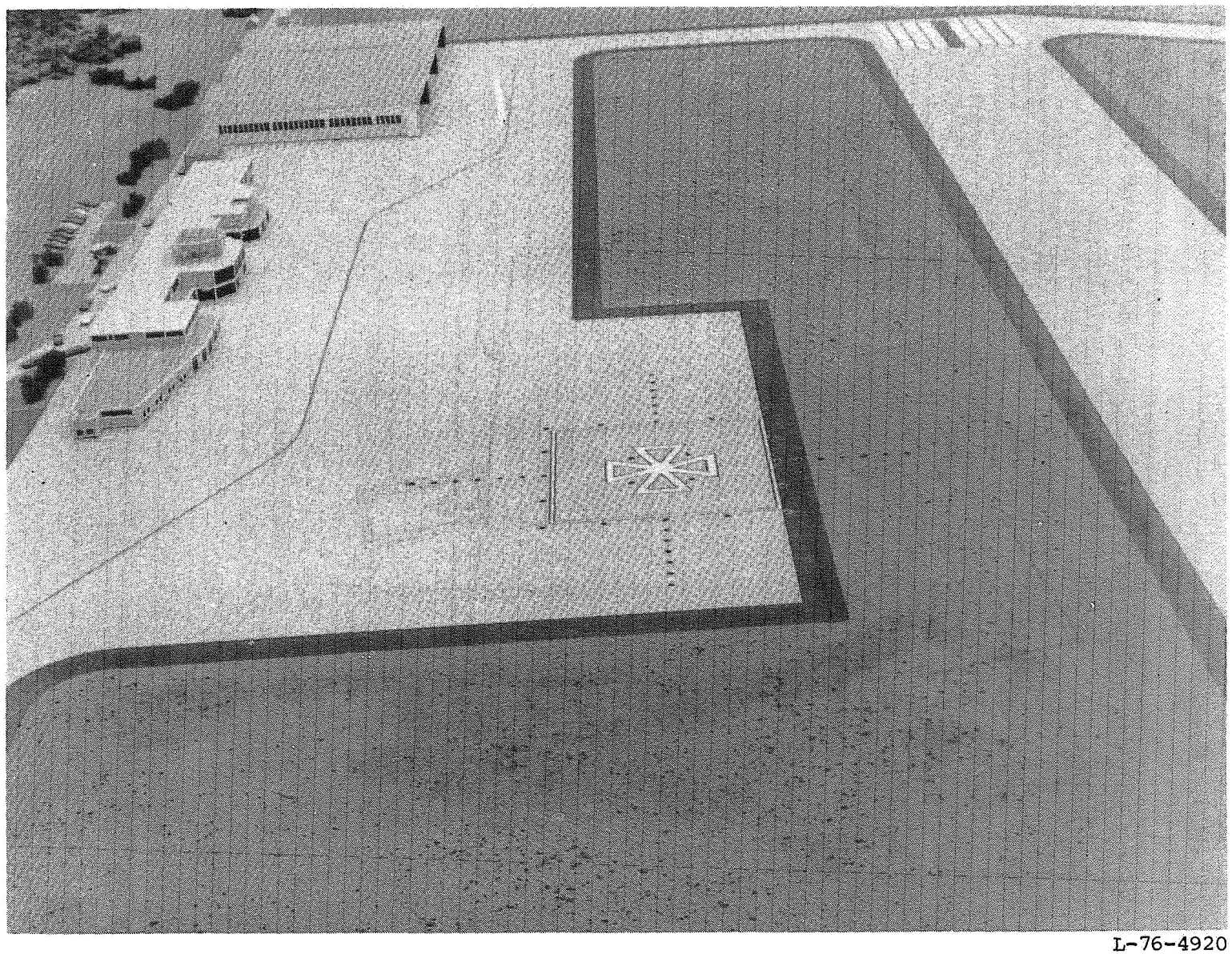

L-76-4920

Figure 23.- VLDS heliport landing zone close-up.

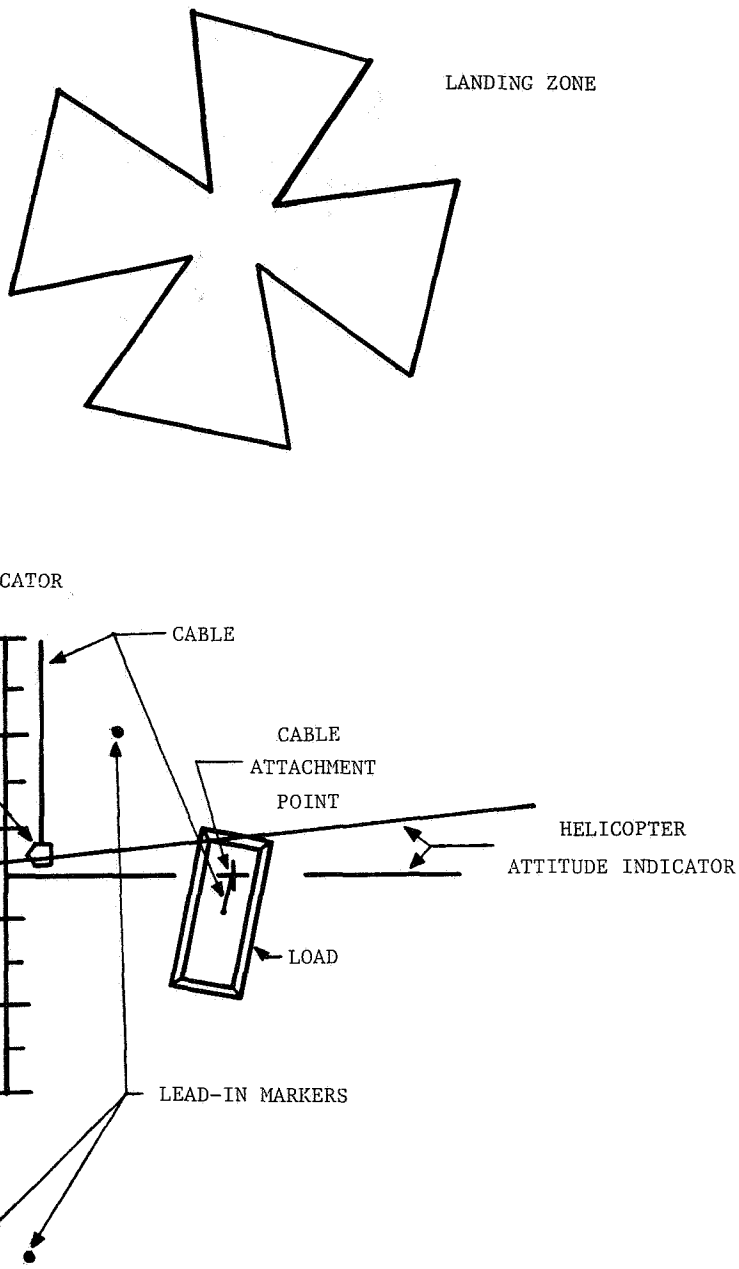

Figure 24.- Sketch of computer-generated load/landing zone display.

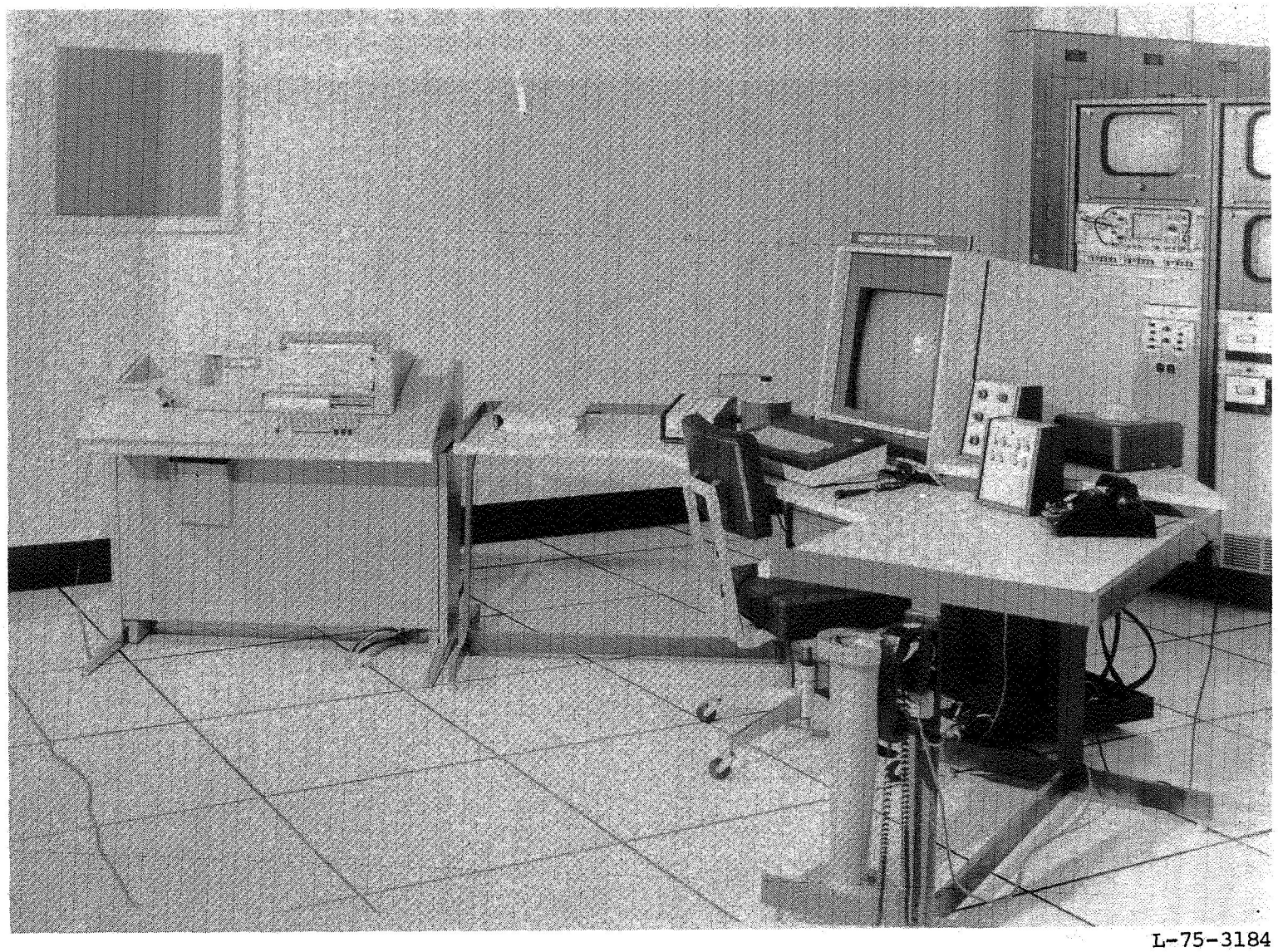

L-75-3184

Figure 25.- Adage Graphics Terminal console.

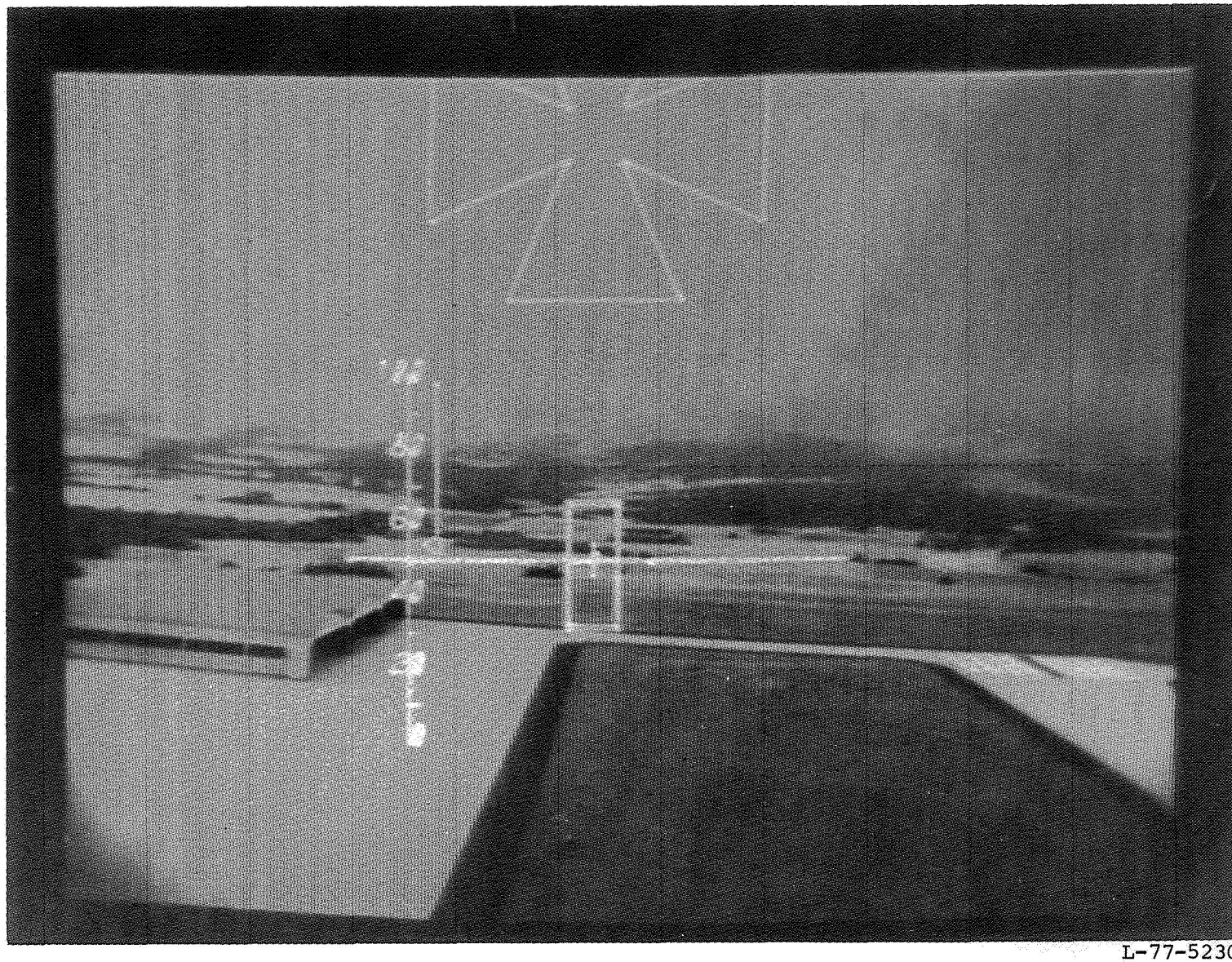

L-77-5230

Figure 26.- Photograph of pilot's out-the-window display at an altitude of 55 m and a distance of 30 m from landing zone.

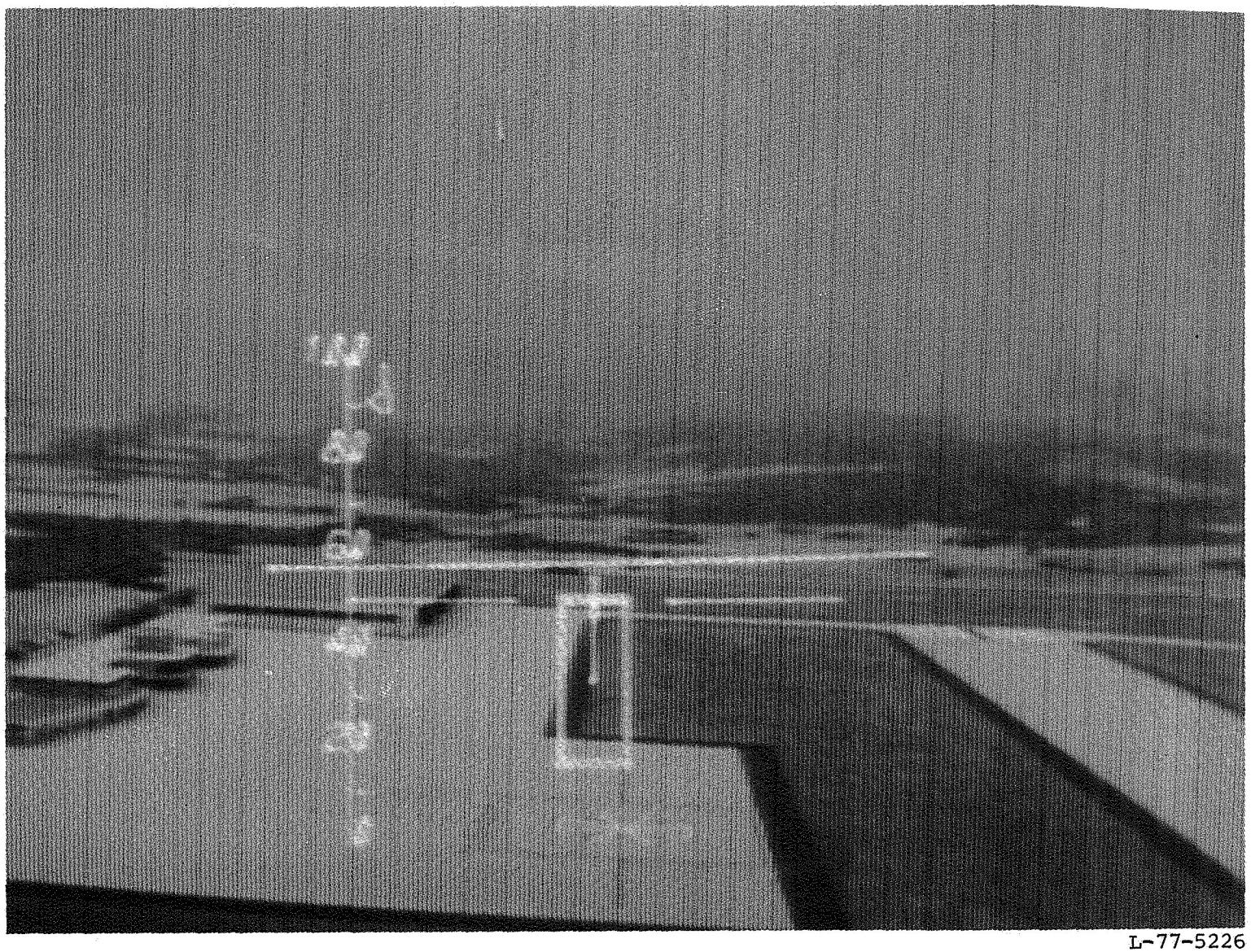

L-77-5226

Figure 27.- Photograph of pilot's out-the-window display at an altitude of 66 m and a distance of 305 m from landing zone.

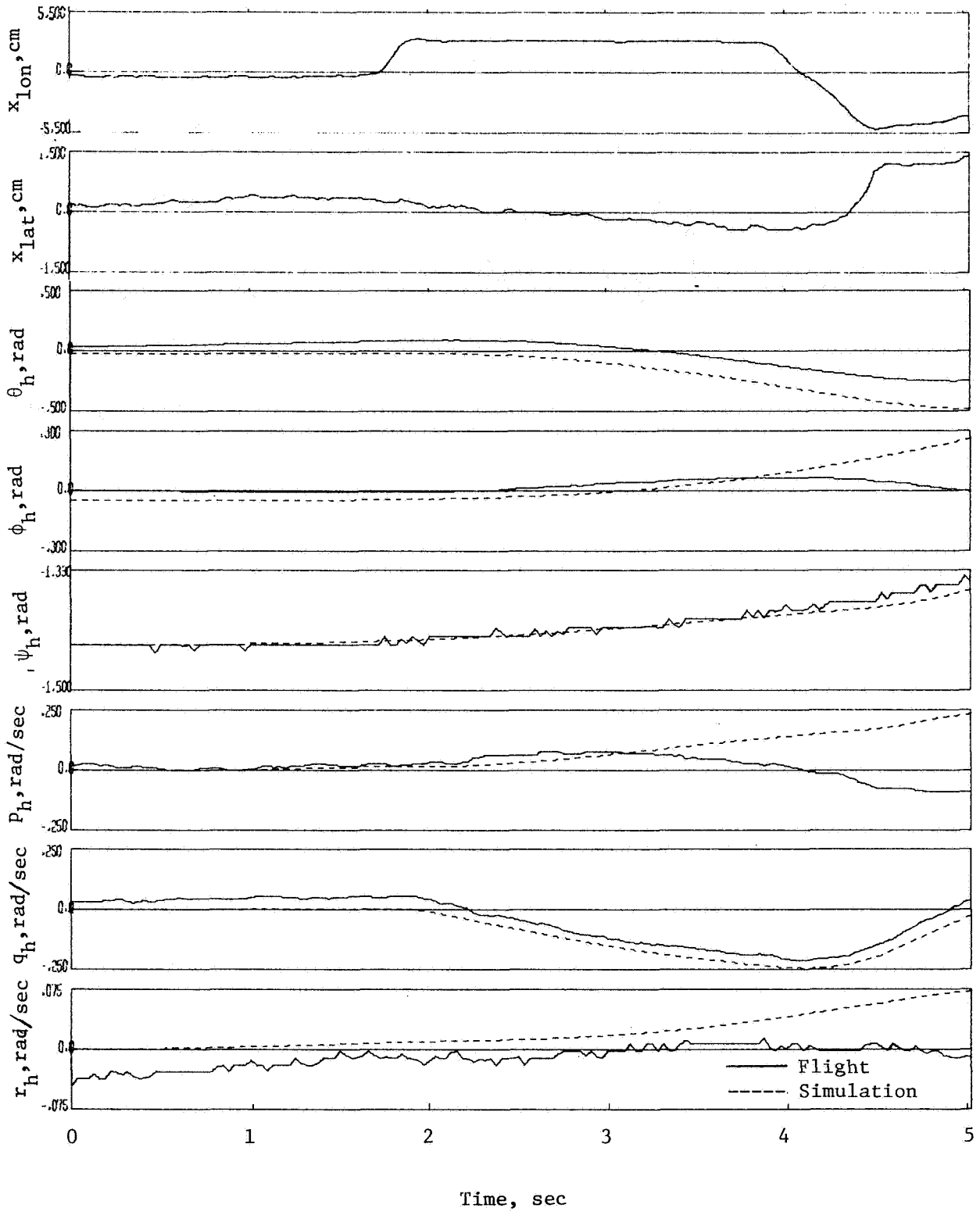

Figure 28.- Comparison of flight data with simulation data at hover for identical control inputs.

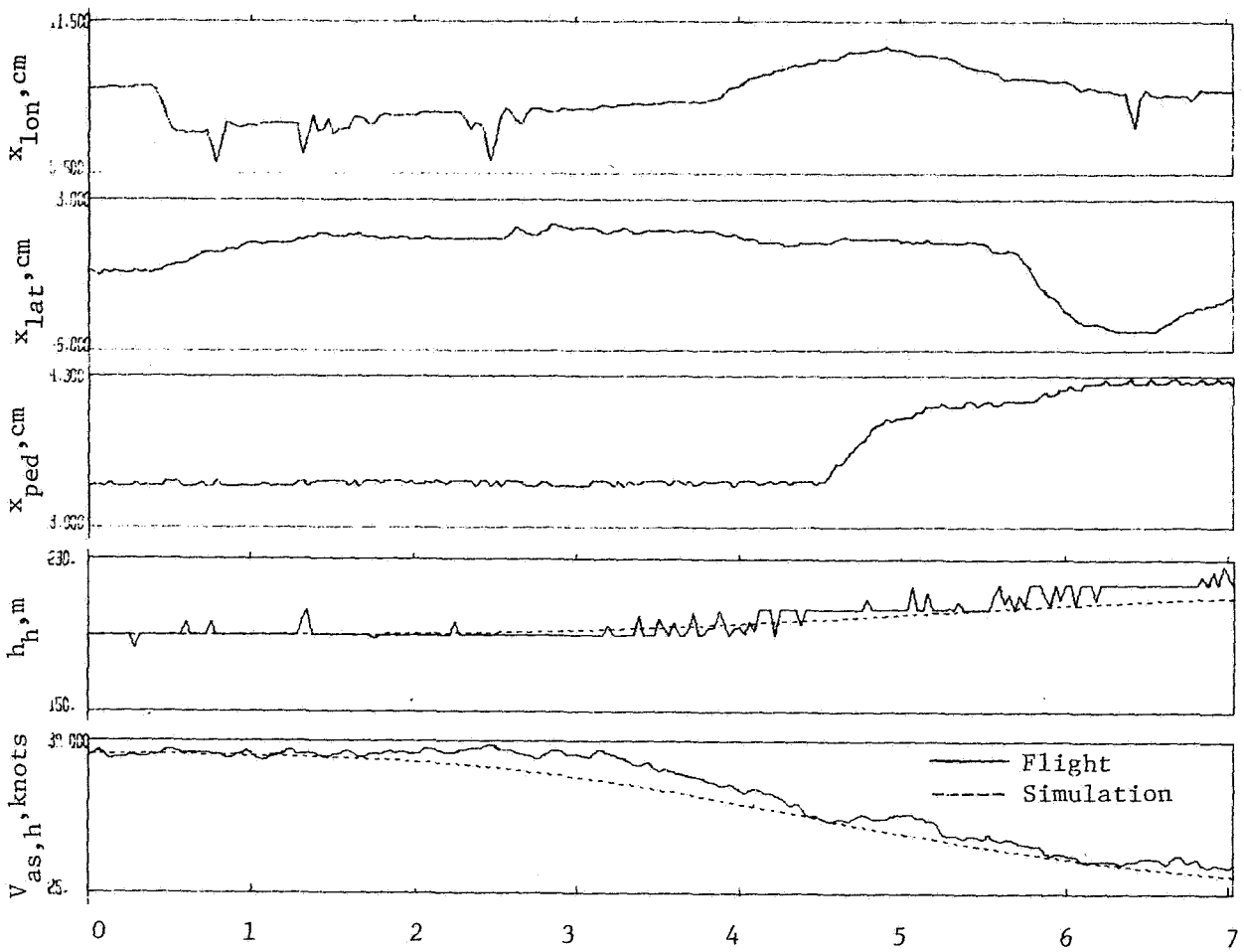

Figure 29.- Comparison of flight data with simulation data at 38 knots for identical control inputs.

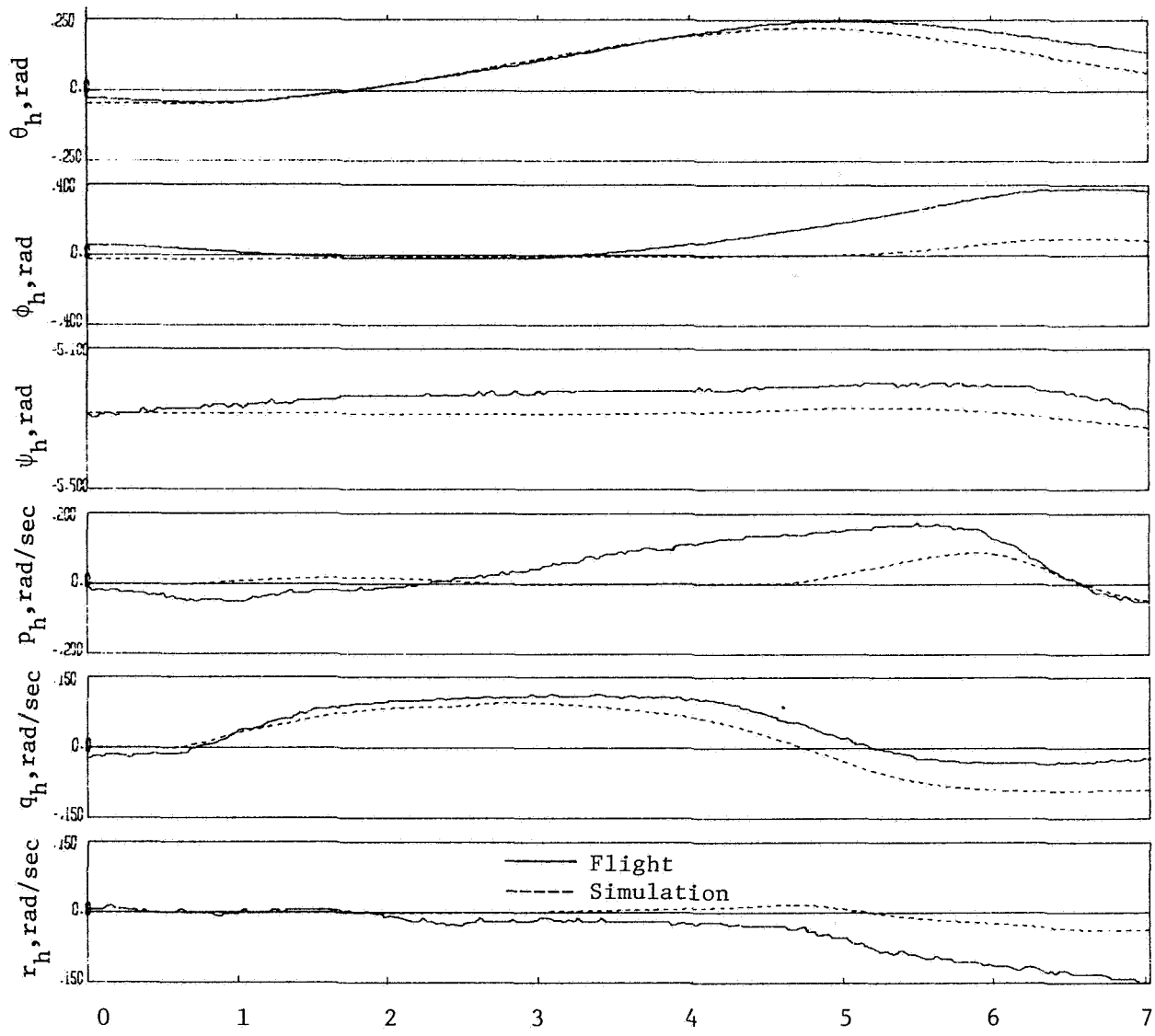

Figure 29.- Concluded.

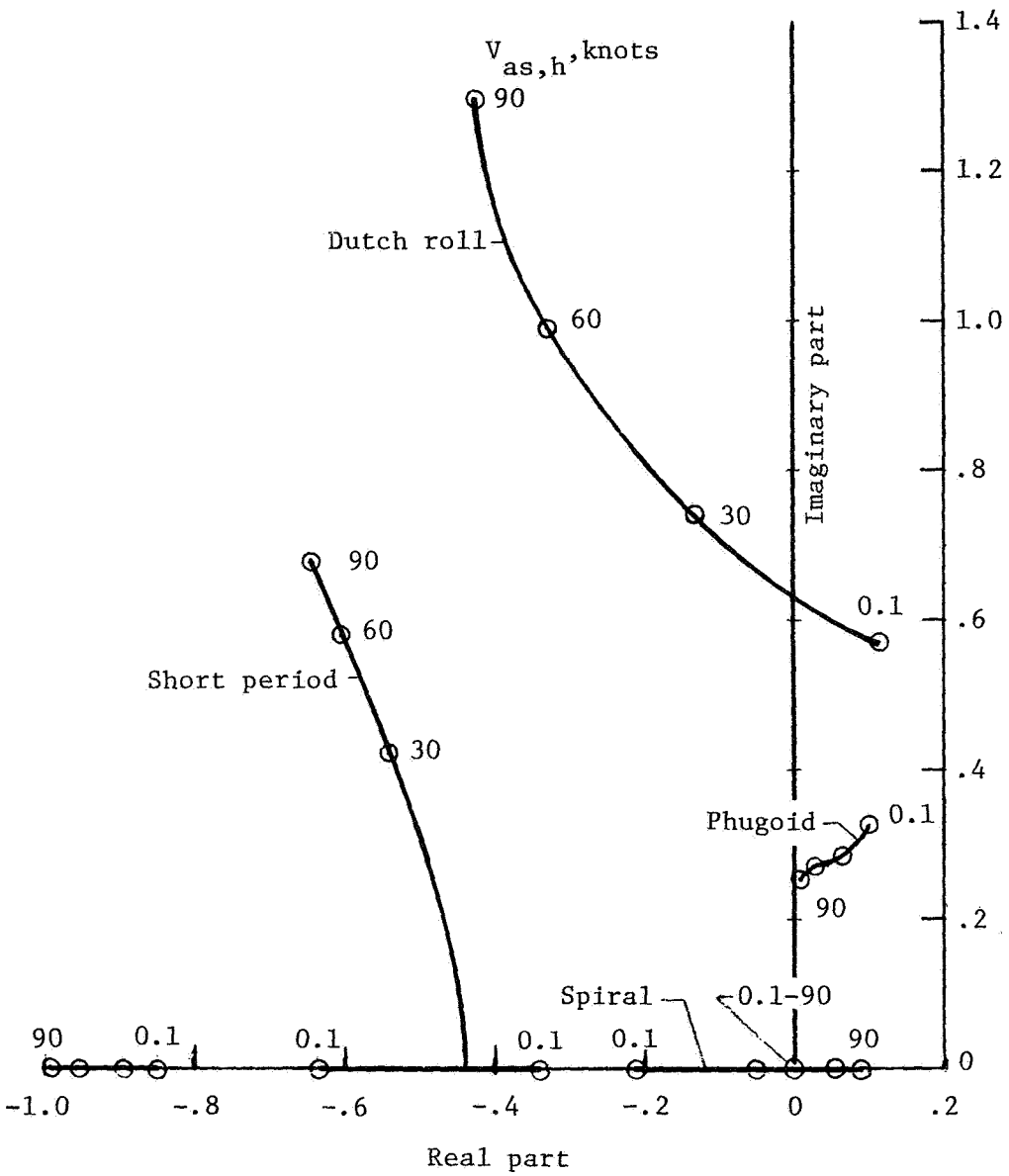

Figure 30.- Eigenvalues at four airspeeds obtained from linearized mathematical model.

1. Report No.	2. Government Accession No.	3. Recipient's Catalog No.
NASA TP-1285		

4. Title and Subtitle	5. Report Date
DEVELOPMENT AND VALIDATION OF A PILOTED SIMULATION OF A HELICOPTER AND EXTERNAL SLING LOAD	January 1979
	6. Performing Organization Code

7. Author(s)	8. Performing Organization Report No.
J. D. Shaughnessy, Thomas N. Deaux, and Kenneth R. Yenni	L-11925
	10. Work Unit No. 505-08-26-01
9. Performing Organization Name and Address	11. Contract or Grant No.
NASA Langley Research Center Hampton, VA 23665	
	13. Type of Report and Period Covered Technical Paper
12. Sponsoring Agency Name and Address	14. Sponsoring Agency Code
National Aeronautics and Space Administration Washington, DC 20546	

15. Supplementary Notes

J. D. Shaughnessy and Kenneth R. Yenni: Langley Research Center.
Thomas N. Deaux: Sperry Support Services, Hampton, Virginia.

16. Abstract

A generalized, real-time, piloted, visual simulation of a single-rotor helicopter, suspension system, and external load is described and validated for the full flight envelope of the U.S. Army CH-54 helicopter and cargo container as an example. The mathematical model described uses modified nonlinear classical rotor theory for both the main rotor and tail rotor, nonlinear fuselage aerodynamics, an elastic suspension system, nonlinear load aerodynamics, and a load-ground contact model. The implementation of the mathematical model on a large digital computing system is described, and validation of the simulation is discussed. The mathematical model is validated by comparing measured flight data with simulated data, by comparing linearized system matrices, eigenvalues, and eigenvectors with manufacturers' data, and by the subjective comparison of handling characteristics by experienced pilots. A visual landing display system for use in simulation which generates the pilot's forward-looking real-world display is discussed, and a special head-up, down-looking load/landing zone display is described.

17. Key Words (Suggested by Author(s))	18. Distribution Statement
Helicopter External/sling load Rotorcraft Visual simulation	Unclassified - Unlimited Subject Category 05

19. Security Classif. (of this report)	20. Security Classif. (of this page)	21. No. of Pages	22. Price*
Unclassified	Unclassified	111	$6.50

* For sale by the National Technical Information Service, Springfield, Virginia 22161

NASA-Langley, 1979

National Aeronautics and
Space Administration

Washington, D.C.
20546

Official Business
Penalty for Private Use, $300

THIRD-CLASS BULK RATE

Postage and Fees Paid
National Aeronautics and
Space Administration
NASA-451

NASA

POSTMASTER: If Undeliverable (Section 158
Postal Manual) Do Not Return